

THESIS FOR THE DEGREE OF DOCTOR OF PHILOSOPHY

**Mechanisms of Enhanced Activity of Model
TiO₂/Carbon and TiO₂/Metal Nanocomposite
Photocatalysts**

Raja Sellappan



Department of Applied Physics
Chalmers University of Technology
Göteborg, Sweden 2013

Mechanisms of Enhanced Activity of Model TiO₂/Carbon and TiO₂/Metal
Nanocomposite Photocatalysts

Raja Sellappan

Göteborg, 2013

ISBN 978-91-7385-871-7

© Raja Sellappan, 2013

Doktorsavhandlingar vid Chalmers Tekniska Högskola

Ny serie nr. 3552

ISSN 0346-718X

Department of Applied Physics

Chalmers University of Technology

SE-412 96 Göteborg

Sweden

Telephone: +46 (0)31 772 1000

Cover picture: Schematics of TiO₂/Carbon and TiO₂/Metal nanocomposite photocatalysts used in the thesis (left). Simplified energy level diagrams (right) of the corresponding schematics under the bandgap excitation (top) and the plasmonic excitation (bottom). The lightning bolt symbol represents near- and far-field plasmonic effects.

Printed by:

Chalmers Reproservice

Göteborg, Sweden 2013

Mechanisms of Enhanced Activity of Model TiO₂/Carbon and TiO₂/Metal Nanocomposite Photocatalysts

Raja Sellappan

Department of Applied Physics

Chalmers University of Technology, Göteborg 2013

Abstract

TiO₂ is the most widely used photocatalyst for energy and environmental applications because of its outstanding physical and chemical properties. However, the quantum efficiency of TiO₂ is greatly diminished by fast electron-hole pairs recombination and light absorption only in the UV region. This thesis deals with two approaches aiming to improve TiO₂ performance through design of model systems. Emphasis is given to understand the underlying photocatalytic mechanisms.

In the first approach, a model consisting of TiO₂/Graphitic carbon nanocomposites has been fabricated to address the role of carbon on charge carrier dynamics and light absorption. Composites showed a significant enhanced photocatalytic activity compared to bare TiO₂ films in the UV region for the test reaction of gas phase methanol photooxidation. The enhanced activity was attributed to improved charge carrier separation at the interface between carbon and TiO₂ films. Photoluminescence (PL) studies confirmed further the improved charge carrier separation in composites, showing reduced PL intensity and shorter lifetime. Another type of model TiO₂/Graphene composite photocatalysts was prepared with the aim of demonstrating the role of graphene synthesizing techniques on the performance of TiO₂ photocatalytic activity. Graphene prepared by different methods resulted in different morphology and electrical conductivity. These modifications strongly affected charge carrier dynamics as revealed by PL studies and in turn affected the photocatalytic activity.

In the second approach, model systems consisting of TiO₂ and optically active Au and Ag metal nanoparticles (NPs) in different configurations were designed to address the role of localized surface plasmon resonance (LSPR)-related effects on the photocatalytic activity of undoped TiO₂ films. Sample irradiation conditions were chosen to excite TiO₂ and NPs separately as well as simultaneously. A substantial enhanced photoactivity was observed for TiO₂/Metal composites compared to bare TiO₂ films. The model systems were evaluated in two different photoreactor systems with two different photocatalytic reactions (methanol and ethylene photooxidation). The enhanced activity was attributed to (i) Interfacial charge transfer from TiO₂ to NPs, when they are in direct contact with each other and (ii) Plasmonic near-and far-field effects, when there is an overlap of the plasmonic band with the TiO₂ absorption band.

In addition, TiO₂/Cu nanocomposite samples were prepared and tested under UV irradiation with the aim of understanding Cu NPs' chemical stability at conditions resembling CO₂ photoreduction to hydrocarbons in water. The chemical transformation of Cu was followed *in situ* using LSPR spectroscopy.

Keywords

Photocatalysis, TiO₂, carbon, graphene, graphite, localized surface plasmon resonance, nanocomposites, photocatalytic mechanisms, solar energy conversion

List of Appended Papers

This thesis is based on the work presented in the following publications.

Paper I: **Preparation and Characterization of TiO₂/Carbon Composite Thin Films with Enhanced Photocatalytic Activity**

Raja Sellappan, Jiefang Zhu, Hans Fredriksson, Rafael Silva Martins, Michael Zäch, and Dinko Chakarov

Journal of Molecular Catalysis A: Chemical 335 (2011) 136–144

Contributions: Prepared samples, performed all the experimental work except XRD, and wrote the first draft of the manuscript (MS).

Paper II: **On the Mechanism of Enhanced Photocatalytic Activity of Composite TiO₂/Carbon Nanofilms**

Raja Sellappan, Augustinas Galeckas, Vishnukanthan Venkatachalapathy, Andrej Yu Kuznetsov, and Dinko Chakarov

Journal of Applied Catalysis B: Environmental 106 (2011) 337- 342

Contributions: Prepared samples, performed all the experimental work except TRPL measurements, and wrote the first draft of the MS.

Paper III: **Influence of Graphene Synthesizing Techniques on the Photocatalytic Performance of Graphene/TiO₂ Nanocomposites**

Raja Sellappan, Jie Sun, Augustinas Galeckas, August Yurgens, Andrej Yu Kuznetsov, and Dinko Chakarov

Submitted to Physical Chemistry Chemical Physics, 2013

Contributions: Prepared all samples except CVD graphene, performed all the experimental work except TRPL measurements, and wrote the first draft of the MS.

Paper IV: **Effects of Plasmon Excitation on Photocatalytic Activity of Ag/TiO₂ and Au/TiO₂ Nanocomposites**

Raja Sellappan, Morten Godtfred Nielsen, Fernando González-Posada, Peter C. K. Vesborg, Ib Chorkendorff, and Dinko Chakarov

Submitted to Journal of Catalysis, 2013

Contributions: Prepared all samples, performed all the experimental work except the ethylene photooxidation test, and wrote the first draft of the MS.

Paper V: **Oxidation of Copper Nanoparticles in Water Monitored *in situ* by Localized Surface Plasmon Resonance Spectroscopy**

Fernando González-Posada, Raja Sellappan, Bert Vanpoucke, and Dinko Chakarov

Submitted to *Nanoscale*, 2013

Contributions: Participated in sample preparation, experimental work and the discussion of the results.

Other Papers not Included in the Thesis

Paper VI: **Tuning Light Absorption by Bandgap Engineering in ZnCdO as a Function of MOVPE Synthesis Conditions and Annealing**

Vishnukanthan Venkatachalapathy, Augustinas Galeckas, Raja Sellappan, Dinko Chakarov, and Andrej Yu Kuznetsov.

Journal of Crystal Growth 315 (2011) 301–304.

Paper VII: **Nanostructures for Enhanced Light Absorption in Solar Energy Devices**

Gustav Edman Jonsson, Hans Fredriksson, Raja Sellappan, and Dinko Chakarov

International Journal of Photoenergy 2011 (2011) 939807.

To
Mother Nature
'For being a source of inspiration and experience'

Table of Contents

Abstract.....	III
List of Appended Papers.....	IV
1. Introduction.....	1
1.1 Background.....	1
1.2 Photocatalysis	2
1.3 Why is TiO ₂ Photocatalyst?.....	3
1.4 Nanoscience and Nanotechnology Approaches.....	4
1.5 Scope of the Thesis.....	5
2. Fundamental Photocatalytic Processes.....	7
2.1 Basic Concepts of Photocatalysis.....	7
2.2 Electronic Band Structure of Solids.....	7
2.3 Elementary Steps in Heterogeneous Photocatalytic Systems.....	9
2.3.1 Light Absorption and Generation of Charge Carriers.....	9
2.3.2 Charge Separation, Trapping, and Transport.....	11
2.3.2.1 Charge Carrier Recombination.....	12
2.3.2.2 Charge Carrier Trapping.....	12
2.3.2.3 Charge Transport.....	13
2.3.3 Chemical Reactions at the Surface.....	14
2.3.3.1 Band Bending.....	15
2.3.3.2 Surface Active Sites.....	17
2.4 Titanium dioxide Properties.....	18
2.4.1 Bulk Properties.....	18
2.4.2 TiO ₂ Nanostructures.....	20
2.5 Approaches to Improve TiO ₂ Photocatalytic Performance.....	20
2.5.1 Bandgap Engineering and Photosensitization.....	21
2.5.2 Optimization of the Charge Transport.....	22
2.5.3 Optimization of the Surface Area.....	23
3. Experimental Methods.....	25
3.1 Deposition Methods.....	25
3.2 Physical Vapor Deposition.....	25
3.2.1 Electron Beam Evaporation.....	25
3.2.2 Sputtering.....	26
3.3 Chemical Vapor Deposition.....	26
3.4 Nanofabrication Techniques.....	27
3.4.1 Hole-mask Colloidal Lithography.....	27
3.5 Annealing Treatments.....	28
3.6 Analytical and Characterization Techniques.....	29

3.6.1	Scanning Electron Microscope.....	29
3.6.2	Atomic Force Microscopy.....	31
3.6.3	UV-VIS-NIR Spectrophotometer.....	32
3.6.4	Photoluminescence Spectroscopy.....	34
3.6.5	LSPR Spectroscopy.....	35
3.6.6	Raman Spectroscopy.....	36
3.6.7	X-Ray Diffraction and X-ray Photoelectron Spectroscopy...	38
3.6.8	Gas Phase Chemical Reactor.....	39
3.6.9	Mass Spectrometry.....	39
3.7	Experimental Setup for the Photocatalytic Tests.....	40
4.	Nanocomposite Photocatalysts.....	43
4.1	Nanocomposites with Carbon and Optically Active Metal NPs.....	43
4.2	TiO ₂ /Carbon Nanocomposites.....	44
4.2.1	Graphite.....	44
4.2.2	Graphitic-like Carbon.....	45
4.2.3	Graphene.....	47
4.2.4	Role of Carbonaceous Materials in TiO ₂ Photocatalysis.....	47
4.3	TiO ₂ /Metal Nanocomposites.....	50
4.3.1	Metals as co-catalysts.....	50
4.3.2	Metals at Nanoscale.....	50
4.3.3	Localized Surface Plasmon Resonance.....	50
4.3.4	Plasmonic Energy/Charge Transfer Mechanisms in TiO ₂	53
4.4	TiO ₂ /Cu Nanocomposites.....	57
5.	Summary of Results.....	61
5.1	Summary of Appended Papers.....	61
5.2	Summary of Unpublished Results.....	65
6.	Conclusions and Outlook.....	67
	Appendix.....	71
A1:	TiO ₂ /Carbon Nanostructures by HCL.....	71
A2:	TiO ₂ /Metal Nanocomposites by HCL.....	75
A3:	TiO ₂ /Metal Nanocomposites by Thermal Evaporation.....	78
A4:	Effects of Hole Scavenger on Charge Transfer.....	83
	Acknowledgements.....	85
	References.....	87

1. Introduction

1.1. Background

Provision of sustainable energy is essential for the global economic development and human well-being. More than 80% of our current energy production comes from carbon-based fossil fuels such as coal, oil, and natural gas[1, 2]. We utilize energy mainly in the form of electricity and liquid fuels, which are used for domestic, commercial, industrial, and transportation sectors. Although these carbon-based fuels can supply energy for another century or may be several hundred years[2], continuous reliance on them will cause severe problems to our economy and environment. Economic problems are predicted to arise from a steady increase of oil prices because of continuous demand but restricted supply. Environmental problems, such as global warming, are mainly caused by increase in man-made (anthropogenic) carbon dioxide in the atmosphere originating from burning of fossil fuels. The global energy demand is projected to double by 2050[2] due to growing population and increased living standards of people in the developing countries. So, the global community has to work harder towards finding alternative ways to tackle shortage in energy supply and associated challenges. One potential way to meet these challenges is to derive energy from renewable sources such as solar radiation, wind, hydroelectric power, etc.

Solar energy is by far the most abundant energy source. It can be the potential replacement to fossil fuels. It provides not only carbon-neutral energy but may also fulfill future energy demands. The amount of solar radiation striking our earth surface is about 3×10^{24} joules/year which is 10^4 times higher than the current global population consumption rate[3]. Albeit the amount of solar energy is tremendous, it only constitutes roughly less than 1% (photovoltaic and concentrated solar power plants)[4] in the global energy production in 2011. Though there are several ways to transform solar energy into some useful energy, direct conversion by photovoltaic cells to electricity is the yet most exploited route. However, solar photovoltaics technology sets some limitations due to the fact that the sunlight is not continuous throughout the day (intermittency) as well as due to inefficiency and lack of large scale solutions to store electricity[5]. In this respect, direct conversion of solar energy by photoelectrochemical cells to chemical (solar) fuels, such as hydrogen from water splitting or hydrocarbon fuels from CO_2 photoreduction, is attractive and promising routes to store solar energy in the form of chemical energy. Solar fuels can be used not only directly for automobile applications but also for domestic applications producing electricity by fuel cells. This technology is economically feasible, environmentally safe, and will supply energy continuously throughout the day even when there is no sunlight[6, 7]. The chemical process involved in this conversion route mimics the natural photosynthetic process and is often called artificial photosynthesis. The heart

1. Introduction

of solar energy conversion in the artificial photosynthesis process is the light harvesting material called *photocatalyst*, which is the central part of this thesis.

1.2. Photocatalysis

The dawn of photocatalysis is dated back to more than 80 years with the observations of the chalking of TiO₂ based paints and darkening of metal oxides in contact with organic substance in sunlight [8]. This field gained prominent attentions in 1972 after the pioneering work of Fujishimna and Honda on photocatalytic water splitting on a single crystalline TiO₂ photocatalyst. This event paved the way for a new era in the field of photocatalysis. Ever since the field is growing continuously (**Figure 1.1**) with variations that follow closely the world energy demand and supply.

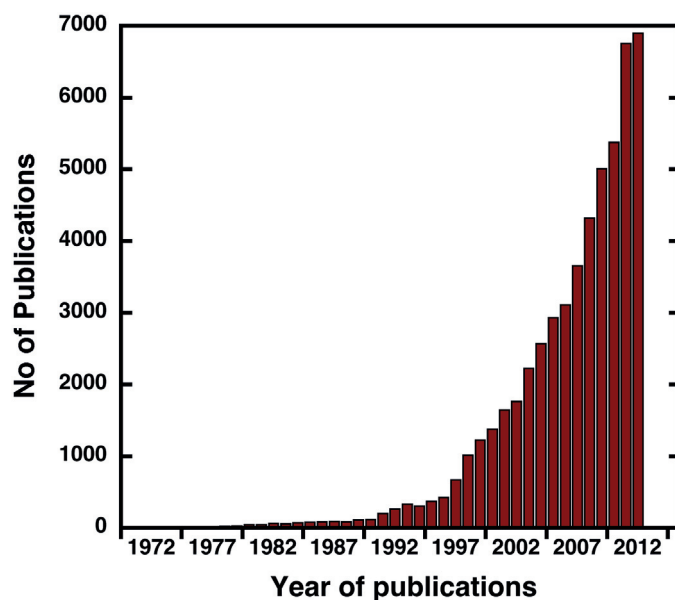


Figure 1.1: Chart illustrating volume of research work carried out each year in the field of photocatalysis. An interest in photocatalysis is growing exponentially and overwhelmingly. Source: ISI web of knowledge with the search keyword '*photocatal**' from the year 1972 to 2012.

Photocatalysis, by definition, 'is a change in the rate of chemical reactions or their generation under the action of light in the presence of substances called photocatalysts that absorb light quanta and are involved in the chemical transformations of the reaction participants'[9]. So, photocatalysis is a term used to refer to a chemical reaction which utilizes light to activate a chemical substance which, in turn, usually accelerates the rate of the reaction without being modified itself [10].

1.3. Why is TiO₂ Photocatalyst?

From an energetic viewpoint, photocatalytic reactions are classified into uphill reactions and downhill reactions[11]. In the uphill reactions, the photon energy is converted into highly energetic chemical compounds than the reactants. Examples are hydrogen from water splitting, methanol from CO₂ photoreduction, etc. These reactions are highly endothermic and referred to as artificial photosynthesis or photosynthetic reactions[11]. In the downhill reactions, the photon energy is used to induce degradation in chemical compounds and the resulting products are with lower energy than the reactants. These reactions are highly exothermic and referred to as photon-induced reaction[11]. Examples are organic compounds oxidation, carbon monoxide oxidation, etc.

Semiconductors are usually employed as photocatalysts since they have bandgaps (E_g), which make photoexcited electrons live longer and thereby have higher chance to promote a chemical reaction, compared to a metal. Most interesting are semiconductors with bandgaps corresponding to optical frequencies ($h\nu \sim 350$ to 1100 nm). The basic elementary processes of a semiconductor photocatalyst (discussed in the chapter 2) are[12]:

- (i) Light absorption and electron-hole pair generation
- (ii) Charge separation and transport
- (iii) Chemical reactions at the surface

These processes govern the performance of any photocatalytic systems. Their optimization is crucial in order to improve the efficiency of the photocatalytic systems.

1.3. Why is TiO₂ Photocatalyst?

Among the many investigated photocatalyst materials for the past decades, TiO₂ remains a most popular candidate for applications in solar cells[13], solar fuels[14], and environmental cleaning[15]. It is due to its outstanding and unique physiochemical properties. Among others, TiO₂ exhibits remarkable resistance to corrosion and photocorrosion especially in harsh aqueous environments[16]. The valence band hole has a strong oxidation potential towards environmental toxic substances. The properties of TiO₂ can be widely altered by introducing defects in the crystal lattice (alteration of stoichiometry) and by doping[17-19]. TiO₂ is much cheaper than other photosensitive materials and its reserves are abundant. All these factors, so far, make TiO₂ superior for energy and environmental applications in comparison to other heterogeneous photocatalysts[20].

1. Introduction

The applications of TiO₂ photocatalysts can be categorized into two areas: (i) Environmental remedy and (ii) Solar fuels applications. Some of its important applications are listed below.

1. Self-cleaning of building materials (windows, walls, etc)[20]
2. Air purification[20]
3. Water purification and degradation of organic compounds[20]
4. Solar water splitting [21] and Photovoltaics [3, 22]
5. Photoreduction of CO₂ to hydrocarbon fuels[23]
6. Sensors (oxygen gas sensors)[24]
7. Anti-fogging mirror[20]
8. Pigments in paints and coatings[20]

1.4. Nanoscience and Nanotechnology Approaches

Nanoscience (NS) and nanotechnology (NT) are scientific and engineering branches dealing with manipulation of materials on the nanoscale (1 to 100 nm) and the size related phenomena in them. The term NT refers not only to the size reduction of materials but also to the controlled manipulation of atoms and molecules in the materials. The properties possessed by nanomaterials can be entirely different from those exhibited by the bulk materials. When the material object's size goes down to the nanoscale, quantum mechanical effects and surface properties come into play more dominantly. For example, gold metal exhibits good catalytic properties on the nanoscale of 1 to 2 nm, but it is normally not observed on the macro scale[25, 26]. Thus, NT allows one to design and tailor make functional materials that are able to replicate some natural processes, for instance photosynthesis [27]. One important feature of NT in the realm of photocatalysis is that it offers substantially higher surface to volume ratio. This extensively helps minimizing charge carrier recombination before the charge carriers have the chance to induce a chemical reaction, and increases the surface area of the photocatalysts[28]. From a practical point of view, the miniaturization of devices also has several advantages such as less material consumption, compactness, etc. Metals such as gold (Au), silver (Ag), copper (Cu), etc., on the nanoscale exhibit localized surface plasmon resonance (LSPR), i.e. collective and coherent oscillations of the conduction electrons at optical frequencies[29]. The LSPR of metal nanoparticles (NPs) has generated a lot of attention and interest in the photocatalytic field due to its potential to enhance photocatalytic performance[30, 31]. Overall, NS and NT have the great capacity to contribute to the improvement of photocatalytic elementary processes.

1.5. Scope of the Thesis

As mentioned above, TiO_2 possesses some outstanding properties for energy and environmental remedy applications. However, it suffers greatly in

- (i) Fast electron-hole pair recombination
- (ii) Light absorption only in the ultraviolet (UV) region

The bandgap of TiO_2 is about 3.2 eV (anatase), so it absorbs light only in the UV part of the solar spectrum. This part accounts for only 4% in the total incoming solar radiation. Hence for solar radiation related applications, it is essential to extend the light absorption of TiO_2 to the visible region, which accounts for about 42% in the incoming radiation. The fast e-h pair recombination in TiO_2 is also an undesirable process because the absorbed energy is wasted as heat or reemitted without doing any chemical work. These two inherent properties are major reasons for the low quantum efficiency and are obstacles for the practical applications of TiO_2 .

There are several approaches to substantially alleviate these problems. In this thesis, two different model TiO_2 based nanocomposite systems have been designed and prepared to address the issues of charge carrier dynamics and light absorption. Special attention has been paid to understanding the underlying mechanisms of the enhanced photocatalytic activity. The prepared photocatalysts are:

- (i) TiO_2 /Carbon nanocomposites
- (ii) TiO_2 /Metal nanocomposites

TiO_2 /Carbon nanocomposites: This model system has been designed to address the role and mechanism of electrically conductive carbon films in the form of graphite and graphene on the photocatalytic performance of TiO_2 nanocrystalline films. Special importance has been given to understanding the charge carrier dynamics and interfacial effects of carbon beneath TiO_2 . A significant attention has been devoted to understanding the role of synthesizing techniques of graphene on the TiO_2 photocatalytic performance.

TiO_2 /Metal nanocomposites: This model system has been designed to address the role of LSPR related effects, exhibited by metal nanoparticles (NPs), on the photocatalytic performance of undoped TiO_2 nanocrystalline films. The chosen metal NPs in this study were Ag and Au, since they have excellent plasmonic properties in the near UV, visible and near infrared region. The metal NPs have been intentionally placed onto, isolated from, and beneath TiO_2 in order to elucidate different effects associated with LSPR. Great emphasis has been given to irradiation conditions of the composite systems over

1. Introduction

different spectral regions with the aim of distinguishing the bandgap excitation from the plasmonic excitation.

TiO₂/Cu nanocomposite has been fabricated for photocatalytic reduction of carbon dioxide to hydrocarbon fuels using water and solar energy. In this photocatalytic system, Cu NPs were placed onto TiO₂ to address the role of Cu chemical stability in aqueous environment under the bandgap illumination of TiO₂. The stability of Cu has been *in situ* monitored by LSPR spectroscopy techniques.

All composite photocatalysts have been tested with the photon-induced downhill reactions. Gas phase methanol photooxidation has been chosen as a model reaction to test the performance of the prepared model photocatalysts.

To summarize, the aim of the thesis was to design, fabricate, and test model TiO₂ based photocatalysts with the aim of optimizing their performance through understandings of the mechanisms for enhanced photocatalytic activity.

2. Fundamental Photocatalytic Process

Heterogeneous photocatalytic system, where the photocatalysts and the reactants are in different phases, represents a central part in an artificial photosynthesis scheme for conversion of solar energy into usable chemical energy. This chapter outlines the fundamental aspects of the heterogeneous photocatalytic process, which are also central in the thesis. Light absorption and charge carrier generation, separation and transportation of charge carriers, and chemical redox reaction driven by transported charge carriers at the surface are regarded as the basic elementary steps in any heterogeneous photocatalytic process. Understanding of them will therefore provide useful insights into the field of heterogeneous photocatalysis. Since TiO_2 has been the choice of material in this thesis, most of the details described in this chapter pertain to its inherent properties and related phenomena.

2.1. Basic Concepts of Photocatalysis

A photocatalyst is a substance that is able to produce chemical transformations of the reaction partners upon absorption of light. The excited state of the photocatalyst repeatedly interacts with the reaction partners forming reaction intermediates and/or products and regenerates itself after each cycle of such interactions[32].

Photocatalysts are classified into homogeneous and heterogeneous systems depending on the photocatalysts' phase with respect to the reactants. In homogeneous system, both the reactants and the photocatalysts are in the same phase whereas in heterogeneous system, the photocatalysts exist in solid phase and the reactants exist in liquid or gas phase. The latter plays central role in solar energy transformation processes since Fujishima's and Honda's pioneering work[21]. Heterogeneous photocatalytic system has intensively been studied for many years because of its potential use in energy[11, 12, 33] and environmental related applications[15]. It is essential to understand microscopic properties of solids especially electronic structure in order to explain the observed macroscopic phenomena in heterogeneous photocatalytic systems.

2.2. Electronic Band Structure of Solids

Solids are generally classified into metals, semiconductors, and insulators based on the nature of their electronic band structure. In general, electronic bands represent sets of allowed energy state ranges that electrons can populate in a solid. Normally, a solid has several numbers of energy bands but the important ones, for the discussion here, are the valence band (VB) and conduction bands (CB), i.e. the highest populated and lowest unpopulated bands (in equilibrium at room temperature). According to the Pauli

2. Fundamental Photocatalytic Process

exclusion principle, no two identical fermions (in our case electrons) may have the same quantum state simultaneously. Therefore, the electrons start to fill up and distribute from the lowest energy levels and up. Electrons that occupy highest energy states or orbitals at absolute zero temperature (0 K) constitute the VB. The energy of the highest and occupied electron state at 0 K is called the Fermi energy. The band of orbitals or states, above the filled VB, that are higher in energy and empty (at 0 K) where the electrons can move freely, if they are excited to these energies, are called the CB. In between the valence band maximum and the conduction band minimum there is a forbidden energy gap called the bandgap, where no electrons can accommodate. As illustrated schematically in **Figure 2.1**, electronic classification of solids stems from how the VB and the CB are positioned with respect to the energy of electrons. In metals, the VB and the CB partially overlap with each other, and there is, thus, no bandgap or forbidden range of energies, which is the reason metals are excellent conductors, while semiconductors at 0 K are insulators.

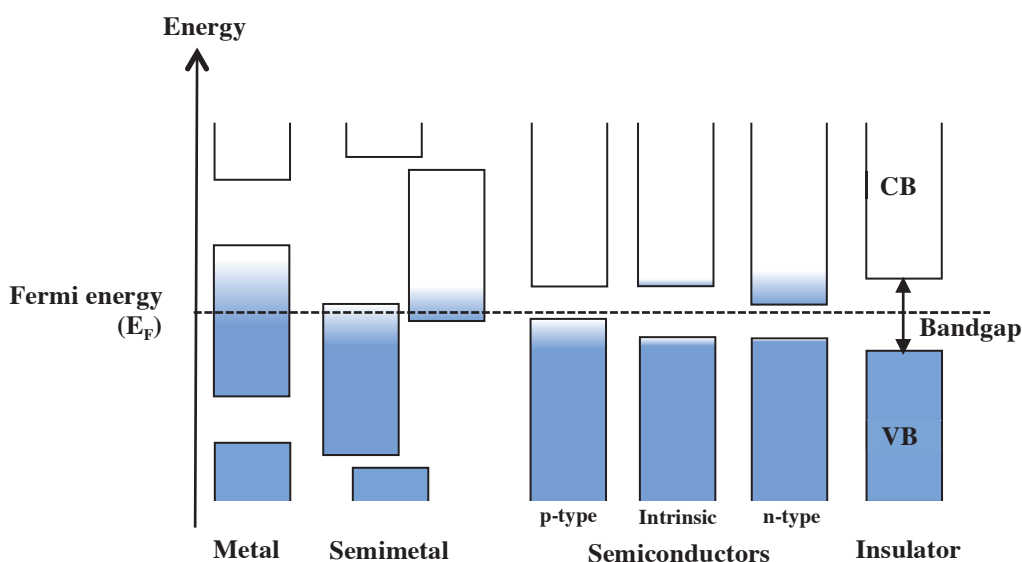


Figure 2.1: Schematic representation of the electronic band structure of metals, semiconductors, and insulators. Note there is an overlapping of the VB and the CB in metals or semimetals whereas in semiconductors and insulators they are separated by a forbidden energy gap. The diagram is adapted from Wikipedia.

In semimetals, the VB and CB overlap is small and need not occur at the same wavevector (k) in the Brillouin zone. Moreover, the density of states at the Fermi energy is lower compared to metals. In semiconductors and insulators, the VB and the CB are separated by a forbidden energy gap. The states in the VB are completely filled ($T = 0$ K) or almost filled ($T > 0$ K). In semiconductors, the origin of electrical conductivity at RT comes from thermal excitation of some electrons from the VB to the CB. The conductivity is very low in comparison to metals and hence the material is called a

2.3. Elementary Steps in Heterogeneous Photocatalytic Systems

semiconductor. Conductivity in semiconductors, however, can be improved by doping with foreign atoms. Depending on the dopants, the semiconductors can be divided into p-type and n-type semiconductors. The former are dominated by holes in the VB carrying the current. These holes are created by electron excitation to the dopant atoms, which have their energy levels just above but very close to the VB. In n-doped semiconductors, electrical conductivity is dominated by electrons in the CB. The electrons are excited from the dopant atoms, which have electron levels just below the CB band edge. The energy bandgap of different semiconductors varies from ~ 1 eV to 4 eV. In insulators, the forbidden bandgap is higher than in semiconductors and as a result RT thermal energy is not enough to promote the electrons from the VB to the CB. So, the electrical conductivity is not possible in insulators.

2.3. Elementary Steps in Heterogeneous Photocatalytic Systems

2.3.1. Light Absorption and Generation of Charge Carriers

Light is an electromagnetic radiation, which is visible to the human eye in the wavelength range from 400 nm to 700 nm. All electromagnetic radiation has dual characteristics of wave and particle nature. The particle nature of light is characterized by the photon, the elementary particle of light, with energy $E=h\nu$, where h is the Planck's constant. The wave nature of light is characterized by a wavelength (λ), a frequency (ν), and a velocity (c), which are related as $C=\lambda\nu$. Light can, thus, be perceived as an electromagnetic wave or collection of photons propagating through space.

The electromagnetic radiation discussed here spans from the near ultraviolet to visible to near infrared (UV-VIS-NIR) ranges. In terms of energy (wavelength), this is radiation from ~ 4.1 eV (300 nm) to ~ 1 eV (1200 nm). In general, most of the chemical transformation occurs in these energy ranges. Intrinsic semiconductors naturally have their bandgaps corresponding to these ranges. More interestingly, the part of the solar spectrum that reaches earth falls into these energy ranges and thus making semiconductors important and interesting functional materials for solar energy transformation applications.

Semiconductors are the most widely used materials as heterogeneous photocatalysts: however, there some exceptions exist. For instance, smaller optically active supported metal NPs have recently been realized as *plasmonic photocatalysts* in solar energy transformation processes[31, 34]. **Figure 2.2** illustrates the interaction of light with a bulk semiconductor.

2. Fundamental Photocatalytic Process

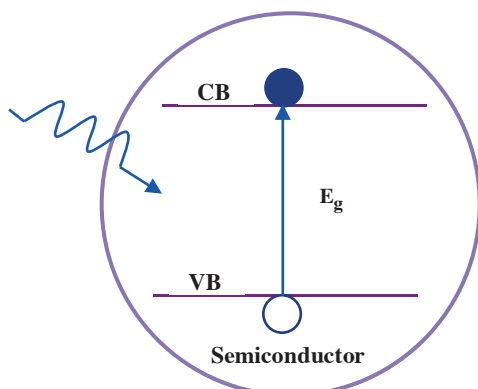


Figure 2.2: Schematic illustration of the first elementary step in a photocatalytic process: the absorption of light in a semiconductor and the subsequent generation of an e-h pair. This is possible for light with energy equal to or greater than the bandgap.

As discussed earlier, a semiconductor is characterized by the filled VB and the empty CB separated by a forbidden energy bandgap (E_g). As far as light absorption in the semiconductor is concerned, the bandgap width and the position of the valence band maximum (VBM) and the conduction band minimum (CBM) have great implications. The width of the bandgap depends strongly on the electronic structure of the constituent atoms in the material. Electronic band structure is generally represented as energy (E) versus momentum (k -vector) of the states that electrons or holes can occupy in a solid, often simply referred to as the E - k diagram. In a direct bandgap semiconductor, the VBM and the CBM lie at the same k vector whereas in an indirect bandgap semiconductor, they lie at different k values (see **Figure 2.3 (a)**). When a photon with energy equal to or greater than the bandgap impinges on a semiconductor, it can excite an electron to the CB and leave a positive hole behind in the VB. This process occurs under the restrictions of energy and momentum conservation. Photons travel at the speed of light, so they have very little or negligible momentum relative to the electrons' momentum in a crystal. This makes electronic transition "vertical" in the E - K diagram, i.e. the initial and final states have the same k vector (exceptions are phonon assisted transitions)[35]. This type of band-to-band transition is called *interband* transition, since it involves two different bands contrary to *intra-band* transition, where the transition takes place within the same band. In the direct bandgap material, as both the VBM and the CBM lie at the same k -vector, light penetration depth is lower at the bandgap energy since all light is absorbed close to the surface. In such a case, thin films are enough to absorb more photons. In an indirect bandgap material, the VBM and the CBM lie at different k -vector (see **Figure 2.3 (b)**). In this case, light absorption is assisted by a third (quasi)particle called phonon (lattice vibration) in order to conserve energy and momentum. Phonons have much higher momentum and much lower energy compared to photons in the visible range[35]. Since phonons must assist absorption or emission, the light penetration depth is larger in these materials and it is temperature dependent. In other words, the absorption coefficient is less at the bandgap energy or close to it, so thicker films are needed to absorb more photons.

2.3. Elementary Steps in Heterogeneous Photocatalytic Systems

The absorption spectrum in semiconductors is typically broad as it may involve all states[36]. The light absorption process results in creating electrically neutral excitons (bound e-h pairs) or unbound charged e-h pairs (free). The excitons are a bound state of e-h pair attracted to each other through electrostatic columbic attraction. Excitons in semiconductors (where the dielectric constant is usually large) are called Wannier-Mott excitons and have binding energies on the order of ~ 10 meV. Excitons are stable at lower temperature and are ionized into free electrons and holes at RT, since thermal energy at RT is about ~ 25 meV.

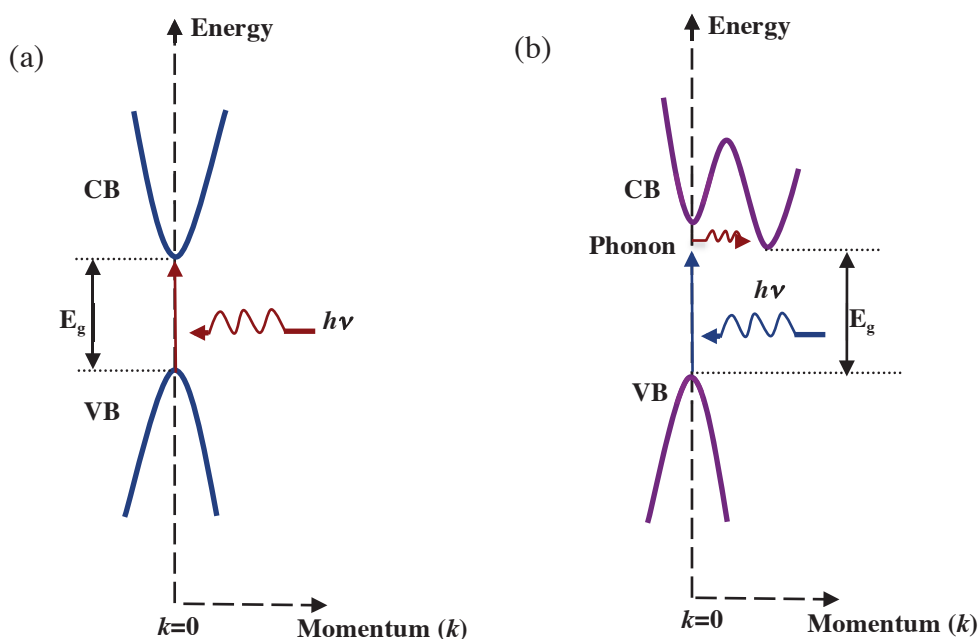


Figure 2.3: Illustration of an interband transition in a (a) direct and (b) indirect bandgap semiconductor. Upward arrow represents the photon absorption. Light absorption in (b) is executed by a photon and a phonon in combination to conserve momentum and energy.

2.3.2. Charge Separation, Trapping, and Transport

The light absorption in semiconductors promotes electrons from the VB to the CB and leaves behind positive holes in the VB or creates e-h pairs. The fate of photogenerated charge carriers could follow several pathways depending on the physical circumstances (see **Figure 2.4**). The lifetime of the charge carriers in the excited state, i.e. the time it can live in the excited state, is on the order of nanoseconds[37] in semiconductors in contrast to femtoseconds in metals. This second elementary step in the photocatalytic process encompasses several sub-processes, each of which is briefly described below.

2. Fundamental Photocatalytic Process

2.3.2.1. Charge Carrier Recombination

Charge carrier recombination is an undesired process because it hinders the efficiency of a photocatalytic system. This undesired process is strongly competing with the desired charge transfer process to the adsorbates on the surface[37]. Factors such as impurities, defects, degree of crystallinity, surfaces, etc., are important to account for recombination of charge carriers. There are several ways to minimize charge carrier recombination. Examples are incorporation of metal particles, manipulation of interfacial junctions, adding dopants, and trapping sites[38].

Charge carrier recombination results in dissipation of the absorbed energy in the form of heat (non-radiative) or photon emission (radiative). It is hard to quantify precisely the relative degrees of radiative and non-radiative recombination. It is also hard to measure directly the amount of non-radiative recombination[38]. However, the radiative recombination probability can be quantified from photoluminescence studies and can be used to assess charge carrier dynamics and to estimate the lifetime of charge carriers of the photocatalyst.

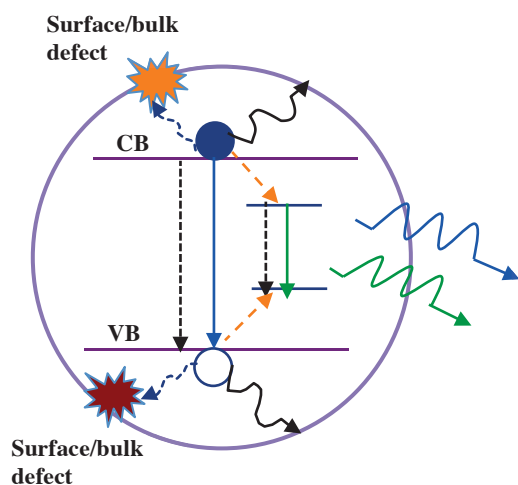


Figure 2.4: Schematic illustration of the second elementary step in a photocatalytic process. After the e-h pair generation, charge carriers follow different paths. The dotted lines/curves and the solid lines represent non-radiative (volume/surface) and radiative recombination of charge carriers, respectively. The solid curves represent charge carrier transfer process to the adsorbates.

2.3.2.2. Charge Carrier Trapping

As mentioned previously, photogenerated charge carriers in semiconductors are the ones that mediate the desired chemical reactions. In some photocatalytic reactions, it is the holes (or vice versa) that induce the desired chemical reactions. In such situations, the electrons (or vice versa) may need to be trapped because they can otherwise recombine with the desirable carrier type. The charge carrier recombination rate can, thus, be

2.3. Elementary Steps in Heterogeneous Photocatalytic Systems

suppressed with the help of trapping sites, since it helps increasing the charge carrier lifetime of TiO_2 [37].

Charge carrier trapping is the capturing of photogenerated electrons or holes in trap sites at the surface and in the bulk of the semiconductor. Trapping could be beneficial if the charge carriers are localized at important electron transfer sites on the TiO_2 surface or if it promoted charge carrier separation. Trapping conversely could be detrimental if the trapping sites are far from preferred electron transfer sites[38].

Trapping occurs normally at irregularities caused by lattice imperfections both at the surface and in the bulk. Depending on the energy associated with the trapping sites, it is characterized as shallow trapping or deep trapping. Shallow trapping sites exist just below the CBM or above the VBM. The energy associated with these trapping sites is close to the energy of thermal excitations. Detrapping (release of trapped carriers) of charge carrier in shallow sites is activated by thermal excitation at RT. Surface states are one example of shallow trapping sites, which occur normally due to the presence of dangling bond(s) at the surface. Bulk trapping sites exist in the bandgap and the energy associated with them with respect to the CBM or the VBM is often higher than thermal excitation at a given temperature[39]. Trapping sites are localized and their occurrence depends strongly on the preparation methods. Reduction of TiO_2 or annealing it in vacuum creates oxygen vacancies or localized Ti^{3+} sites at the surface[40-42]. These oxygen vacancies are the main trapping sites for the photogenerated electrons in TiO_2 photocatalysts. These surface trapping sites play a significant role in influencing the performance of TiO_2 under different circumstances especially under oxygen lean conditions or when the surface is fully bound with or blocked by organic compounds. In other words, they can be simply regarded as electron storage sites[38]. Although the nature of hole trapping sites remains unclear, it is assumed that hole scavengers such as organic compounds and OH^\cdot species initiate the hole trapping. However, several studies point out that $\text{Ti}^{4+}\text{-O}^\cdot$ site is the most possible sites, where hole resides on an under-coordinated oxygen atom at the surface[38]. A few recent studies propose that the hole trapping sites exist preferably in the near-surface region contrary to bulk or on surface sites[38]. Overall, the trapping sites in TiO_2 have the capacity to determine the performance of photocatalytic activity.

2.3.2.3. Charge Transport

As soon as the e-h pairs are generated by light absorption, the photogenerated charge carriers should preferably be separated and transported to the surface in order to induce desired chemical processes. The primary driving forces that transfer the photogenerated charge carriers to the surface on the macroscopic scale are diffusion, resulting from

2. Fundamental Photocatalytic Process

gradients of charge carriers, and drift (mobility) due to force exerted on charge carrier by an electric field. Depending on the nature of the photocatalyst system, either one or both of the processes could contribute to the transfer of charge carrier. In a typical heterogeneous photocatalytic system, there is generally an electric field created at the interface between the photocatalyst and the reactants due to band bending. If the band bending is of the right sign, it will accelerate the desired charge carriers to the surface and vice versa. As a result of this, after the generation of e-h pairs in the bulk, charge carriers first will diffuse over certain distances (if excitation occurs deeper into the semiconductor than the distance over which band bending occurs) and then if they are close to the interface, the electric field will drift them further away.

The extent to which charge carriers are effectively transported depends on the nature of materials' electronic and crystal structure. If the crystal is perfect, the band states in the VB or CB represent travelling states, that is states allowing the holes or electrons to move almost like free electrons, except that the motion occurs as if the electron (hole) had different effective mass. This problem can be further simplified by assuming the concept of electrons effective mass. Higher effective mass of charge carriers leads to lower charge transfer and vice versa. The effective mass approach is valid under the influence of electric field. However, in the real case, i.e. in a non-perfect crystal, impurities, defects in the lattice, crystallinity defects, etc., will scatter charge carriers strongly and hinder their movement to a great extent. The average distance over which charge carriers move without experiencing any scattering or collisions from defects is called the mean free path of charge carriers and the corresponding time it takes between such collisions or scattering events is called the mean free time.

TiO₂ represents a mixed nature of ionic and covalent bonding[40]. The ionic nature of TiO₂ causes a strong interaction of photogenerated electrons with the lattice, resulting in formation of quasiparticles called polarons i.e. electrons accompanying lattice polarization and/or distortion. Strong interaction of electrons with the lattice leads to more localized, self-trapped polarons whereas the weak interaction leads to formation of less confined polarons with effective wavefunctions that extend beyond the dimension of a unit cell[43]. In the former case, the charge is transported through hopping from one site to the next sites whereas the latter case exhibits the band type transport but with an enhanced mass relative to the band mass of an electron[43].

2.3.3. Chemical Reactions at the Surface

Once the charge carriers arrive at the interface with the reactive medium, they may take part in redox reactions (**Figure 2.5**). This elementary step involves transfer of the charge carriers between the surface of the photocatalyst and the adsorbed chemical species. This

2.3. Elementary Steps in Heterogeneous Photocatalytic Systems

transfer process is called interfacial charge transfer and is a central process in the heterogeneous photocatalytic scheme. There are several governing parameters that determine charge carrier transfer across the interface. The most important one is how well the energy level positions of the semiconductor and the adsorbed species match each other. The energy level position of different semiconductors with respect to the redox potential of water is shown in **Figure 2.6**.

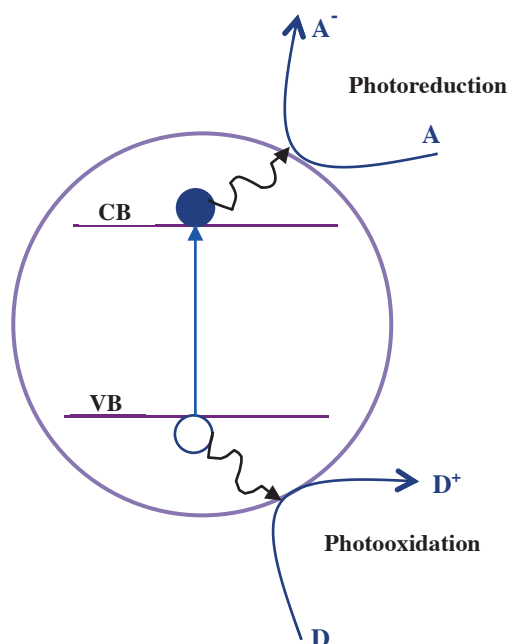


Figure 2.5: Schematic representation of the third elementary step in a photocatalytic process. The photogenerated electron takes part in reduction whereas the hole takes part in oxidation reaction.

In order for an electron transfer to occur, for example in TiO_2 , the position of the CBM should be higher than the reduction potential of the adsorbed acceptor species. For a hole transfer to occur, the position of the VBM should be lower than oxidation potential of the adsorbed donor species. The transfer of photogenerated electrons from the CB of the photocatalyst to the acceptor is referred to as photoreduction whereas the transfer of electrons from the donor to the VB of the photocatalyst is referred to as photooxidation. The electron and hole transfer processes should occur (almost) simultaneously in order to regenerate the photocatalyst otherwise charging effects would occur.

2.3.3.1. Band Bending

When a semiconductor is in contact with another phase such as liquid, gas or metal, Fermi level equilibration thermodynamically occurs by redistribution of the charge carriers from the lower work function side to the higher work function side. This can be explained clearly in the example of contact between a metal and an n-type semiconductor. Assume that the metal work function is higher than the semiconductor work function. In this case, the electrons will flow from the semiconductor to the metal

2. Fundamental Photocatalytic Process

side until their Fermi level aligns. As a consequence, a space charge layer or double layer is built-up at the interface where more excess negative charge carriers are present on the metal side and more positive carriers exist on the semiconductor side. This situation is similar to formation of electric dipoles across the interface, which in turn creates an electric field in the space charge region. The space charge region has great implications

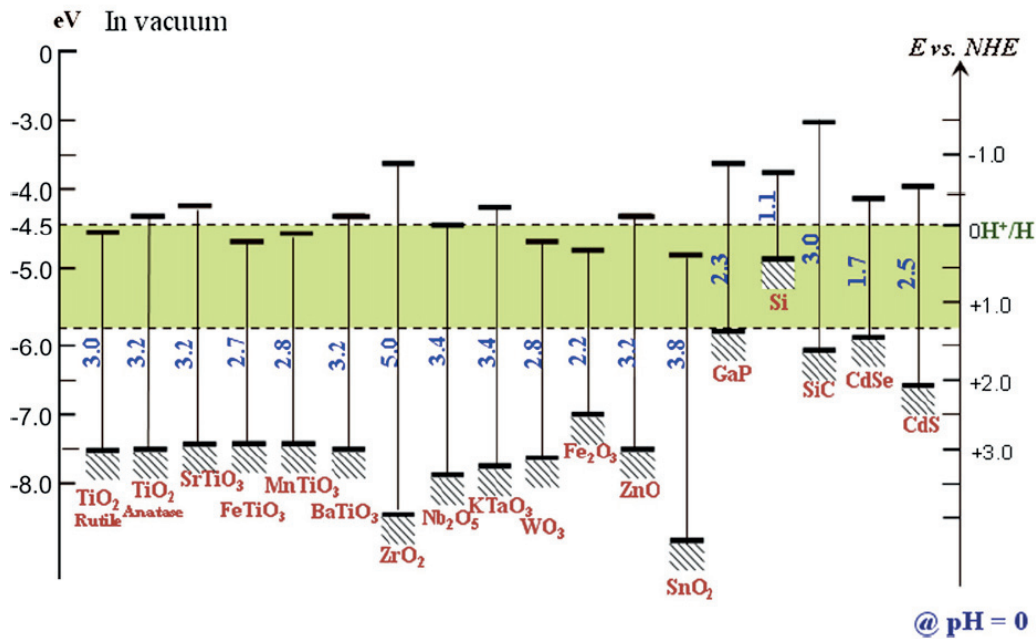


Figure 2.6: Schematic representation of energy band positions of different semiconductors versus standard hydrogen electrode potential (NHE) and vacuum energy level at pH=0 [44]

in suppressing charge carrier recombination due to the presence of the electric field. Following the Fermi level alignment and subsequent migration of charge carriers from the semiconductor, the electrostatic potential near the interface is changed, causing upward band bending close to the surface. This forms a potential barrier across the interface and is referred to as a Schottky barrier. Note that the Schottky barrier/contact is formed when the metal work function is higher than the semiconductor work function otherwise the formed junction is called an ohmic contact. The height of the Schottky barrier is given by,

$$\phi_{SB} = \phi_m - E_{x(sc)} \quad (2.1)$$

where ϕ_{SB} , ϕ_m , and $E_{x(sc)}$ are the semiconductor work function, the metal work function, and the electron affinity of the semiconductor, respectively. The direction and magnitude of band bending plays a crucial role in photocatalytic activity because it determines the direction of charge transfer/ transport across the interface/in the material. More detailed

2.3. Elementary Steps in Heterogeneous Photocatalytic Systems

analysis of the band bending and their implications on photochemistry has been recently summarized in reference[45].

2.3.3.2. Surface Active Sites

The second important parameter that should be taken into account when considering the surface reactivity is the number of surface active sites. These are operational sites at the surface where the reactants tend to adsorb and react with photogenerated charge carriers and eventually lead to new products. In this regard, the surface structure[46] and surface area of photocatalysts play important roles in determining active sites. The surface structure determines the adsorption ability, e.g. binding strength, of photocatalysts with the reactants. Molecules or atoms can either physically or chemically adsorb on the surface. In physisorption, the adsorbed molecules or atoms are in proximate contact with the surface via weak Van der Waals interaction. No chemical bond is formed between the physisorbed adsorbates and the surface, which results in no change in the electronic structure of the involved substances. In chemisorption, a strong chemical bond is formed in a monolayer on the surface upon transfer (ionic bonds) or sharing (covalent bonds) of electrons among the adsorbates and the surface. Chemisorption consequently modifies the density and position of electronic states of the surface-adsorbate complex. The binding energy of species involved in chemisorption (~ 1 to 10 eV) is higher than in physisorption (10 to 100 meV). Of course, there exist a whole spectrum of bond strengths going from weak physisorption bonds to strong chemisorption bonds. Chemisorption is the dominant adsorption mechanism in heterogeneous photocatalytic systems.

The chemical reaction that takes place at the surface active site is either reduction (gain of electrons) or oxidation (loss of electrons) or both (redox). In a photocatalytic process, both oxidation and reduction happens at the surface of the same material and no net charge is accumulated, whereas in photoelectrochemistry (PEC), oxidation takes place at the (photo) anode and reduction takes place at the counter-electrode (or photo-cathode). The VB holes are powerful oxidants ($+1.0$ to $+3.5$ V vs. normal hydrogen electrode (NHE) depending on the semiconductor and pH), while the CB electrons are good reductants ($+0.5$ to -1.5 V vs. NHE)[15, 47]. Most organic photodegradation reactions utilize the oxidizing power of the holes directly or indirectly. However, to prevent a buildup of charge one must also provide a reducible species to react with the electrons.

2. Fundamental Photocatalytic Process

2.4. Titanium dioxide Properties

This section highlights some basic properties of TiO₂, ranging from structure, electrical, optical, and surface. Some fundamental approaches for photocatalytic enhancement of TiO₂ are discussed in the end of the section.

2.4.1. Bulk Properties

TiO₂, also known as titanium (IV) oxide or titania, is a naturally occurring oxide of titanium [48]. It is one of the basic materials in our daily life and has been used for a variety of applications over long time. As discussed in the chapter 1, this material possesses several properties favorable to the photocatalytic applications. There are several extensive reviews available on TiO₂ photocatalyst systems, so the reader can refer to them for further and more detailed understanding of this material[8, 20, 37, 38, 40, 49].

Structural properties: TiO₂ crystallizes naturally in three forms: rutile, anatase, and brookite phase. The rutile phase is thermodynamically the most stable phase. The anatase phase, in contrast, is more stable at lower temperatures and converted into rutile at higher temperatures. The crystal structure of both anatase and rutile are similar, belonging to the tetragonal crystal family. On the other hand, the brookite phase has an orthorhombic crystal structure. This phase is less studied due to its inefficiency as a photocatalyst. Anatase and rutile have the same tetragonal symmetry, but they differ in physical properties. In rutile, the structure is based on octahedrons of titanium oxide that share

Table 2.1: Structural properties of titanium dioxide

Properties	Anatase	Rutile	Brookite
Crystal structure ^a	Tetragonal	Tetragonal	Orthorhombic
Lattice constant (Å) ^a	a=3.784 c=9.515	a=4.5936 c=2.9587	a=9.184 b=5.447 c=5.145
Space group ^a	I4 ₁ /amd	P4 ₂ /mnm	Pbca
Molecule/cell ^a	4	2	8
Density (g/cm ³) ^a	3.79	4.13	3.99
Refractive index ^{b,c}	2.52	2.71	2.583
Melting point ^b	Becomes rutile at high temperature	1858	Becomes rutile at high temperature
Ti-O bond length (Å) ^a	1.937(4) 1.965(2)	1.949(4) 1.980(2)	1.87~2.04

^aReference[50] and therein

^bReference [20]

^cReference[48]

2.4. Titanium dioxide Properties

two edges of the octahedron with other octahedrons and form chains. It is the chains themselves which are arranged into a four-fold symmetry [51]. In anatase, the octahedrons share four edges hence the four-fold axis. TiO_2 with rutile crystal structure is the most used phase in industrial applications[20]. The crystal structure properties of the three TiO_2 phases are summarized in **Table 2.1**.

Surface properties: The surface of course plays a crucial role in governing photocatalytic activity. It determines how the material will interact with the environment and is the key in forming interfaces with other materials. A detailed knowledge and better understanding of surface properties, thus, will help solve some fundamental issues, concerning the improvement of catalytic reactions[40]. The mixed nature of ionic and covalent bonding of this metal oxide surface structure has the capability of influencing local surface chemistry in a richer way as compared to metals or elemental semiconductors[46]. The single crystalline TiO_2 surface, especially rutile (110) surface, has been well studied for this purposes as a model system, since it offers excellent properties[40]. A detailed analysis of the surface structure of TiO_2 can be found elsewhere [40].

Electronic properties: The photocatalytic properties of TiO_2 are determined by its electronic structure. In TiO_2 , the VB is created by O_{2p} states whereas the CB is formed by Ti_{3d} states. The energy bandgap size is essentially established by hybridization of these 2 orbitals[50]. The electronic band structure of titania has a wide indirect bandgap of about ~ 3.2 eV for anatase and ~ 3.0 eV for rutile [52]. It is reported that the anatase phase has a higher photocatalytic activity over rutile due to the difference in position of energy band levels with reference to the water redox potential. It should be noted that the VBM for both types lies at the same energy level with respect to water redox potential. The origin of the higher photocatalytic activity in anatase arises from the fact that its CBM lies 0.2 eV above rutile CBM that gives more reducing power than rutile; for example, it can reduce molecular oxygen into superoxide radicals [20]. The oxidation potential of photogenerated holes is about +3 eV, whereas the reduction power of photogenerated electrons is about TiO_2 is about -0.3 eV[53].

The exact stoichiometry of TiO_2 is primarily determined by the process conditions such as oxygen partial pressure and temperature. Any deviation from perfect titania stoichiometry results in oxygen depletion (vacancy defects). The oxygen vacancy makes titania become an n-type material and is responsible for color centers in titania. Moreover, the depletion of oxygen creates Ti^{3+} sites in the lattice, which is the origin for electrical conductivity of titania[8]. The formation of oxygen vacancies can have 0,1,2 electrons associated with them and with different energies [54]. Tang et al [52] studied the electronic properties of rutile and anatase titania extensively and reported a change in electronic conductivities

2. Fundamental Photocatalytic Process

between them after thermal reduction in vacuum around 400 or 450° C. It has been observed experimentally that the effective mass of electrons is smaller in the anatase phase in comparison to the rutile phase, resulting in higher mobility [55].

Optical properties: TiO₂ optical properties stem from its electronic band structure. Since the anatase phase has a bandgap of 3.2 eV, it is highly transparent to visible light and absorbs below 380 nm wavelength. TiO₂ has high refractive index ($n_{\lambda@550\text{nm}} = 2.54$ for anatase and 2.75 for rutile) [56]. The origin of the high refractive index is the TiO₆ octahedral structure, the basic building block of rutile and anatase. Under optical excitation, titania exhibits a broad visible photoluminescence in the green color range (~2.1 to 2.3 eV). The origin of this luminescence is the recombination of self-trapped excitons (STEs)[57-59]. The concept of STE can be understood by considering the ionic nature of TiO₂. The ionic nature gives rise to a strong electron-lattice interaction, leading to formation of a polaron. A bound electron-hole pair involving such a type of polaron formation is described as STE, which may be immobilized by its own lattice distortion field[60].

2.4.2. TiO₂ Nanostructures

TiO₂ in the form of nanostructures[61, 62] has received much attention due to its improved performance in solar cells[22], heterogeneous photocatalysis[8, 37], and non-linear optics[63]. The improved performance is a direct consequence of shrinking particle size down to the nanoscale, which in turn results in different physiochemical properties as compared to its bulk form[64]. The commercially available Degussa P-25 (here 25 represents the mean diameter of the particles) has a mixed phase of anatase and rutile in a ratio of about 3:1 and has a surface area of about 49 m²/g [65]. It is reported to have enhanced photoactivity owing to its particle size and reduced recombination rate. The anatase phase is considered to be the active element in the mixed phase, whereas the rutile acts as an electron sink to reduce the recombination rate[66]. TiO₂ in the form of nanocrystalline porous structure is being predominantly used in dye-sensitized solar cell applications due to 1000-fold increase in effective surface area [67]. TiO₂ in the form of nanotubes, nanowires, etc., are also reported to have enhanced photocatalytic performance [68, 69]. Overall, TiO₂ as nanostructures offers high surface to volume ratio and short path for charge carriers to the surface (especially for photogenerated holes).

2.5. Approaches to Improve TiO₂ Photocatalytic Performance

It is clear from the description of the elementary steps of the photocatalytic processes that the fundamental governing parameters of a photocatalytic system are light absorption,

2.5. Approaches to Improve TiO₂ Photocatalytic Performance

charge carrier dynamics, and provision of surface active sites. So, a good photocatalyst is said to possess all these properties in a favorable way to improve the quantum efficiency. As can be seen from **Figure 2.6**, there exist several semiconductor photocatalysts, but none of them satisfy all the requirements for being a good photocatalyst. Nevertheless, TiO₂ still dominates being a potential candidate in this field though it absorbs only in the UV region, owing to its robust properties. Moreover, it can be used as a good model system through modifications of its surface chemistry since a wealth of available information exists in the literature. In this regard, there are three fundamental approaches proposed in the literature to enhance the performance of TiO₂ [70]:

- (i) Bandgap engineering and/or use of photosensitizers for broadening of the absorption wavelength range
- (ii) Optimization of the charge transport and minimizing charge carrier recombination
- (iii) Provision of adequate quality and quantity of active surface sites

These approaches have been widely followed and subject to research efforts by the scientific community because of their potentials to improve the photocatalytic performance.

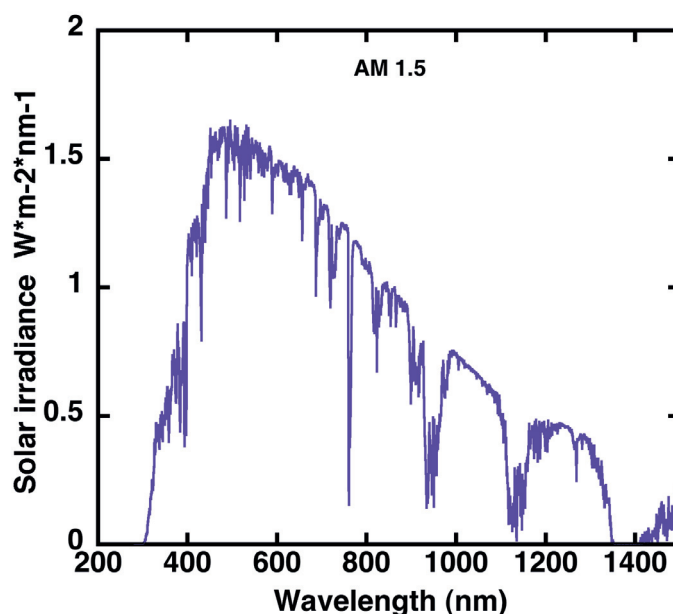


Figure 2.7: Global air mass 1.5 solar spectral distribution

2.5.1. Bandgap Engineering and Photosensitization

This approach is used to extend light absorption of TiO₂ photocatalyst systems into the visible region. **Figure 2.7** shows the incoming solar radiation that reaches the earth surface. According to this spectrum, the ultraviolet region and visible region constitutes

2. Fundamental Photocatalytic Process

of about 4% and 43%, respectively in the incoming solar radiation[71]. It is, therefore, important to extend light absorption in the visible region in order to improve the overall efficiency. There are two pathways commonly followed to accomplish this approach.

- (i) Bandgap engineering
- (ii) Photosensitization

Bandgap engineering is the process of altering the bandgap of a semiconductor through modifying its electronic properties. The proposed way to modify the bandgap is through an introduction of some additional energy states in the bandgap and/or shrinking the bandgap via impurity doping, making alloys of different compositions, etc. Non-metal doping such as carbon[72-75], nitrogen[76-78], boron[79], and sulphur[80] has also been attempted to improve the absorption of titania photocatalyst in the visible.

Photosensitization is the concept of incorporating either some molecules (dyes) or metallic NPs on the TiO₂ surface that have absorption or plasmonic spectrum in the visible region. The function of these sensitizers is to create e-h pairs through visible light absorption and inject the photogenerated electrons to the CB of TiO₂ due to favorable energy alignment. The injected electrons result in causing either photocurrent or reduction while the holes will be scavenged by an electron donor. In this way, light absorption in the visible region can be achieved. This is the backbone of dye-sensitized based solar cell systems[13]. Nobel metal NPs have the ability to extend light absorption of TiO₂ into the visible region through excitation of surface plasmon resonance[30, 31, 34]. The concept of surface plasmon resonance will be discussed in the chapter 4. Plasmonic NPs have some advantages over dyes because they are more robust and non-degradable.

2.5.2. Optimization of the Charge Transport

Operation of the catalytic system requires charge carrier transport to the surface. So, the focus of the second proposed approach is to improve charge carrier dynamics in TiO₂. There are several ways to improve charge carrier transport to the surface. The simplest one is to prepare photocatalyst with smaller thickness or make it on a nanoscale because they offer shorter path for the photogenerated charge carriers to reach the surface active sites. In this way, charge carrier recombination could considerably be reduced. It should be also noted that films with smaller thickness absorb less light compared to thicker films. This problem can be compensated by designing composite structures[81]. Addition of metal NPs on TiO₂ in the form of co-catalysts will improve charge carrier separation[82, 83]. Making rectifying heterojunction structures could also serve to improve charge separation[84].

2.5. Approaches to Improve TiO₂ Photocatalytic Performance

2.5.3. Optimization of the Surface Area

The third approach is used to improve surface active sites and reduce back reaction. Surface area plays one of the important roles in enhancing the activity of the photocatalyst by providing a platform for the reactants. As a rule of thumb, more surface area makes more reactants adsorb on the active sites of the surface. It will eventually lead to more products and thereby increasing the overall efficiency. For instance, the commercially available Degussa P-25 TiO₂ shows higher photoactivity due to its improved surface area (~49 m²/g) and mixed phase of anatase and rutile [65, 66]. Nanostructuring photocatalysts is the most effective way to improve not only the surface area but also all the elementary processes. Another way to improve surface area is to use porous supports or templates, whiskers or nanotubes.

2. Fundamental Photocatalytic Process

3. Experimental Methods

This chapter provides information about sample fabrication methods and characterization techniques used in the study. The description is organized in the same order as for a typical experiment: fabrication, characterization, and test of activity.

3.1. Deposition Methods

The materials used in this thesis were TiO₂, graphitic-carbon, graphene, silicon oxide (SiO₂), gold (Au), silver (Ag), and copper (Cu). These materials have been deposited by physical vapor deposition (PVD) and chemical vapor deposition (CVD) methods and appear in the form of nanometer thin films or nanometer particles.

3.2. Physical Vapor Deposition

PVD is a method of growing thin films onto a desired substrate. The deposition involves evaporation of the source material by heating and its condensation onto the substrate at controlled temperature. The chamber is maintained under vacuum in the range between 10⁻³ mbar to 10⁻⁹ mbar, depending on the process requirements. The source material can be evaporated by different ways such as plasma sputter, pulsed laser ablation, evaporation, etc.

3.2.1. Electron Beam Evaporation

The electron beam evaporation (e-beam) makes use of a high-energy electron beam to heat and evaporate the source material. The electron beam originates from an electron gun consisting of a tungsten filament and electron optics. When a high DC voltage (10 to 30 KV) is applied to the filament, the thermally excited electrons that have energies above the vacuum level electrons are pulled from the tungsten filament and accelerated and focused on the target. The energetic electrons transfer their kinetic energy to heat in the collision with the source material, which is then heated. The source atoms are vaporized and travel straightly in vacuum and eventually condense on the substrate. The transferred energy is quite high, making high temperatures possible, to achieve high deposition rates. The e-beam evaporated films usually have less contamination in comparison to thermally evaporated films because only the source material is heated.

Carbon films (see paper I, II, and III) were deposited in the AVAC HVC 600 e-beam evaporator with poly-crystalline graphite as the source material. The deposition chamber was maintained at around 10⁻⁶ mbar and the substrates were at RT. The deposition rate was maintained at 1Å/s in order to achieve the nominal thickness of about 20 nm at stable

3. Experimental Methods

operational conditions. The NPs in paper IV were prepared by depositing a thin layer of Au and Ag films in the same evaporation chamber. The nominal thicknesses of the Au and Ag films were 3 nm and 5 nm, respectively. The deposition rate was maintained at 1Å/s.

3.2.2. Sputtering

Sputtering is a physical process by which the source material is bombarded with high energetic plasma (ionized gas) to dislodge the source atoms. The plasma is usually created in an inert gas, such as argon, by applying a RF voltage. The applied EM field ionizes the argon atoms and creates positive argon ions and free electrons. The energetic free electrons create more ions on the way they collide with other gas molecules. On the other hand, the high energetic positive ions are attracted towards the negative electrode, where the source material is placed. During the collision, the positive ions transfer its energy and momentum to the source. This process ejects some atoms or clusters from the source. The ejected atoms travel in the chamber until they encounter the target where they get deposited. Sputtering process is normally associated with a glow discharge (plasma) due to radiative relaxation of the free electrons and excited atoms/ions.

In this thesis, direct current (DC) reactive magnetron sputtering was used to deposit TiO₂ thin films. In this sputtering, the deposited TiO₂ was formed by chemical reaction between the source material (titanium) and the reactive gas oxygen introduced in the chamber during the sputtering. The argon was used to initiate the sputtering process with a flow rate of 40 SCCM whereas the oxygen flow rate was maintained at 12 SCCM initially and then reduced to 4 SCCM during the deposition. The DC power was kept at 1 kW. The chamber pressure was kept at 5×10^{-3} mbar during the sputtering.

3.3. Chemical Vapor Deposition

CVD is a method for depositing a material in solid (film) form onto a substrate through chemical reaction of gas phase precursors. To achieve this, the precursor gases are mixed with carrier gas and fed to the chamber at ambient conditions. The substrate is kept at high temperature. When the precursor gases come in contact with the substrate, they react chemically and form a solid phase of desired materials onto the substrate. The parameter that influences the chemical reaction is the substrate temperature, concentration (pressure) of precursors, and carrier gas. This technique was, in the present work, used to deposit graphene and SiO₂. The graphene synthesis was done using Black Magic, AIXTRON Nanoinstruments Ltd using methane or acetylene as a precursor material. The chamber was heated to 1000°C to initiate the reaction for graphene deposition with and without catalysts. Details of the graphene synthesis by the CVD technique can be found

in references[85-87]. The SiO₂ insulating layer in paper II and IV was deposited by plasma enhanced CVD (STS) using silane and oxygen as precursor materials. The temperature of the substrate was kept at 300°C.

3.4. Nanofabrication Techniques

Nanofabrication is a process of manipulating materials to make structures at nanoscale. Presently nanostructures are fabricated by *top-down* and *bottom-up* approaches. In the *top-down* approach, a bulk material is, for example, etched gradually until the desired shape and structure is achieved (removal of substance). Typical examples for *top-down* method are conventional photolithography, e-beam lithography, focused ion beam etching, etc. In contrast, the *bottom-up* approach starts with steering atoms or molecules to form nanostructures (addition of substance), for example, by self-assembly techniques.

3.4.1. Hole-mask Colloidal Lithography

Colloidal lithography is a class of non-conventional and bottom-up nanofabrication techniques for preparing 2-D arrays of nanostructures on a large-scale sample area at relatively low-cost. In this technique, charged polystyrene (PS) beads are used as a template to define the desired nanostructure.

Hole-mask colloidal lithography (HCL) is a slightly modified version of the original colloidal lithography technique for deposition of nanostructures[88]. It relies on using colloidal PS nanospheres as an etch mask to pattern and deposit a variety of materials. This method offers fabricating structures with different sizes and shapes on a large area, but it yields only short-range order. The lack of long-range order is an advantage for certain types of optical experiments because it prevents interference and diffraction effects. The technique is simple, cost-effective, and faster comparing to conventional, serial top-down lithography methods like e-beam lithography.

The fabrication procedure starts with spin coating the substrate with a thin PMMA sacrificial polymer layer and subsequent baking of the polymer at 180 °C for 5 to 10 minutes. The polymer layer is further subjected to oxygen plasma etching for 5 seconds to improve its hydrophilicity. Dip coating of the sample in positively charged water-based PDDA electrolyte follows next. Negatively charged PS beads are then deposited in liquid phase onto the PDDA layer (**Figure 3.1a**). The PS beads are bound firmly and distributed homogenously on the substrate due to electrostatic attraction between PS beads and the PDDA and repulsion between the beads. A thin metal film (Au) resistant to oxygen plasma is evaporated onto the sample (**3.1b**).

3. Experimental Methods

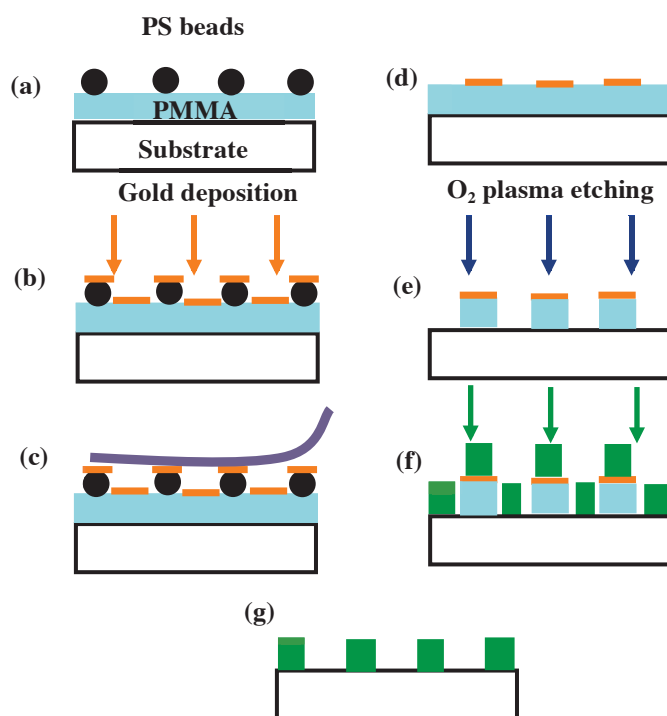


Figure 3.1: Illustration of the different steps in the HCL nanofabrication method (a) Deposition of PS beads on a PMMA layer (b-d) Etch mask deposition (Au), removal of PS beads by tape stripping, and formation of patterned nanoholes (e-f) Removal of PMMA beneath holes and deposition of target materials (g) Final nanostructure after lift-off in acetone.

In the next step, the beads are removed by tape stripping or in ultrasonic bath with isopropyl alcohol (**3.1c**). Removal of the beads also removes the Au that was deposited on top of the beads, and leaves nanoholes in the PMMA sacrificial film (**3.1d**). Here, the PS beads define the size and diameter of the holes. Reactive oxygen plasma etching is then used to remove the PMMA underneath the nanoholes (**3.1e**). The hole-mask prepared in this method, consisting of a bottom layer of PMMA and a top layer of Au, mimics a conventional photolithography mask and can be used as an etch mask to etch the underlying substrate and/or as a deposition mask (**3.1f**). The etch mask is finally lifted-off in acetone (**3.1g**). Using the HCL technique, different types of nanostructure based on metals (Au, Ag & Cu) and carbon were fabricated during the thesis work.

3.5. Annealing Treatments

All deposition methods described in this work were carried out at room temperature (RT). As-deposited structures are highly amorphous or very finely microcrystalline according to the characterization tests. Post-deposition thermal treatment was carried out to make fabricated structures crystalline. It was performed by rapid thermal processing (RTP) process. The RTP process employs high intensity halogen lamps to generate the

3.6. Analytical and Characterization Techniques

necessary heat. Since the method employs a lamp as a heating source, the desired temperature can be achieved within a few seconds (thus the name rapid). The system also allows the possibility to use different process gases during the treatment. The system used in this thesis to anneal the fabricated samples was Jiplec Jetfirst 200. Summary of all preparation recipes can be found in **Table 3.1**.

Table 3.1: Summary of annealing parameters employed in the RTP system for different fabricated materials

Materials	Temperature (°C)	Annealing time (minutes)	Process gas
Carbon	800	10 to 30	Argon
TiO ₂	500	10 to 20	Argon
Au	300	15 to 30	Argon
Ag	200	15 to 30	Argon
Graphene oxide (GO)	150 to 200	15 to 30	Nitrogen

3.6. Analytical and characterization Techniques

A number of analytical and characterization techniques were used to probe the material properties of prepared samples either *ex situ* or *in situ*. They provide knowledge on material's internal structure such as composition, phase, and distribution of elements within the material, topography of surfaces, etc. This section briefly describes the used toolbox.

3.6.1. Scanning Electron Microscope

The birth of electron microscope (EM) began in 1931 with the optical microscope approaching its theoretical resolution limit (180 nm) due to light diffraction. The EM provides high-resolution image because of the small wavelength (de Broglie) of electrons. A typical scanning electron microscope (SEM) with different components is schematically illustrated in **Figure 3.2 (a)**. It consists mainly of an electron gun, different electromagnetic lenses, an aperture, scanning coils, and different electron detectors. The main working principle of an SEM is as follows. The electron gun emits a beam of electrons by applying a voltage to a thermionic tungsten filament. These electrons are attracted by the anode and accelerated vertically through the column of the SEM. On its way, the beam passes through different magnetic lenses before reaching the sample surface. A pair of condenser lenses demagnifies the electron beam and defines the beam size, which in turn determines the resolution of the SEM. The objective aperture blocks any unwanted spray electrons. The objective lens focuses the beam on the sample surface. The sample is scanned in a raster across the specimen with the help of scan coils.

3. Experimental Methods

When the incident electrons (primary) beam with high energy impinges on the sample, a number of different signals are generated as described below (see **Figure 3.2(b)**).

Secondary electrons: The energetic primary electrons knock out electrons from the surface of the sample. The energy of these electrons is relatively low (0-30 eV). Together with inelastically scattered primary electrons, they are used to analyze the surface topography.

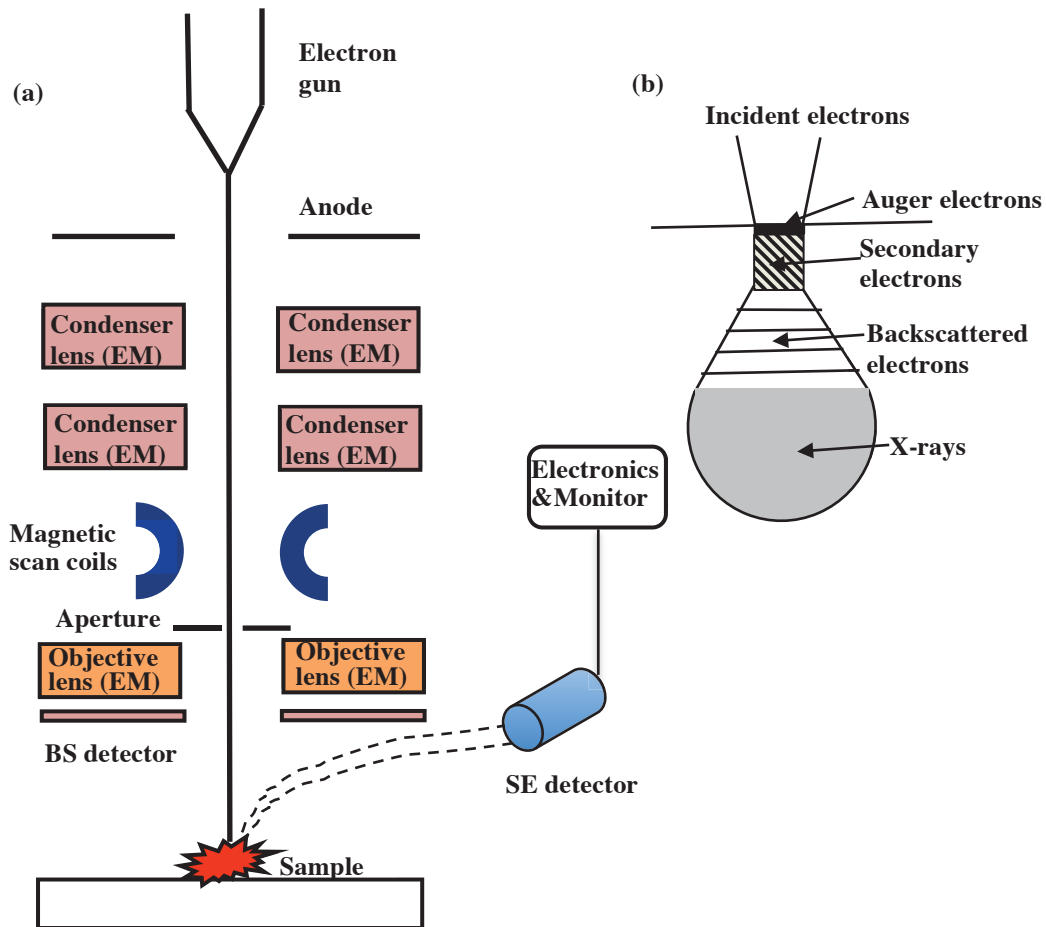


Figure 3.2: (a) Schematic representation of a typical SEM (b) Sample interaction volume and the generation of different signals. The size of the interaction volume depends on the incident electrons' energy, composition, and the density of the sample.

Backscattered electrons: These are highly energetic (within a few eV the same as the primary electrons' energy) elastically scattered electrons. They are originating from the sample down to 0.5 μm below the surface. The elastically scattered electrons are used to analyze the bulk properties and compositional aspects of the specimen.

3.6. Analytical and Characterization Techniques

Auger electrons, X-rays, and cathodoluminescence can also originate from the specimen. The relative strengths of the different signals from the specimen depend strongly on the incident energy and composition of the material. SEM in combination with x-ray spectroscopy can be used as an analytical technique for elemental analysis.

Important advantages of SEM over optical microscopy are its relatively large depth of analysis, the capability of producing an image that is a good representation of the sample, etc. One limitation, however, is that the sample has to be conductive enough to avoid charge accumulation. This problem is circumvented in the so-called environmental SEM. The combination of larger depth of field, greater resolution (~ 2 nm), higher magnification, compositional and crystallographic information makes the SEM one of the most extensively used instruments for different applications both in industries and the academy. In this thesis, the JEOL SEM (JSM-6301F) and the Zeiss Supra (60 VP) SEM were used to analyze morphology of thin films, nanoparticles shape, diameter, and their distributions.

3.6.2. Atomic Force Microscopy

The atomic force microscope (AFM) is a versatile instrument belonging to a family of scanning probe microscopes (SPMs). It is used to probe the surface topography of a sample with atomic resolution. Commonly, SPM relies on an interaction between a sharp tip and the sample surface. It raster-scans the surface and monitors the tip to the sample interactions. Different types of interactions between the tip and the sample surface bring different names to SPM.

In AFM, the sample surface is probed with a sharp tip of less than 10 nm. The tip is attached to the free end of a cantilever (100 to 200 μm long) [89]. When the tip is brought closer to the surface, forces between the tip and the sample surface cause the cantilever to bend or deflect. The cantilever deflection is recorded during the scanning by a detector. The signal is then sent to a computer and electronics to generate the surface map of the sample. In modern AFMs, the cantilever deflection is monitored by an optical lever technique in which a laser beam is directed to the backside of the cantilever. The position of the reflected beam is measured using a four-quadrant photodiode detector. AFM allows one to operate it in different modes to analyze the surface properties of the specimen. The most commonly used modes in AFM are contact, non-contact, and tapping modes. The corresponding force-distance curves[90] of these modes are plotted in **Figure 3.3 (b)**.

3. Experimental Methods

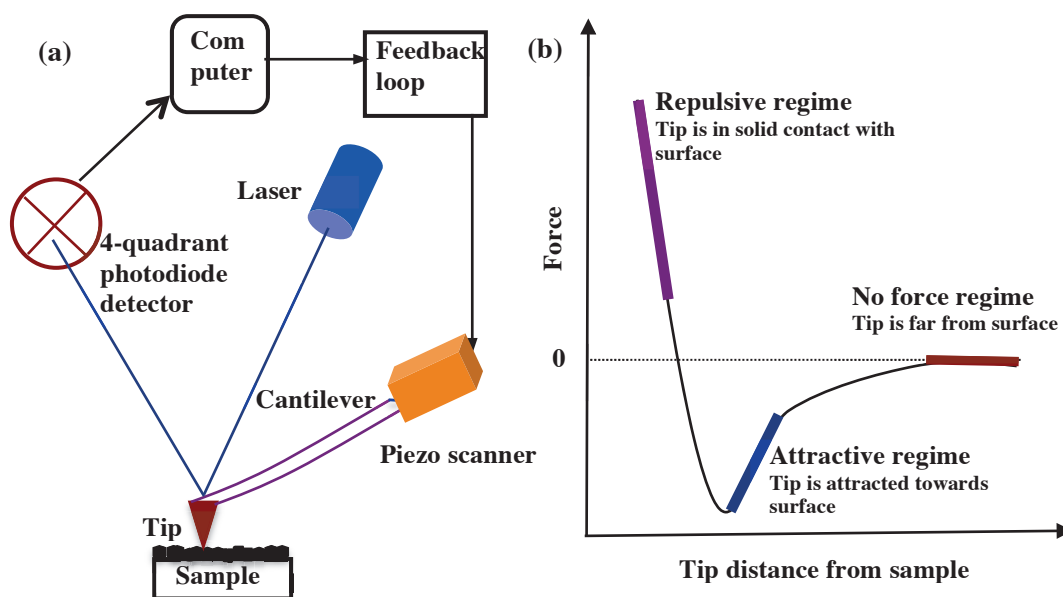


Figure 3.3: (a) A typical AFM setup. It consists of a tip attached to a cantilever, scanner, and a four-point photodiode detector (b) Plot of force-distance curve indicates the position of the tip from a sample surface and its corresponding force regime. Different mode of AFM operation is based on one or combination of this regime.

One of the great advantages of AFM is that it can be used to study both conducting and non-conducting surface. It does not require vacuum and any special sample preparations except that the sample needs to be reasonably flat on a macroscopic scale. The Veeco Dimensions 300 SPM and the Bruker Dimension 3100 SPM were used in the thesis to characterize carbon and TiO_2 structures and also to measure the height of NPs. The AFM was operated in tapping mode and a silicon tip of diameter below 5 nm was used.

3.6.3. UV-VIS-NIR Spectrophotometer

As the name implies, this spectrophotometer measures the interaction of light with solids or liquids in the UV-VIS-NIR regions. These regions are more interesting and important because different optical transitions in solids occur over these spectral intervals. **Figure 3.4** shows a double-beam spectrometer setup with its different parts. It consists of a light source, diffraction gratings (monochromator), a sample holder, chopper, and a detector. The light that is coming out of the source enters the monochromator and gets spectrally diffracted into different wavelength. The light output from the monochromator is split into 2 beams by a chopper, where one light beam probes the sample and the other light beam is used as a reference. The chopper allows one beam at a time to the detector while blocking the other one since it consists of a transparent, a mirror and a dark segments. The double beam mode is normally found in modern spectrometers. The reference beam

3.6. Analytical and Characterization Techniques

intensity is set to 100 % transmission and the detector measures the intensity ratio of the sample and the reference. The advantage of double beam over single beam is that any fluctuations in the light source, detector or electronics are removed each time a measurement is taken [91].

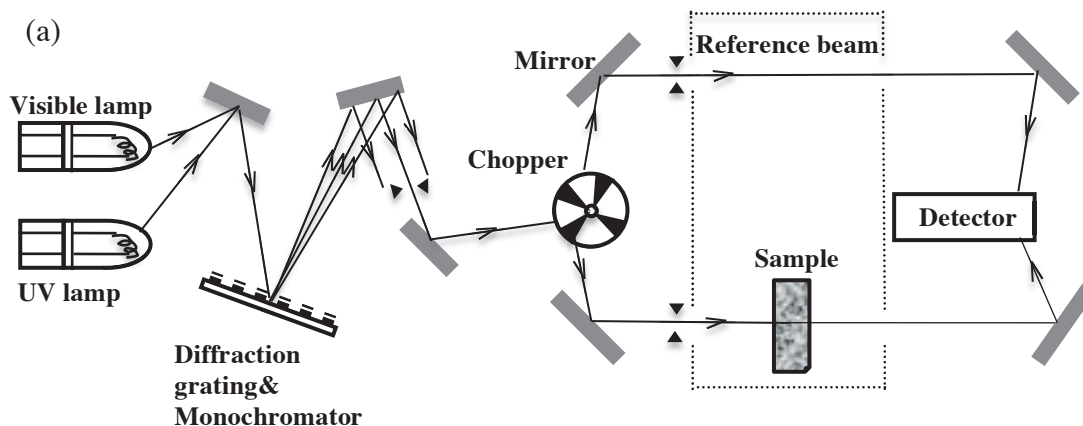


Figure 3.4 (a): Schematic of a double-beam spectrophotometer setup. In this setup, the light beam is split into 2 beams by a chopper. One beam is used as a reference and other beam is used to probe the sample.

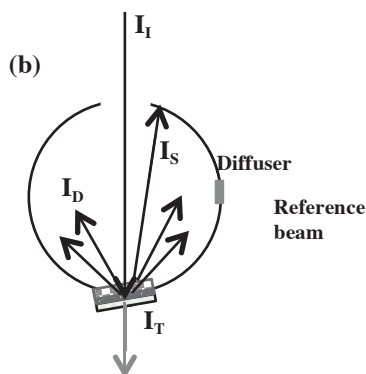


Figure 3.4(b): Schematic of a typical integrating sphere. The sample is mounted 3° tilt from the normal incident in order to avoid the light scattering back from the front port. I_s and I_D represent the specular and diffuse reflectance light intensity, respectively.

The instrument measures the intensity of light as a function of wavelength. It actually measures the transmitted light, i.e. the ratio between light that is coming out of the sample and the incident light (I_0).

$$\text{Transmission} = I / I_0 \quad (3.1)$$

The extinction, which usually describe the light absorbed and scattered by the sample, can be determined from the obtained transmission spectrum by,

$$\text{Extinction} = \text{Absorption} + \text{Scattering} = 1 - I / I_0 \quad (3.2)$$

3. Experimental Methods

The scattering can be measured separately by the diffuse reflectance accessory (DRA). The DRA setup contains an integrating sphere and a detector located either on the top or bottom of the sphere (**Figure 3.4(b)**). The integrating sphere is a hollow spherical cavity whose wall is coated with a high reflecting material, which in principle reflects all light several times until the light reaches the detector. The optical absorption can be finally calculated from the equation 3.2. The Cary Varian 500 and 5000 double-beam spectrophotometers were used in the thesis for performing optical characterizations on the prepared samples.

3.6.4. Photoluminescence Spectroscopy

Photoluminescence (PL) spectroscopy measures the intensity of luminescence as a function of wavelength, temperature, excitation intensity, and time. It is a unique, highly sensitive, and non-destructive method to probe the electronic energy levels and defects in a given material using the PL intensity, peak position, and line width at ambient conditions. Analysis of these parameters helps understanding the underlying physics of the recombination mechanism in semiconductors. Recombination of photogenerated charge carriers can dissipate energy both radiatively and non-radiatively. PL spectroscopy measures only the radiative recombination of charge carriers. A typical PL setup is shown in **Figure 3.5**. The setup consists of a laser source, optics, and a detector. The excitation laser source photons excite electrons from the VB to the CB and leave holes in the VB. Since an excited state is not stable for the electron, it falls back to the ground state by emitting a photon corresponding to the bandgap energy and/or other energies below the bandgap if the electron is trapped in defects and impurities. The emitted light is collected by a microscope objective and sent to the detector. Non-radiative recombination (emission of phonons) is one of the competing processes because the thermal energy (lattice vibration) can dissociate the exciton from trapped or impurity sites. The analysis of such defect or trap states can be obtained from temperature-dependent PL measurements (4 K to RT). From these measurements, the activation energy of thermal quenching can be extracted. By varying the excitation energy, one could measure the concentration of the excited electronic states. In the time-resolved photoluminescence (TRPL) measurement, a laser pulse is used to excite the material and the decay of PL intensity transient yields the lifetime of charge carriers.

The setup employed for PL measurements as follows: We used a 325 nm wavelength He-Cd laser (cw) as an excitation source. The laser light was illuminated on part of the sample that was freely hanging in the air from the sample holder to avoid any contributions from the holder. The laser was shot at a certain angle on the sample in order to prevent scattered light reaching the detector. An optical fiber detector was used to collect the luminescence from the front side of the sample through a microscope

3.6. Analytical and Characterization Techniques

objective. For the low-temperature measurements, samples were placed inside a cryogenic chamber and the measurement was done in the temperature interval from 10 K to RT. The laser beam intensity used for both RT and low-temp measurements was ~6 mW. TRPL was investigated at 10 K by employing 372 nm wavelength laser (Pico Quant, 50ps-pulsed, 2 mW @ 40 MHz) as an excitation source. The selected spectral region was filtered out from the total PL signal using imaging spectrograph (HORIBA Jobin Yvon, iHR320) and registered by photon counting system (Becker&Hickl, PMC100, TCSPC, MCP) with overall time resolution of ~50 ps.

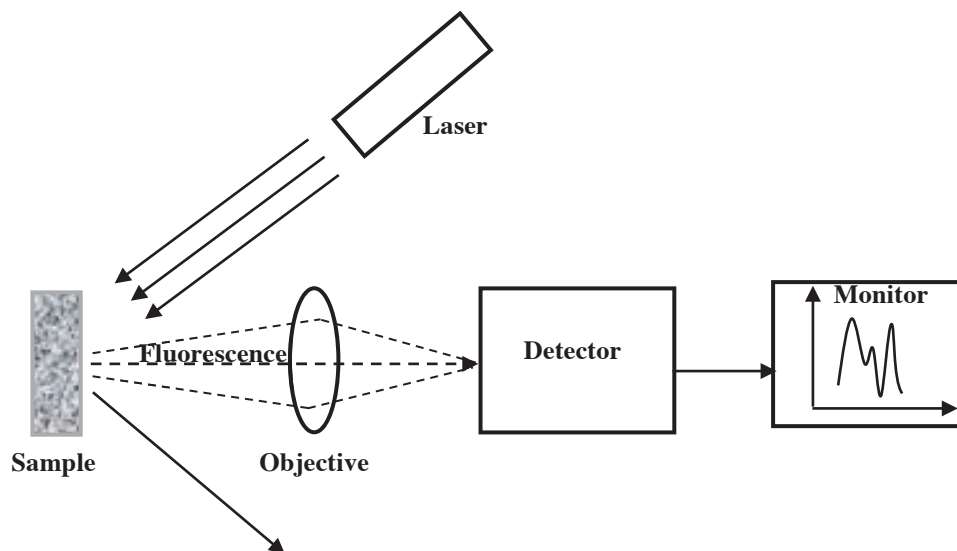


Figure 3.5: Schematic of a typical PL setup. The laser light is shot on the sample surface at a certain angle in order to avoid the incident light reaching the detector. The emitted light is collected by a microscope objective from the front side of the sample.

3.6.5. LSPR Spectroscopy

LSPR spectroscopy is a versatile optical characterization technique for *in situ* monitoring of local changes in the (metallic) NPs environment or in the particles themselves. As will be explained in the chapter 4, the LSPR frequency depends on the size, shape, material, and the local dielectric environment medium. The plasmon frequency will shift by manipulating any of these parameters. The shift can also be caused by changes in electronic density in the NPs provided that other mentioned parameters remain constant, as given in the expression 3.3,

$$\omega_{\text{plasmon}} = (Ne^2/m^* \epsilon_0)^{1/2} \quad (3.3)$$

where N , e , m^* , and ϵ_0 are the concentration of electrons, charge of an electron, the effective mass of electrons in the conduction band, and the vacuum permittivity,

3. Experimental Methods

respectively. According to the expression 3.3, the plasmon frequency is directly proportional to the square root of the density of electrons (i.e. the number of free electrons in the volume of metal NPs). In other words, the plasmon frequency shifts to the blue side if the electron density increases or to the red side if the electron density decreases. Based on changes in plasmonic peak position, one can deduce the charge transfer from TiO_2 to plasmonic particles (and vice versa) as well as chemical stability of particles (oxidation and corrosion) in real time. The spectroscopy setup used in the work consisted of a fiber optics spectrometer, a visible source, an UV source, and a quartz cuvette containing an aqueous solution (either milli-Q or methanol). The solution was bubbled with nitrogen gas to maintain inert conditions around the NPs. The sample was

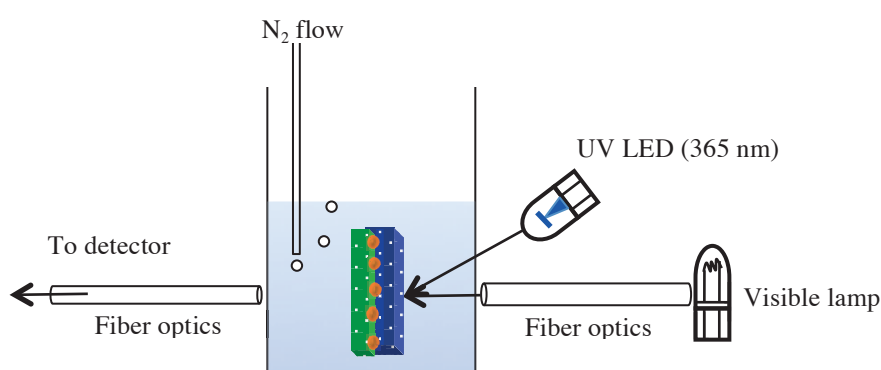


Figure 3.6: A simple LSPR spectroscopy setup. Visible light is irradiated normal to the surface while the UV light is irradiated at a certain angle. The transmitted light is sent through the fiber optics spectrometer to the detector for analysis.

placed in the solution and irradiated with visible light normal to the surface to excite the plasmons. In order to study charge transfer from TiO_2 to metal particles (Paper IV), an UV LED ($\lambda=365$ to 367 nm) was used to excite the TiO_2 at a certain angle, as shown in **Figure 3.6**. The transmitted light was collected by an optical fiber and the detector signal was sent to a computer for processing. In paper V, we used this technique to monitor changes in the copper NPs (supported on TiO_2) chemical stability (oxidation/reduction) in water under the bandgap illumination.

3.6.6. Raman Spectroscopy

Raman Spectroscopy is an analytical technique relying upon inelastic scattering of monochromatic light (typically a laser) with molecules as a result of molecular excitation such as vibration, rotation, etc. The working principle of Raman Spectroscopy is based on the Raman effect as illustrated in **Figure 3.7**. When the laser light strikes the molecule, it distorts the electronic cloud and causes polarization. The molecule distortion induces a

3.6. Analytical and Characterization Techniques

dipole moment $P=\alpha E$, where α is the molecular polarizability which determines the distortion of the electronic cloud. Since light contains a time-varying periodic electric field (E), the molecule starts to oscillate periodically with a characteristic frequency. It is known that when charged particles vibrate, they emit electromagnetic field. The emitted scattering light from the molecule can have three different characteristic frequencies.

Rayleigh scattering: A molecule in its lowest ground vibrational state (V_0) is excited to some virtual states after absorbing a photon of frequency (f_0). Eventually the excited molecule relaxes back to its original ground state (V_0) by emitting a photon. In Rayleigh scattering, the emitted frequency (f_0) is the same as the incident frequency. This is referred to elastic scattering, as there is no shift in frequency. The Rayleigh scattering is not Raman-active mode.

Stokes shift: A molecule (Raman-active) is excited to a virtual state from its lowest ground vibrational state with the help of a photon (f_0). When it relaxes back, it lands in one of the higher ground vibrational states. The difference between incident and emitted photon frequency (f_0-f_s) is referred to as Stokes shift. The emitted photon energy (f_s) is red shifted.

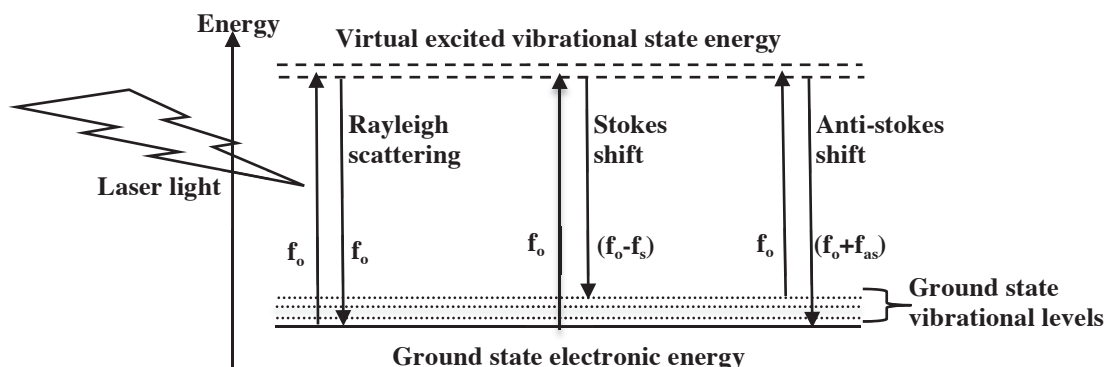


Figure 3.7: Energy level representation of the Raman effect with different active modes.

Anti-Stokes shift: At the time the Raman-active molecule is already in one of the higher ground vibrational states during excitation. It then relaxes back to the lowest ground vibrational state by emitting a photon (f_{as}). The resulting difference between incident and emitted photon energy (f_0+f_{as}) is referred to as anti-Stokes shift. In this case, the emitted photon is blue shifted.

The inelastic Raman scattering is relatively very weak as compared to Rayleigh elastic scattering. Care must be taken to separate Rayleigh scattering and fluorescence emission from the Raman scattered light reaching the detectors. There are some advanced Raman

3. Experimental Methods

spectroscopes such as Surface enhanced (SERS), resonance Raman, tip-enhanced Raman, etc., which gives enhanced Raman scattered signal. Raman spectroscopy encompasses wide applications in chemistry, solid-state physics, and biology.

In this thesis, Raman measurements were carried out by a LabRam spectrometer using a He-Ne laser of 632.8 nm light with a beam intensity of 1.76 mW. The use of Raman in our work was mainly to characterize the crystalline phase of the carbon and TiO₂ films.

3.6.7. X-Ray Diffraction and X-ray Photoelectron Spectroscopy

X-ray diffraction (XRD) is a technique to analyze the crystalline structure and composition of a material. XRD is based on the interaction of a monochromatic x-ray beam with a crystal lattice. Since the crystal lattice represents a periodic arrangement of atoms in 3-dimensions, it can act as a grating element to diffract/scatter the x-rays. The scattered waves from the atomic lattice can interfere constructively under special conditions and give rise to sharp interference maxima with the same symmetry as in the distribution of atoms in a given material. The criteria for constructive interference to occur according to Bragg's law is given by,

$$2d \sin\theta = n\lambda \quad (3.4)$$

where d , θ , n , and λ are the distance between the lattice planes, diffracted angle, diffraction order, and the wavelength of the x-ray, respectively. In this thesis, XRD was used to characterize the crystalline phase of as-deposited and annealed TiO₂ films using a Siemens D5000 diffractometer with a step size of 0.03 degree and time/step of 2 seconds.

X-ray photoelectron spectroscopy (XPS) is a technique to analyze the chemical state and elemental composition of a material primarily in the surface region. In XPS, an x-ray beam irradiates the material and emits the core-level electrons. The binding energy of the electrons can be determined by detecting the kinetic energy of the emitted electrons from the material. Though x-rays can penetrate down to 1 mm in the material, the mean free path of the electrons is on the order of 10 nm. So, XPS is a surface sensitive technique and the sampling depth is less than 10 nm from the surface. The electronic structure of the elements is very unique, so it is also elemental sensitive. Based on the shift in binding energy, the chemical state of the material can be determined. In this thesis, we used XPS to analyze the chemical state of the Cu NPs and graphene oxide using PHI 5500 XPS system at a base pressure of 10⁻¹⁰ mbar.

3.6.8. Gas Phase Chemical Reactor

Gas phase chemical reactor is a small (micro) reactor chamber where chemical reaction is normally taking place on a (photo) catalyst material. It is generally high sensitive to evaluate and optimize the performance of a thermo or photocatalytic activity. The microreactor can be used for liquid phase reactions as well. Simply speaking, the reactants in gas or liquid phase are fed to the reactor, by small channels, to take part in chemical reactions on the (photo) catalyst and then products are withdrawn through another end of the reactor for further analysis by mass spectrometry (MS) or gas chromatography (GC). The reactors can be operated both in batch and continuous or flow mode. In batch mode, the reactants are filled once in the reactor. After a while, the reactor is closed and brought to the desired temperature and pressure. These conditions are maintained for the time needed to achieve the desired conversion. In continuous or flow mode, there is continuous flow of the reactants to the reactor and continuous withdrawal of the products from the reactor[92]. Microreactors are fabricated from a variety of substrates such as silicon chip, quartz, metals, polymers, ceramics, and glass depending on the available fabrication techniques and the application. The advantages of a microreactor over conventional reactors are the following [93]; It provides high mass and heat transfer. It is safer and environmentally friendly as small amounts of chemicals being used. The residence time of the reactants flow is small because of small dimensions, which results in high space velocity [94]. It offers possibility to regulate parameters like pressure, flow rate, and also the residence time.

3.6.9. Mass Spectrometry

Mass spectrometry (MS) is a versatile method to quantitatively analyze the molecular or atomic mass of individual compounds. Simply saying, it is an analytical technique for weighing molecules based on the mass-to-charge ratio (m/z) of ions. The basic schematic of a mass spectrometer is shown in **Figure 3.8**. It involves three basic steps to map the spectra of masses[95].

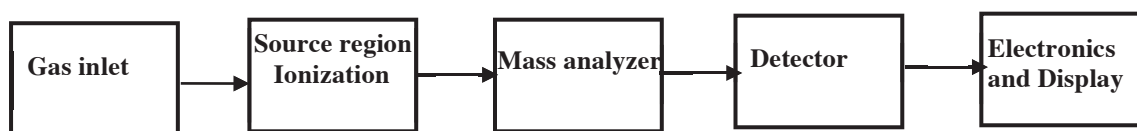


Figure 3.8: A block diagram of a common mass spectrophotometry instrument. The source region, mass analyzer, and the detector are maintained in ultra-high vacuum (UHV).

The first step is the conversion of analyte molecules or atoms into gas-phase ionic species. This is normally done in the source region (ionization source) where neutral

3. Experimental Methods

molecules are converted into ionic species (charged) by adding or removing an electron to or from the molecule. During the ionization process, the excess energy transferred may break the molecules into characteristic fragments. The charged ionic species are now accelerated into a mass analyzer with the help of the applied electric field. The mass analyzer is the central part of the mass spectrometer, where charged ions or their fragments are separated according to their m/z ratio. The quadrupole mass analyzer (QMA) is the most used analyzer in the mass spectrometer. The QMA consists of four circular metal rods arranged parallel to each other. A fixed DC and alternating RF potential is applied across the rods. The ions that are produced in the source enter the middle of the rods where their motions are controlled by the electric field. This allows the mass analyzer to filter only ions of a particular m/z . In other words, ions of particular m/z value that have a stable trajectory will reach the detector. Different ions can be filtered and sent to the detector by changing the RF value applied to the rods. The diameter and length of the rods determine the resolution and mass range [96]. Finally, the detector measures the ion current from the mass-separated species. The detected signal is amplified and displayed on the computer in the form of a mass spectrum.

3.7. Experimental Setup for the Photocatalytic Tests

The photocatalytic experiment setup consists of the following main parts:

- (i) Photoreactors
- (ii) Optics

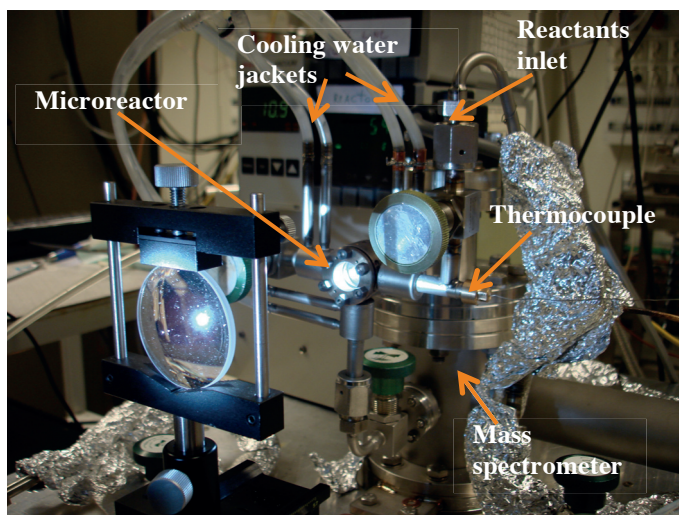


Figure 3.9: A photograph of the microreactor setup used in this work. Picture shows different parts in the setup. The microreactor is connected to a quadrupole mass spectrometer. Light is focused on the center of the sample using lenses and aperture.

3.7. Experimental Setup for the Photocatalytic Tests

Photoreactors: We used two different photoreactors to test the activity of the prepared samples. The first reactor used in the work was the third generation photoreactor which was designed and built in our lab. The reactor chamber is made of a tiny stainless steel cylinder of ~ 880 μl volume. It is closed on both sides by fused silica windows and sealed with O-rings. The reactor is connected online to a quadrupole mass spectrophotometer (QMS-VG), via a small capillary tube, for monitoring the reaction products. The reactor temperature is controlled by an external heater and water-cooling system and monitored by a thermocouple placed in the reactor in contact with the sample. The photoreactor setup mostly used during the thesis is shown in **Figure 3.9**.

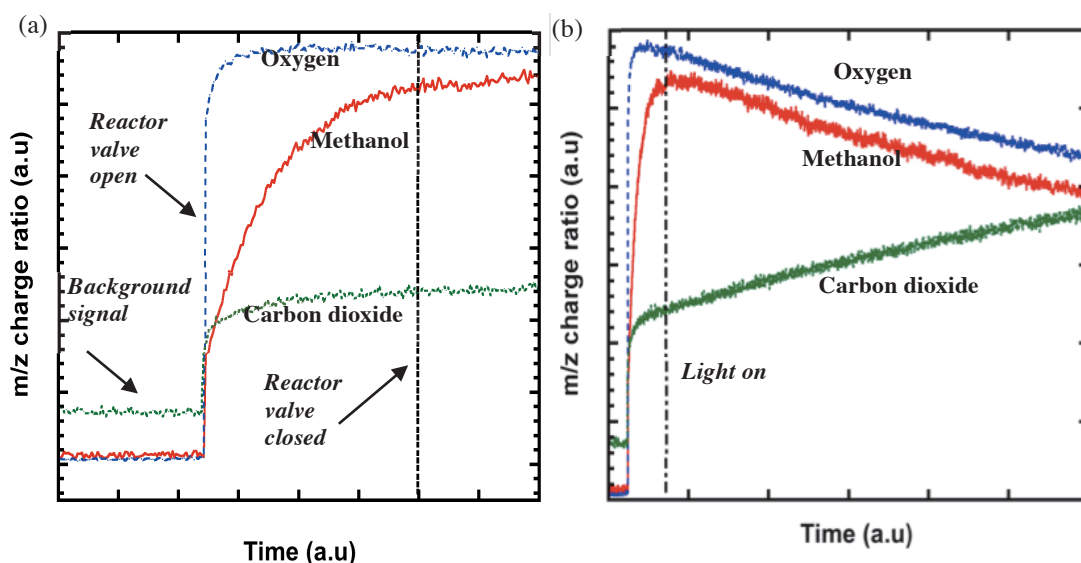


Figure 3.10: Illustration of the microreactor detection system. The QMS traces different subsequent processes in batch mode. Here the reactants are methanol and oxygen and the product is carbon dioxide. (a) The QMS signal of background gases and the reactants in the reactor before the light is turned on. (b) Showing *in situ* photocatalytic reaction under illumination. Note the decrease of the reactants and the corresponding increase of the product (CO_2).

The experiments described here were carried out in batch mode. The pressure inside the reactor was kept close to the atmospheric pressure, but it can be varied from about 10^{-3} mbar to slightly above the atmospheric pressure. The QMS itself is placed in an UHV chamber and operated at 10^{-7} to 10^{-10} mbar. Due to difference in pressures between the QMS chamber and the reactor, the gases inside the reactor leak into the QMS chamber. The reaction products are followed directly with only 3-5 seconds delay. Typical different subsequent processes in batch mode followed by QMS signals are illustrated in **Figure 3.10**. The example shows the signal from an empty reactor. As can be seen in the figure, there are some background gases always present in the reactor but they are in a negligible amount. The next step is to let the reactants mixture (methanol and oxygen) into the reactor from a small container. The corresponding m/z ratio of the reactants

3. Experimental Methods

mixture is followed on the monitor. The reactor valve is closed after the reactants pressure has reached equilibrium with the container. The reactants are now enclosed in a small volume of the reactor. The QMS shows distinctly each detection step (**Figure 3.10 (a)**). After a while, the sample mounted inside the reactor is irradiated by a mercury lamp. The light initiates a chemical reaction on the surface of the sample. In our case, photooxidation of methanol produces CO₂ and H₂O as end products. Here the CO₂ mass signal is monitored. As soon as the light is turned on, the CO₂ mass signal gradually starts to increase at the same time the reactants mixtures start to decrease (see **Figure 3.10 (b)**). After the light is turned off, there is neither increase in CO₂ nor decrease in the reactants mass signal, implying the reaction is non-thermal.

The second photoreactor used during the thesis work was the gas phase microreactor made from a silicon chip with a dimension of 16 x 20 mm² and 0.35 mm thick. The reactor has a large frontal circular illumination area of 0.78 cm² with the chamber volume of about 240 nl. The reactor has two inlets for gas flow and the reactor products are led to the QMS through a capillary. Details of the reactor system can be found in references[94, 97]. The test reactions used in the reactor was gas phase carbon monoxide photooxidation and ethylene photooxidation in flow mode.

Optics: The optics part consists of light sources, different set of filters, and lenses. The light source plays an important role in photocatalytic experiments. We employed both xenon (Xe) and mercury (Hg) arc lamp in the photocatalytic experiments. These light sources offer wide range of spectral wavelength approximately from ~250 nm to ~1100 nm. We used the non-polarized continuous wave 100 W Hg arc lamp (HBO) in the stainless steel photoreactor. In the silicon microreactor, we used a 1000 W Xe arc lamp. In addition to them, we also used Hamamatsu UV LED ($\lambda = 365$ to 367 nm). Use of neutral density filters and apertures allowed regulating the photon flux incident on the sample. We used Hoyo U-340 short-pass filter ($\lambda = 250$ nm to 380 nm) and Schott GG420 long-pass filter ($\lambda = 400$ nm to 700 nm) to test the samples in the UV and visible region, respectively. In addition to them, we used Oriel band-pass filter with a bandwidth of 20 nm to irradiate the plasmonically active samples close to their plasmonic resonance wavelength. A combination of high and short focal length lenses were used to focus light on the sample. A water filter was mounted in the lamp unit to remove the infrared part of the light. Typical light intensity used in this work was ranging from 20 to 350 mW/cm².

4. Nanocomposite Photocatalysts

This chapter deals with the effects of incorporating carbon and metals in the form of a nanometer thick film or as nanosized particles in the TiO₂ photocatalyst system. It also presents insights into underlying mechanisms of photocatalytic activity of such nanocomposites. The chapter is divided into two parts: the first part outlines the role of carbonaceous materials and the second part highlights the effects associated with optically active metallic NPs with emphasis on LSPR-related phenomena.

4.1. Nanocomposites with Carbon and Optically Active Metal NPs

As discussed in the chapter 2, the quantum efficiency of TiO₂ in solar energy applications is restricted by light absorption only in the UV and the fast photogenerated electron-hole recombination. Some of the approaches have already been mentioned in that chapter as to how to minimize these problems. Here, we concentrate on the approach of designing nanocomposite functional photocatalysts using either carbonaceous nanomaterials or metallic NPs in the TiO₂ matrix. The term nanocomposite refers to the dimension of the constituting materials (< 100 nm) and their synergy effect.

The thickness of TiO₂ studied in this thesis has been restricted to be in the nanometer range (below 100 nm). Two requirements should be generally satisfied for an efficient transformation of solar energy: (i) higher light absorption and (ii) efficient separation of photogenerated charge carriers without recombination. The first process requires thicker films to absorb more light. The second process requires thin films to separate charge carriers effectively with minimal recombination. There is a trade-off between light absorption and charge separation in terms of choosing the thickness of materials. This problem can be alleviated with the help of nanocomposites without compromising the chosen TiO₂ thickness[30, 81].

Two model nanocomposites schemes have been investigated in this thesis with the aim of improving the charge carrier separation and extending the light absorption into the visible range. The first design is based on nanometer thin of TiO₂/carbon films, where the carbon is in the form of graphite, graphene or amorphous carbon. The second composite scheme consists of thin TiO₂ films decorated with metallic NPs. It is designed with the aim of addressing the role of LSPR effects in TiO₂ photocatalysts. Attention is paid in both cases to understanding charge carrier dynamics in TiO₂ using different spectroscopy methods.

4. Nanocomposite Photocatalysts

4.2. TiO₂/Carbon Nanocomposites

Carbon materials in different forms and with different properties play important roles in heterogeneous catalysis processes acting as an adsorbent, catalyst support or even as catalyst on its own[98]. The attention to carbonaceous nanomaterials is due to their relatively low cost, relevant physical and electronic structure, and ability to control the properties of the photocatalysts through composition and fabrication. They have greater probability and capacity to contribute to the approaches discussed in the chapter 2 for photocatalytic enhancement of TiO₂ [70, 99].

One interesting factor about carbon is its ability to form bonds in different manners with its neighboring carbon atoms, resulting in different allotropes. Graphite and diamond are the naturally occurring crystalline form of carbon. However, there exist a large number of other synthetic or natural carbon materials in different forms: carbon nanotubes, fullerenes, glassy carbon, highly ordered pyrolytic graphite (HOPG), activated carbon, carbon black, amorphous carbon, etc. Since graphene and graphitic-like carbon have been used in this thesis, some of their physical and electrical properties relevant for the photocatalytic applications will be briefly presented in the following sections.

4.2.1. Graphite

Graphite is a naturally occurring mineral with layered and planar structure. It has sp² hybridization configuration in which one s-orbital and 2-p orbitals are hybridized, forming three σ (sigma) bonds in a trigonal fashion with three neighboring carbon atoms. The σ bond is very strong and rigid forming the layered planar hexagonal or aromatic rings structure (graphene) along the plane (basal plane). The remaining P_z orbitals of the carbon atoms form the so-called π (pi) bond. The π bond is relatively weaker and delocalized over the entire layer. The planar-layered structure of sp² carbon atoms are connected either side by these π bonds, giving rise to 3-dimensional graphite. Due to these weak π bonds, the sheets can slide with respect to each other. This property makes graphite as a good lubricant. The C-C distance of the planar double bonds is 1.42 Å in length whereas the distance between the planes (*c-axis*) is 3.37 Å[100].

Optical absorption and electrical conductivity in graphite is mainly arising from the delocalized π orbital electrons. The π states are weakly bound and lie closer to the Fermi energy. The bonding π states form the top of the VB and the anti-bonding π* states form the bottom of the CB. The energy separation between these two states is spanning from zero to relatively narrow value. As a consequence, the material has strong absorbance in the UV-VIS-NIR range. On the other hand, the sigma states also create bonding (σ) and anti-bonding σ* states, which are located quite far away from the Fermi level. The energy separation between them is larger compared to the π bands. Hence it is used for high

frequency applications. Graphite is highly anisotropic due to the strong covalent bonding between the atoms. As a result, it has much higher electrical conductivity along the basal plane compared to the perpendicular direction. The semi-metallic nature arises from the fact that only a low density of states (DOS) is available close to the Fermi energy compared to metals that have higher DOS [101].

4.2.2. Graphitic-like Carbon

Graphitic-like amorphous carbon represents a type of carbon, which is neither perfect crystalline nor complete amorphous. It is predominately composed of sp² microstructures lacking long-range crystalline order. It exhibits short-range order and has smaller domains of nanocrystallites.

Graphitic-like carbon were used in TiO₂/Carbon nanocomposites model studies (papers I, II, and III) and prepared in high vacuum ($\sim 10^{-6}$ mbar) by electron-beam evaporation using poly-crystalline graphite as a source in high vacuum. This process results in thin films with preferentially sp² bonded nanocrystallites (under right process conditions, see experimental sections). The property of evaporated carbon films can be well characterized by Raman spectroscopy. The Raman spectra of evaporated films indicate generally the ratio of sp² and sp³ contents present in the films.

Figure 4.1 shows typical Raman spectra of thin (~ 20 nm) evaporated carbon films prepared in this work. The Raman spectrum of annealed ($\sim 800^\circ$ C) films has 2 well-resolved peaks that are characteristic for graphitic-like carbon [102, 103]. The peak located around 1380 cm^{-1} , called the D-peak, is assigned to a so-called breathing mode of six-fold carbon rings, and the peak appearing around 1580 cm^{-1} , called the G-peak, is associated with stretching modes in the carbon rings. The D-peak normally appears for defective graphite and indicates nanocrystallites in the films. At the same time, narrow and well-resolved D and G peaks represent existence of larger crystallites in the structure. Note that the D- and G-peaks of as-deposited films merge with each other (and broader), implying smaller crystallites with more amorphous nature.

Another way of assessing the quality of graphitic-like carbon films is to measure their electrical resistivity. The standard way of measuring electrical resistivity of thin films is the four-point probe method. The measured sheet resistivity (R_s) of carbon films of different types and annealing conditions is summarized in **Table 4.1**. The resistivity was measured across several different places on the surface. From Table 4.1, it is evident that the annealed carbon films have improved conductivity and good homogeneity.

4. Nanocomposite Photocatalysts

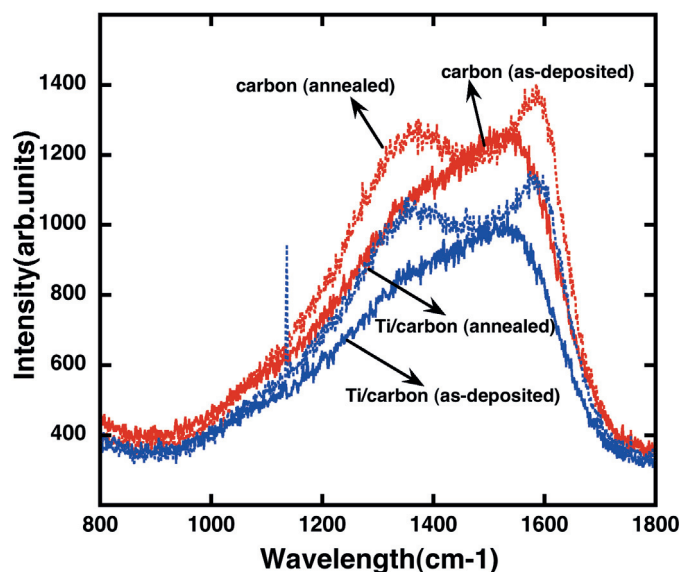


Figure 4.1: Raman spectra of 20 nm thick evaporated carbon films with and without a thin titanium adhesive layer. Annealed films exhibit two well-resolved peaks, which are not visible clearly for as-deposited films.

Interesting to note here is that a thin titanium adhesion layer (~3 nm) beneath carbon promotes graphitization and yields lower resistivity. Annealing temperature also influences the degree of crystallinity in the films. The increased conductivity of annealed carbon films is a result of restoring of sp^2 bonding in the network.

Table 4.1: Effect of annealing temperature on the sheet resistivity of e-beam evaporated carbon films

Annealing temperature (° C)	Ti (~3 nm)/carbon (20 nm) R_s ($K\Omega/\square$)	Carbon (20 nm) R_s ($K\Omega/\square$)
Room Temperature	2.29	67.58
	2.24	67.96
	2.25	68.26
500	1.60	1.81
	1.58	1.82
800	0.79	1.57
	0.78	1.61
	0.80	1.58

4.2.3. Graphene

Graphene is a 2-dimensional, single-atomic plane, and flat honeycomb structure. It is the basic building block for all other dimensionality carbon materials. The 2-D nature of the crystal renders unique physical and chemical properties to graphene. These unique properties are interesting for wide range of applications such as electronics[104], (photo)catalysis[105, 106], energy storage[107], solar cells, etc. Being one atom thick, it has good optical transparency in the visible range (~90 %) [108], which makes graphene a potential candidate in opto-electronics applications[104]. Charge carriers can travel thousands of interatomic distance before collision in graphene. The charge carrier mobility can reach up to $15,000 \text{ cm}^2 \text{ V}^{-1} \text{ S}^{-1}$ at ambient conditions and is weakly dependent on temperature[109]. In addition, graphene possesses high surface area, good thermal, and mechanical properties. More details about graphene and its related properties can be found elsewhere[109, 110]. Some of these properties are also of interest for the TiO₂ photocatalytic applications. With the advent of different preparation methods, it is easy to synthesize graphene with low cost and high quality[111-115]. All these factors make graphene a potential candidate in the TiO₂ photocatalytic systems. There are several reviews in the literature focusing on the contributions of graphene to the TiO₂ photocatalyst systems[99, 105, 114, 116-118].

4.2.4 Role of Carbonaceous Materials in TiO₂ Photocatalysis

Carbon in different forms can contribute to improve the photocatalytic governing parameters such as light absorption, surface area, and charge carrier dynamics. Some of the proposed effects contributing to better photocatalytic performance is illustrated in **Figure 4.2** and is summarized in **Table 4.2**.

Surface area modification: Carbon has earlier been mainly used as a support for metal catalysts to maintain a highly dispersed state of the active phase[119]. Activated carbon (AC) has been extensively used for this purpose, i.e. to provide high surface area for TiO₂. AC is a porous amorphous carbon structure with porosity ranging from less than 1 nm (micropores) to greater than 25 nm (macropores) and has high surface area of about ~700 to 1200 m²/g[120]. The support also enhances immobilization of TiO₂ powders. The AC material is not merely a support but to some extent its interaction with TiO₂ can also influence the photoactivity (a synergy effect)[119]. The origin of this effect arises from higher adsorption of the reactants on the AC surface followed by transfer of the reactant molecules to TiO₂ through the interface between TiO₂ and AC[121-123].

Bandgap narrowing: Bandgap engineering is aimed intentionally at narrowing the bandgap of TiO₂ in order to extend light absorption into the visible region. Though there

4. Nanocomposite Photocatalysts

have been attempts of using various metallic dopants, bandgap narrowing demonstrated with carbon has gained significant attentions[72, 73, 123]. Though the exact mechanism of carbon doped TiO_2 is still debatable, it is accepted that the addition of carbon in the TiO_2 lattice causes a significant bandgap narrowing[124], resulting in red shift of the absorption spectrum ranging from about 0.1 eV to 1.05 eV[123]. The difference in red shift is assigned to how the carbon dopant replaces atoms in the lattice and in general depends on the preparation methods. The nature of carbon dopant state in the TiO_2 lattice has been claimed to form different bonds such as Ti-C, O-Ti-C or states such as C 2p

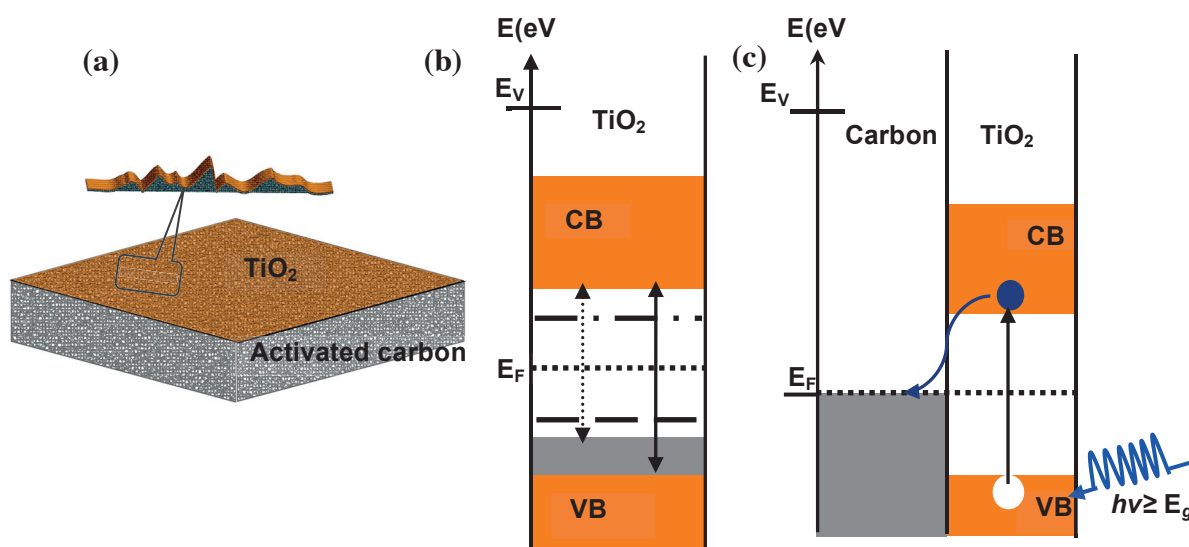


Figure 4.2: (a) Surface area modification of TiO_2 deposited on activated carbon (b) Energy level diagram of carbon-dopant induced localized energy levels in the TiO_2 bandgap (Horizontal broken solid lines) and bandgap narrowing of TiO_2 (vertical dotted line). The solid vertical line represents the bandgap of undoped TiO_2 (c) Energy level diagram of charge carrier separation at the interface between conducting carbon and TiO_2 . Here E_v and E_f denotes the Fermi and vacuum energy level positions.

mid-gap states caused by mixing of the O 2p and C 2p states[123]. In other words, carbon as dopant introduces either different localized energy levels in the bandgap or broadens the valence band. It is also demonstrated that the concentration of carbon doping in TiO_2 is one important factor for observing visible light activity of TiO_2 . For example, low carbon content does not lead to any significant visible light activity whereas larger carbon content leads to visible light activity[75]. Several studies demonstrated photocatalytic water splitting and organic compound degradation in the visible region for carbon-doped TiO_2 [72, 73, 123]. The photocatalytic enhancement achieved in the visible region seems to correlate with the preparation method. Some studies have pointed out that carbon dopant states in TiO_2 are highly undesirable because they promote charge carrier recombination[125]. It should be noted that visible light absorption in TiO_2 /carbon system does not directly imply enhanced photocurrent or photocatalytic activity in the visible region[126]. Some studies even have pointed out that electronic interactions

4.2. TiO₂/Carbon Nanocomposites

between carbon and TiO₂ at the interface causes the visible light activity[117, 127, 128].

Charge carrier dynamics: Carbon plays vital roles in suppressing charge carrier recombination in TiO₂. The ability to suppress charge carrier recombination lie in the conducting properties of carbon as well as in its favorable energy level positions with respect to the TiO₂ conduction band. In this regard, fullerene (0-D)[129, 130], carbon nanotubes (CNTs, 1-D)[128], graphene (2-D)[114], and graphite (3-D)[131] have similar ability to suppress charge carrier recombination in TiO₂ composites.

Upon illumination of TiO₂ with a UV photon, an electron in the VB is excited to the CB, leaving a hole in the VB. The excited electron is transferred to the adjacent carbon film. In this way, conducting carbon materials act as sink for photogenerated electrons[132, 133] and thereby improve charge carrier separation in TiO₂. The proposed mechanisms for charge carrier separation is the same for all types of conducting carbon materials[134]. However, factors such as interfacial area, defects, optical, and electronic properties differentiate their performance. For example, CNTs have the capacity to store 1 electron per 32 carbon atoms[133]. The electron storage of conducting carbon is assigned to a large array of carbon double bonds and defects in it[133, 135]. The conducting nature of carbon improves charge transport in composites, for example, when it is anchored with dye-sensitized solar cell[136].

Table 4.2: Different forms of carbon used in TiO₂/Carbon composites and their contributions to the photocatalytic performance

Types of carbon	Role of carbon in TiO ₂ matrix	Improved TiO ₂ parameters
Activated carbon, carbon black	Support	Surface area
Carbon atoms	Dopants	Visible light absorption
Carbon nanotubes (CNTs)	Composites	Surface area, light absorption, charge carrier dynamics
Graphite	Composites	Charge carrier dynamics, light absorption
Graphene	Composites	Surface area, light absorption, charge carrier dynamics
Fullerene	Composites	Charge carrier dynamics

CNTs and graphene have the capacity not only to prolong the charge carrier lifetime but also improve the surface area and extend the light absorption into the visible region. In this way, they contribute to achieve all of three approaches discussed in the chapter 2 for the photocatalytic enhancement of TiO₂. Based on the discussion above and from the results obtained from the thesis, the contribution of the following three parameters are suggested for the improved carrier separation in TiO₂/Carbon composites:

4. Nanocomposite Photocatalysts

- 1) Band level alignment
- 2) Maximized physical interface
- 3) Electrical conductivity

4.3. TiO₂/Metal Nanocomposites

4.3.1. Metals as co-catalysts

Addition of metal particles as co-catalysts to the semiconductor-based photocatalytic systems has several effects on their performance. In such functional co-catalyst systems, metal particles like Au, Ag, and Pt not only provide active sites for chemical transformations but also act as charge separation center to accept photogenerated electrons from TiO₂[30]. However, this functional co-catalyst system does not address the problems of extended light absorption, light penetration depth, minority charge carrier diffusion, etc., in the semiconductor[30]. These problems can be addressed with the help of designing TiO₂/Metal NP composite systems.

4.3.2. Metals at Nanoscale

Metals at nanoscale (<100 nm) possess some unique properties in comparison to their bulk counterparts. When approaching materials dimensions down to the nanoscale, two interesting physical phenomena become clearly visible in favor of photocatalysis. The first one is that the surface to volume ratio increases i.e. the number of surface atoms is higher than the bulk atoms. This phenomenon not only affects the thermodynamic properties but also dramatically affects the electronic structure and its associated optical properties of metals. The second phenomenon relevant for catalytic applications is associated with shorter charge transfer path lengths. New effects are observable when the particle size is shorter than the mean free path. In the next section, we will discuss the so-called nanoparticle plasmon resonance phenomenon and their associated effects.

4.3.3. Localized Surface Plasmon Resonance

Localized Surface Plasmon Resonance (LSPR) is one of the unusual optical phenomena manifested in metal particles at nanoscale resulting in enhanced light absorption and scattering in the near UV-VIS-NIR ranges. Excitation of LSPR arises from the resonant interaction of a metal's electron cloud with the incident light[29]. This interaction causes polarization in the metal NPs, i.e. displacement of the free electrons collectively and coherently with respect to nuclei. The positive nuclei (more correctly the atoms minus their valence electrons, usually called the "core") act as a restoring force in

a similar way as in a simple harmonic oscillator. As a consequence, the electronic cloud oscillates forth and back with respect to the positive core. At certain frequency, the oscillation of the electronic cloud is in resonance with the incoming light frequency. This frequency is called the (localized) surface plasmon frequency and lies in the near UV-VIS-NIR ranges for metals like Au, Ag, etc. The similar excitation of a plasmon in a continuous metal thin film is called a *propagating* surface plasmon resonance, since the plasmon wave travels along the metal and the dielectric interface. On the other hand, the excitation in metal NPs is called a *localized* surface plasmon resonance (non-propagating).

LSPR is strongly sensitive to the shape, size, and specific material of the NP, and also to the local dielectric environment. An important feature of LSPR is that the resonance frequency can be tuned to a desired range by manipulating those parameters. The exact solution of light extinction (sum of absorption and scattering) by small spherical NPs was presented analytically by Gustav Mie in 1908 by solving Maxwell's equation[29]. There are different numerical models proposed to find an exact solution also for different shapes of metal NPs. With the help of the electrostatic approximation model, one can simply explain the physical origin of LSPR. This model assumes the size (R =radius) of the NP to be much smaller than the wavelength of light (λ), i.e. $R \ll \lambda$, so that the electric field is constant (static) over the particle at a specified time. This results in excitation of a surface plasmon as a dipolar mode, as shown in **Figure 4.3**, with polarizability as expressed by,

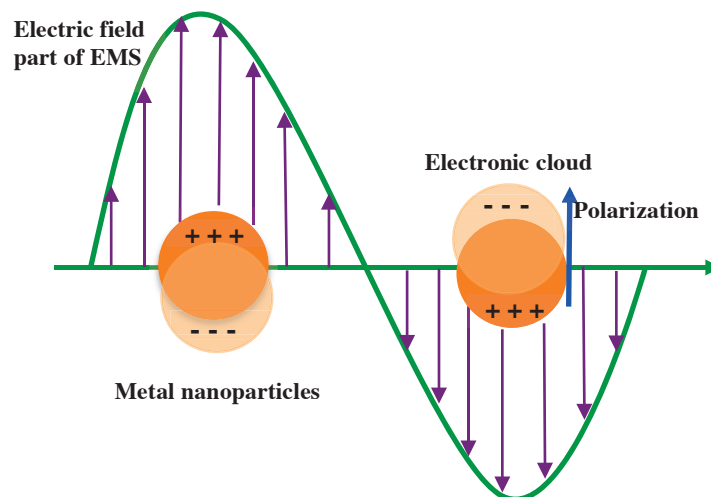


Figure 4.3: Schematic representation of the excitation of dipolar mode LSPR in a metal NP. Upon interaction with light, the electronic cloud in the metal NP is displaced with respect to fixed positive core creating a dipole. The Coulombic interaction acts as a restoring force to bring back the electronic cloud into equilibrium.

4. Nanocomposite Photocatalysts

$$P = \alpha \varepsilon_0 \varepsilon_m E_0 \quad (4.1)$$

$$\alpha = 4\pi R^3 \frac{\varepsilon - \varepsilon_m}{\varepsilon + 2\varepsilon_m} \quad (4.2)$$

where P , α , E_0 , ε_0 , R , ε_m , and ε are the dipole moment, polarizability, incident electric field, the vacuum permittivity, radius of the metal particle, the dielectric constant of the surrounding medium, and the complex dielectric constant of the metal particle, respectively. The complex dielectric constant of the material is described by the expression $\varepsilon = \varepsilon_{\text{real}}(\omega) + i\varepsilon_{\text{ima}}(\omega)$, where the real part represents polarization and the imaginary part represents energy loss such as absorption and scattering[29]. The resonance condition for LSPR is obtained by setting the denominator of the expression 4.2 to zero, i.e. $\varepsilon_{\text{real}}(\omega) = -2\varepsilon_m$ ($\varepsilon_{\text{ima}}(\omega) = 0$).

The dielectric function of a metal according to the Drude model can be expressed as [137],

$$\varepsilon = 1 - \frac{\omega_p^2}{\omega^2 + i\gamma\omega} \quad (4.3)$$

$$\omega_p = \sqrt{\frac{Ne^2}{m_e \varepsilon_0}} \quad (4.4)$$

where ω_p , γ , N , e , and m_e are the bulk plasmon frequency, damping constant, electron density, charge of an electron, and effective mass of the electron, respectively. Combining expression 4.2 and 4.3, one can obtain the LSPR frequency for Drude type metal NPs (assuming a negligible damping constant γ),

$$\omega_{LSPR} = \frac{\omega_p}{\sqrt{2\varepsilon_m + 1}} \quad (4.5)$$

The absorption and scattering cross-sections of LSPR for the time varying electromagnetic field with wave vector (k) can be defined as[138],

$$C_{\text{absorption}} = k \text{Im}(\alpha) = 4\pi k R^3 \text{Im}\left(\frac{\varepsilon - \varepsilon_m}{\varepsilon + 2\varepsilon_m}\right) \quad (4.6)$$

$$C_{\text{scattering}} = \frac{k^4}{6\pi} |\alpha|^2 = \frac{8\pi}{3} k^4 R^6 \left| \frac{\varepsilon - \varepsilon_m}{\varepsilon + 2\varepsilon_m} \right|^2 \quad (4.7)$$

$$\text{Wave vector } k = 2\pi/\lambda$$

$$C_{\text{Extinction}} = C_{\text{scattering}} + C_{\text{absorption}} \quad (4.8)$$

According to the above expressions (4.6 and 4.7), the scattering is proportional to R^6 whereas the absorption is proportional to R^3 implying that the scattering dominates for larger particles whereas absorption dominates for smaller particles.

The shifts in plasmon frequency of a metal NP towards the red side of the spectrum due to a change in the local dielectric environment other than vacuum can be understood as follows. The polarization field in the NP induces polarization in a nearby dielectric material at the interface. The induced polarization in the nearby dielectric reduces the restoring force of the electronic cloud and thereby decreases the frequency of the oscillation and causes red shift of the plasmonic peak. The red shift of plasmon frequency due to changes in size of NP can be explained as follows: When the particle size becomes comparable to the wavelength of the incoming light ($R \sim \lambda$), the electrostatic approximation is no longer valid in which case electrodynamics is required to solve the problem. As the particle size becomes bigger than the wavelength of the incident light, the incident electric field is not uniform over the particle at any given time. So, the collective excitation of electronic clouds will not be in phase within the particle. This will consequently cause a red shift in plasmonic resonance and broadening of the peak. This phenomenon is referred to as dynamic depolarization[139].

From the experimental plasmonic peak spectrum, one can deduce the following parameters. The plasmonic peak position corresponds to the resonance frequency of the given metal NP. The full-width at the half maximum (FWHM) of the peak represents the lifetime (T_2) of plasmon resonance as $\text{FWHM} = 2\hbar/T_2$ (for a single particle or ensembles with no spread in size and shape) i.e. the smaller the peak width the longer the lifetime and vice versa. Inhomogeneous broadening of the peak represents poly-dispersity in the particle sizes[140]. For particles smaller than the mean free path of the electrons, the surface will scatter the electronic cloud[141] and dampen the plasmon in addition to the bulk damping effects, resulting in peak broadening. For bigger particles, as shown in the expression 4.7, the scattering dominates and as a consequence the lifetime of the plasmon is reduced, resulting in peak broadening.

4.3.4. Plasmonic Energy/Charge Transfer Mechanisms in TiO₂

The lifetime of the plasmon resonance is on the order of femtoseconds[137]. The decay of the plasmon resonance can be radiative (scattering) or non-radiative (absorption in the particle itself). The plasmonic energy decay can be effectively coupled or transferred to a nearby semiconductor, for example TiO₂, which in that case is another lifetime reducing

4. Nanocomposite Photocatalysts

channel. The transferred energy/charge can be used to enhance the performance of TiO_2 . Four different possible plasmonic energy transfer mechanisms have been proposed to account for enhanced photocatalytic activity in TiO_2 /metal NPs composites[30] (see, **Figure 4.3**).

1. Near-field enhancement
2. Far-field scattering
3. Hot-electron transfer
4. Plasmonic heating

The physics behind these mechanisms and how they can be utilized in the TiO_2 photocatalyst systems is briefly described in the next paragraphs and summarized in **Table 4.3**.

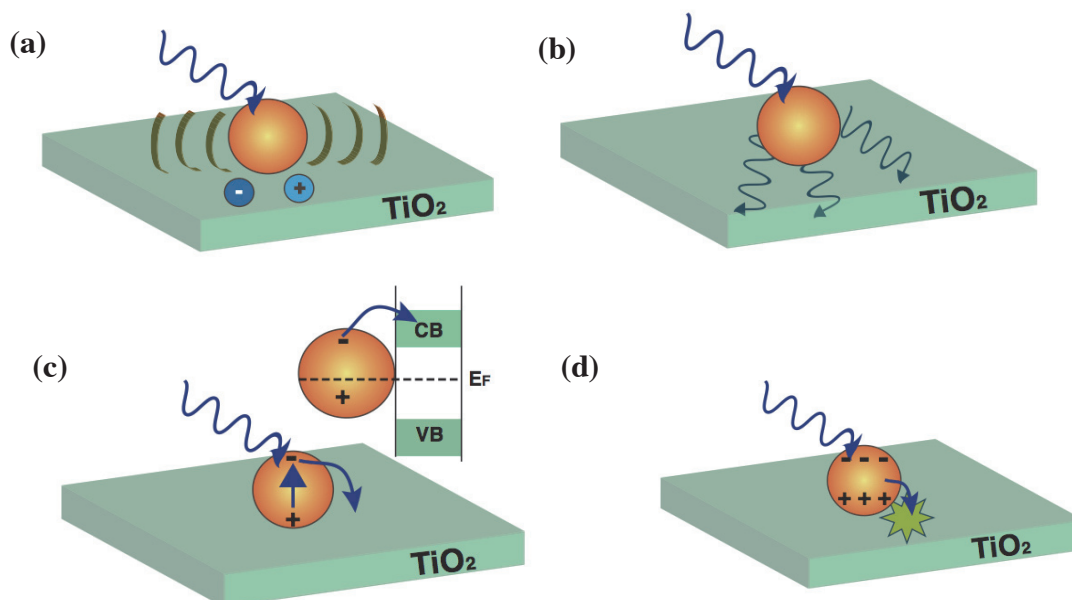


Figure 4.4: LSPR energy transfer mechanism from the metal NP to TiO_2 (a) Near-field enhancement (b) Far-field radiative scattering (c) Hot-electron transfer from the metal NP to TiO_2 (d) Plasmonic heating. For the mechanisms (a) and (b), the plasmon energy should be equal to or greater than the bandgap of TiO_2 whereas the mechanism (c) and (d) the plasmon energy does not have to be equal or greater than the bandgap of TiO_2 .

Near-field enhancement: Excitation of surface plasmon resonance creates polarization in the particle i.e. displacement of free electrons coherently and collectively with respect to the positive. These polarizations create an electric field locally around nanoparticles (both inside and outside). This field is enhanced strongly at resonance due to higher polarizability according to the equation 4.2. This non-propagating localized field in the

immediate vicinity of nanoparticles is called the near-field. The distribution of the field around the particle is not homogeneous implying that the strength of the field is higher at the edges and sharp points. The field strength has exponential decay dependence from the surface of the particles, so the field intensity is higher in the vicinity of the particles. Sometimes this intense field at resonance in the region between two closely placed particles is called ‘*hot spots*’.

From the plasmonic resonance spectrum, the lifetime of LSPR can be deduced as $T_2 = 2\hbar/\Gamma_{\text{hom}}$ [142], where T_2 and Γ_{hom} are the lifetime or dephasing time of plasmon resonance and FWHM, respectively. The dephasing time is directly proportional to the so-called field enhancement factor [142] and the parameters that affect the lifetime of the plasmon are local dielectric environment, size, and shape of the particles. The near-field is reduced for bigger particles because of creation of multipole resonance mode and dynamic depolarization of plasmon. So, in order to achieve enhanced field, the size of NPs should be $2R \leq 0.1\lambda_{\text{LSPR}}$ (5 to 20 nm in diameter) [81, 143].

The intense near-field can be used to enhance charge carrier generation rate in TiO₂ or improve separation of charge carriers generated in the TiO₂ film. In this way metal NPs can be viewed as a sub-wavelength optical antennas, which interact with external light in space and amplify and confine it down to the nanoscale locally in a nearby semiconductor. The criterion to transfer plasmon energy to the TiO₂ film through near-field effect is that the plasmon energy must be equal to or greater than the bandgap or sub-bandgap energy level of the TiO₂. The near-field effect is the basis for nanoplasmonics-based chemical and biological sensors. It has been demonstrated in several reports that the near-field effect is also the origin for enhanced photoactivity of TiO₂/metal nanocomposites in the visible region [144-147].

Far-field scattering: One of the decay pathways of surface plasmon resonance is the dissipation of the plasmon energy radiatively. This plasmon relaxation process is strongly dependent on the size of the particles as shown in the expression 4.7. According to this expression, the probability of scattering increases with bigger particle size and is dominant for particles above 30 nm sizes. The resonant far-field effect is perceived as the elastic scattering of incident light at resonance. The scattered light is symmetric in the forward and reverse directions for the particles embedded in a homogenous medium. In the case of particles placed at a TiO₂-air interface, light will then preferentially scatter into the dielectric with the larger permittivity [81]. The scattered light spreads angularly in the TiO₂ film resulting in extending the effective optical path length and thereby increases the absorption rate. The criterion to improve absorption rate through far-field scattering in TiO₂ is that the resonance energy must be equal to or greater than the

4. Nanocomposite Photocatalysts

bandgap and sub-bandgap energy levels of TiO₂. There is only a very few studies proposed this pathway for enhanced activity of TiO₂/metal composites [148].

Hot-electron transfer: One other decay pathway of LSPR is the dissipation of the plasmon energy non-radiatively, i.e. absorption of the plasmon energy (Landau damping) by the NP itself via internal e-h pair excitation. Landau damping is dominant for smaller particles ($R < 5\text{ nm}$) [149] for which the absorption cross-section is higher than the scattering cross-section. This absorption creates single photon excitation (of an e-h pair) in the metal particles. The generated hot-electron could be transferred into the TiO₂ conduction band when TiO₂ and the metal particles are in direct contact with each other and if there exists proper matching of excited hot electron energy levels in the metal with the conduction band of TiO₂. In this case, the hot-electron is transferred from the metal particles to TiO₂. For example, the Schottky barrier between Au and TiO₂ is about 1 eV, so the hot-electron should have enough energy to cross over this barrier (near the top of the barrier, but below it, tunneling may also be effective). It should be also mentioned that the e-h pair recombination rate in metals is high, so the size of the particles should be closer to the mean-free path of the electrons in the metal. However, it is not clearly understood yet as to what extent this hot-electron transfer is feasible and how the size of the particles influences the transfer rate. There are several studies that quote this mechanistic pathway for the observed enhanced photoactivity of TiO₂/metal composites [150-153] but ambiguity remains. It has been also proposed that the particle size and preparation methods play an important role here [154]. For particles smaller than the mean free path of the electron, there is likely high probability that the electrons can tunnel into the TiO₂. This decay of surface plasmon is called chemical interface damping [155].

Table 4.3: LSPR related energy/charge transfer mechanism and their effects in a nearby semiconductor

LSPR-related effects	Criteria	Possible improvements in TiO ₂ in the visible region
Near-field enhancement	$E_{\text{LSPR}} \geq E_{\text{g(SC)}}$ and $d = 0.1\lambda$	Increased e-h pairs generation/separation rate
Far-field scattering	$E_{\text{LSPR}} \geq E_{\text{g(SC)}}$ and $d \geq 30\text{-}50\text{ nm}$	Increased absorption rate
Hot-electron transfer	$d \leq 30\text{ nm}$	Increased photocurrent
Plasmonic heating	$d \leq 30\text{ nm}$	Increased catalytic activity

Plasmonic heating: This effect is similar to the third mechanism in which plasmon relaxation leads to absorption in the particle itself creating single electron-hole pair. The

4.3. TiO₂/Metal Nanocomposites

plasmons will generally relax through electron-electron (<100 fs), electron-phonon (1-10 ps), phonon-phonon (~100 ps) interactions[150]. The hot-electron transfer mentioned above should occur before thermalization of particles (lattice vibration). Otherwise the plasmon relaxation through absorption in the particles leads eventually to heating the particles. This plasmonic energy transfer mechanism is referred to as plasmonic heating. The temperature created around metal particles at resonance is high enough with relatively small optical power and is localized both spatially and temporally[156]. This effect is believed to increase the reaction rate of catalysts supported or unsupported on a metal oxide layer [157]. The thermal effect also depends on the size of the particles, geometry, heat conductivity of the surrounding medium, and the incident light intensity[137, 157, 158]. Our conclusion is that careful studies are needed to elucidate the thermal effect in photocatalysis. This mechanism is hardly quoted for TiO₂/metal NPs composites whereas it has been quoted in few studies as the origin of the improved catalytic activity[159].

4.4. TiO₂/Cu Nanocomposites

This model composite has been prepared to photocatalytically reduce CO₂ to hydrocarbon fuels using water with the help of solar energy. Since the CO₂ photoreduction process involves only water and CO₂ and it produces useful hydrocarbon fuels, it is one of the potential routes to create a sustainable carbon cycle. In other words, it is a promising way to mitigate the monotonic increase of anthropogenic CO₂ concentration in the atmosphere and associated global warming. The production of methanol and methane from the CO₂ photoreduction process requires 6 and 8 electrons, respectively as shown in the equations 4.9 and 4.10.



Figure 4.5 shows the energy band position of different semiconductors versus CO₂ redox potential at pH 5 [160]. According to this diagram, the TiO₂ conduction band position is slightly lower than the reduction potential of CO₂. The challenge here is to choose efficient co-catalyst materials to reduce CO₂. In the literature, different kinds of metal catalysts have been tested for the CO₂ photoreduction system. Among all studied metal catalysts, copper has the capability to catalyze CO₂ to hydrocarbons because of its physical and chemical structure [161-163]. In the first step of photoreduction on the metal

4. Nanocomposite Photocatalysts

electrodes, CO_2 is reduced to CO and is followed by protonation of CO to hydrocarbons. It is believed that the adsorption ability of CO on the Cu surface is neither too strong (Pt , Ni) nor too weak (Au) in comparison to other metals[161-163], thus making Cu a suitable material for the CO_2 reduction system. Detailed mechanisms of CO_2 reduction on the Cu surface can be found elsewhere[164].

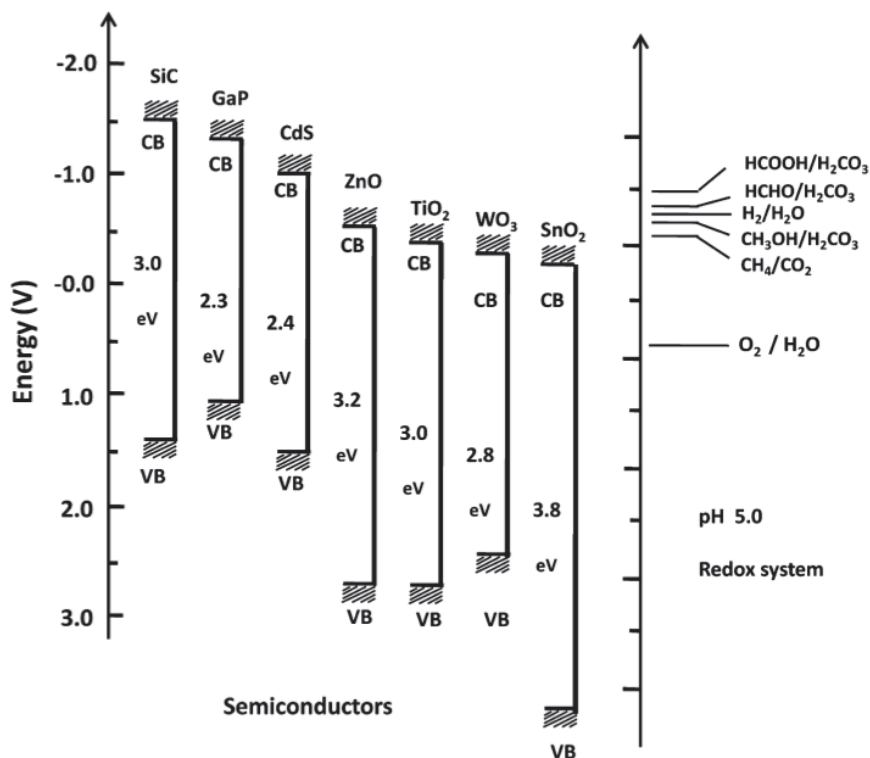


Figure 4.5: Illustration of energy band positions of different semiconductors versus water and CO_2 redox systems at $\text{pH}=5$ [160].

It has been reported that Cu particles on TiO_2 exist in different oxidation states such as Cu^0 (metallic), Cu^{I} (Cu_2O), and Cu^{II} (CuO). It has been pointed out in several studies that the Cu^{I} (Cu_2O) state is the active site for influencing the CO_2 photoreduction rate[165-167], while some other studies have pointed out that the Cu^{II} (CuO) state is the active site in such systems[168]. It is therefore important to follow the chemical stability of copper because it might affect the product selectivity. In this respect, TiO_2/Cu NPs composites were prepared to study the nature of Cu NPs in water environment *in-situ* using LSPR spectroscopy. Cu NPs were fabricated on TiO_2 films by hole-mask colloidal lithography. As a control sample, Cu NPs deposited on fused silica were used.

The chemical nature (oxidation/reduction) of copper is probed *in-situ* by simply monitoring the shift of surface plasmon resonance peak. One of the beauties of this composite system is that here Cu NPs function both as a co-catalyst to perform the desired catalytic reaction and also as a plasmonic sensor to monitor the chemical status of

the particle in real-time. In the present study (paper V), we used the Cu NPs for the latter purpose. One possible mechanism (see **Figure 4.6**) of the TiO₂/Cu photocatalytic system is assumed to be as follows[165]: First electron-hole pairs are created in TiO₂ with the help of UV light irradiation. It is believed that the Cu NPs on the TiO₂ surface can trap the photogenerated electrons. The trapped electrons are subsequently used to reduce the adsorbed CO₂ on the Cu NPs. The photogenerated holes are used to reduce water to oxygen. During the electron transfer from TiO₂ to Cu NPs, the density of electrons in Cu is increased, which gives rise to a shift in plasmon frequency. If the copper is already in an oxidized form, the transferred electrons will reduce Cu back to metallic form. Based on the position of the plasmonic peak shift, the oxidation nature of Cu NPs can be extracted along with other surface characterization techniques such as XPS.

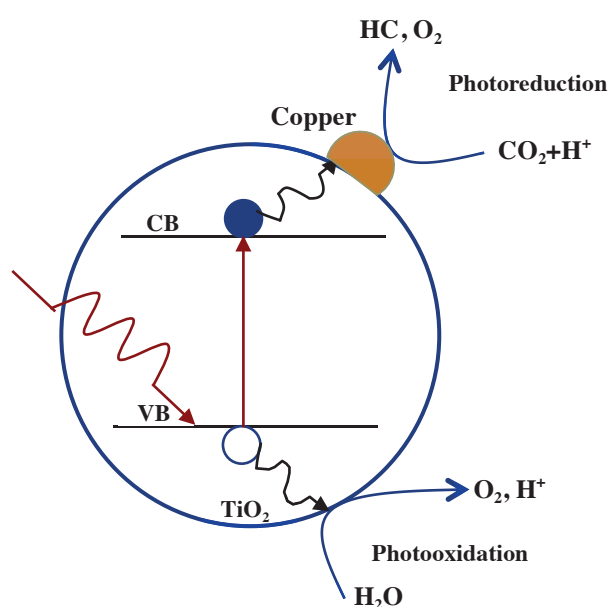


Figure 4.6: Illustration of a conceptual CO₂ photoreduction scheme on the TiO₂/Cu photocatalytic system. Here HC represents hydrocarbons such as methane.

4. Nanocomposite Photocatalysts

5. Summary of Results

This chapter summarizes the results presented in the appended papers and the results of some unpublished works. The results of the unpublished works will be found in the Appendix (A1 to A4).

5.1. Summary of Appended Papers

Paper 1

'Preparation and Characterization of TiO₂/Carbon Composite Thin Films with Enhanced Photocatalytic Activity'

Paper I describes the preparation and characterization of photocatalysts consisting of TiO₂/carbon composite films. The prepared samples have characteristics of anatase phase for titania films and graphitic-like for carbon films after annealing. The graphitic-like carbon films restrict the growth of titania crystallites in composite films. As a result, the crystallite size of titania was slightly smaller in composite films than in bare titania films, as confirmed by Raman and XRD measurements. It was observed that the optical absorption spectra of composite films red shifted in comparison to bare TiO₂. The origin of the red shift was believed to be the electronic effect between graphitic-like carbon and TiO₂ nanocrystals at the interface. The reaction performance of the investigated samples was evaluated by photocatalytic oxidation of methanol as a model reaction. The photoactivity of bare titania films was compared with composite films of similar thickness. Bare titania films with different thicknesses show less photocatalytic activity compared to composite films. We also noticed that the photoactivity of the samples increase as the film thickness increases. The increased photoactivity, as the film thickness increases, is a result of the increased optical cross-section of the films. However, if the thickness of the film reaches an optimum value, the photoactivity showed no further increment.

On the other hand, composite films show an enhanced photoactivity as compared to bare titania films. The origin of the enhanced activity was ascribed to synergy effects at the interface between the smaller nanocrystallite titania and graphitic-like carbon. The observed variation in activity for different thicknesses of composite films was understood in the same way as described for single titania films. Besides, the smaller crystalline size of titania in composite films would also contribute to improved activity via providing more surface area for the reactants.

5. Summary of Results

Paper II

'On the Mechanism of Enhanced Photocatalytic Activity of Composite TiO₂/Carbon Nanofilms'

Paper II is a continuation of paper I explaining the origin of enhanced photocatalytic activity of composite films in terms of charge carriers dynamics. The latter was studied by photoluminescence (PL). The observed PL spectra at RT were broad (extending from 450 to 750 nm) and centered around ~630 nm (1.96 eV) and ~611 nm (2.02 eV) for bare and composite films, respectively. The origin of the broad peak luminescence was attributed to self-trapped excitons (STEs) due to strong lattice-electron interaction. The increase in PL intensity for thicker films was attributed to higher optical cross-section. In comparison to bare TiO₂ films, lower PL intensity was observed for composite films. The observed PL quenching in composite film was believed to be a consequence of the efficient charge carrier leakage due to energy band alignment at the graphitic-like carbon film and titania nanocrystalline interface. In order to emphasize the band level effects, we prepared a sample consisting of a 15 nm SiO₂ spacer layer in between the carbon and titania films. Our results showed that the PL intensity for bare samples and those with a SiO₂ spacer layer are similar in PL intensity. The result suggested that the spacer layer inhibits the charge carrier transfer due to the high energy barrier for the electrons. The resistivity of the annealed carbon films was found to be relatively lower than for the non-annealed films as revealed by the four-point probe measurement. This result reflects the semi-metallic nature of the prepared carbon films. The conducting carbon possibly forms a heterojunction at the interface of titania and facilitates the effective transfer of the electrons from titania to the carbon film (band bending). The low temperature measurement (T= 10 K) revealed no trace of carbon doping in composite films. The dynamics of photogenerated charge carriers were measured by time-resolved PL measurements to probe the influence of the carbon films in composites. We estimated a shorter lifetime for composite films in comparison to bare titania films. We assigned the shorter lifetime mainly to the charge carrier leakage at the interface, in addition to minor contribution of inferior crystallinity obtained from the Huang-Rhys model.

Paper III

'Influence of Synthesizing Techniques on the Photocatalytic Performance of Graphene/TiO₂ Nanocomposites'

Paper III focuses on elucidating the influence of different graphene synthesizing techniques on the photocatalytic performance of TiO₂/graphene composite systems. Graphene was prepared by widely used techniques namely catalyst-assisted chemical vapor deposition (CVD), catalyst-free CVD, and spin coating from a commercially available graphene oxide solution. The catalyst-assisted grown graphene is also called transferred-graphene, since it involves first growth of graphene on a copper catalyst

foil and then transfer of graphene onto fused silica. The catalyst-free method allows synthesizing graphene directly on fused silica without the assistance of catalysts, so it is referred to as transfer-free graphene. The solution processing technique involves deposition of graphene in solution/suspension by spin coating. Special attention was given to the electrical conductivity and surface morphology of graphene. The prepared graphene was characterized by AFM, four-point probe, and PL techniques. It was observed from AFM that graphene prepared by different methods exhibit different morphologies. It was determined from the four-probe techniques that the sheet resistivity of catalyst-assisted graphene was lowest, followed by catalyst-free and solution processed graphene. The prepared photocatalysts showed enhanced photoactivity compared to bare TiO_2 for methanol photooxidation in the UV region. However, the enhanced photocatalytic activity was different for the different preparation techniques. The enhanced activity was attributed to improved charge carrier separation as confirmed by PL measurements. It was also revealed from PL studies that the charge carrier lifetime of catalyst-assisted graphene was lower compared to catalyst-free graphene, implying that the former has fewer defects than the latter. This trend was also observed in the photocatalytic activity as well as in sheet resistivity measurements. From these results, we confirmed that graphene prepared by different techniques have great effects on the photocatalytic performance. Finally, the graphene composites were compared with composite catalysts based on graphitic carbon and Au thin films, in order to further emphasize the importance of interface and electrical conductivity on the performance of the photocatalysts.

Paper IV

'Effects of Plasmon Excitation on Photocatalytic Activity of Ag/TiO₂ and Au/TiO₂ Nanocomposites'

Paper IV deals with the role of LSPR-related effects of metal NPs such as Au and Ag on the performance of undoped TiO_2 photocatalyst systems. Plasmonic near-field, far-field, hot-electron transfer from NPs to TiO_2 and thermal effects are generally considered for photocatalytic enhancement of TiO_2 composites. The aim of this paper was to elucidate these different plasmonic related mechanisms in undoped TiO_2 photocatalysts by using different irradiation conditions to excite plasmon and semiconductor separately and simultaneously. We designed three different generic configurations in order to provide different conditions for the plasmonic excitation and de-excitation processes. In the designed configuration S1 and S3, NPs were decorated above and beneath TiO_2 , respectively and NPs were in direct contact with TiO_2 . In the designed configuration S2, NPs were isolated from TiO_2 by a thin SiO_2 spacer layer. From the SEM and optical characterizations, it was observed that Ag contained samples of configuration S3 are not stable. The fabricated samples of different configurations were then evaluated by methanol and ethylene photooxidation tests in two independent photoreactors system. Irrespective of the oxidation tests, the samples of all configurations qualitatively exhibited a significant enhanced

5. Summary of Results

photocatalytic activity compared to bare TiO₂. We suggest two possible mechanisms for the enhanced activity (i) improved charge carrier separation due to interfacial charge transfer of electrons from TiO₂ to metal NPs, when they are in direct contact with each other and (ii) plasmonic near-and far-field effects, when there is overlapping of the plasmonic band with the TiO₂ absorption band. The interfacial charge transfer mechanism was demonstrated using the samples with different configurations of Au in methanol by LSPR spectroscopy. The plasmonic near-and far-field effects were observed for Ag particles isolated from TiO₂. This was confirmed by varying the SiO₂ spacer layer thickness, since the near-field intensity has exponential distance dependence. We observed a decrease in photocatalytic performance as the thickness of SiO₂ was increased. The samples irradiated only in the visible region showed no activity, as the plasmon resonance energy is lower than the TiO₂ bandgap energy. Simultaneous irradiation of samples with both visible and UV showed no enhanced activity compared to UV illumination.

Paper V

*‘Oxidation of Copper Nanoparticles in Water Monitored *in situ* by Localized Surface Plasmon Resonance Spectroscopy’*

Paper V investigates the chemical stability of Cu NPs, deposited on TiO₂, in water under UV illumination. Disc-shaped Cu NPs (80 nm diameter) were prepared by the HCL method on photocatalytically active TiO₂ films (50 nm thick). As a control sample, we prepared Cu NPs on an inert fused silica substrate. The fabricated samples can be used as model photocatalysts for the CO₂ photocatalytic reduction system in aqueous environment. In such systems, Cu NPs act as a co-catalyst to reduce CO₂ to hydrocarbon fuels. The aim of this paper was to monitor the dynamics of copper oxide formation in water *in situ* and real time using LSPR spectroscopy. The Cu NPs here also functioned as a plasmonic sensor to probe the chemical changes. We monitored plasmonic peak shift (λ_{LSPR}) and extinction maximum (M_{EXT}) in dark and under UV illumination to investigate the oxide formation on the Cu NPs. We observed a blue shift of the plasmonic peak under UV for Cu NPs on TiO₂ and assigned it to formation of Cu oxide, shrinkage of the metallic core and partial photocorrosion. For comparison, no blue shift was observed for Cu NPs on the inert fused silica substrate. The Cu oxide formation was confirmed by post-irradiation XPS measurements. Comparing the findings made by *in situ* monitoring of the Cu NPs oxidation in water with the post-irradiation characterization analysis, we conclude that LSPR spectroscopy enables to monitor the oxide growth on the Cu NPs, even under reaction conditions.

5.2. Summary of Unpublished Results

Appendix A1: We found that the carbon nanostructures prepared by the HCL method have the ability to improve the interfacial area (between carbon and TiO_2) and the optical absorption of TiO_2 . The lack of photocatalytic activity for the nanostructured carbon/ TiO_2 in comparison to the thin carbon films/ TiO_2 was due to the left over of PMMA residues after the HCL method.

Appendix A2: We found that Au NPs prepared by the HCL method irrespective of their configurations in the TiO_2 photocatalytic system showed a negligible photocatalytic enhancement in comparison to bare TiO_2 . The result was due to the presence of PMMA residues after the HCL fabrication method. No visible light photocatalytic activity was observed for TiO_2/Au samples, since the plasmon resonance energy of the Au NPs is below the bandgap of TiO_2 . Plasmon mediated hot-electron transfer from the Au NPs to TiO_2 was not observed due to bigger size particles.

Appendix A3: We found that Au/TiO_2 nanocomposite systems under oxygen lean conditions yield H_2 and CO_2 as the end products in the methanol photooxidation test, whereas under the oxygen rich conditions, the systems yield only CO_2 . The production of H_2 was assigned to either methanol reforming or water reduction on the composites. The photochemistry mechanism was the same for Pt/TiO_2 nanocomposite systems irrespective of the oxygen's partial pressure.

Appendix A4: We found that the role of air, water, and methanol medium on the charge carrier separation rate in the TiO_2 photocatalytic system. The charge carrier separation rate in different media was demonstrated by LSPR spectroscopy. The result showed that the charge carrier separation was higher in methanol medium, followed by water and air.

6. Conclusions and Outlook

6.1. Conclusions

The central part of the thesis was to fabricate and characterize model nanocomposite photocatalysts consisting of TiO₂/Carbon films and TiO₂/Metal NPs, with emphasis on understanding their underlying photocatalytic operational mechanisms. Characterization included both physical methods to characterize the samples, and measurements of photocatalytic activity. The main preparation aim was to improve charge carrier dynamics in TiO₂ and to extend its light absorption into the visible part of the electromagnetic spectrum.

We succeeded in developing reproducible fabrication methods for making undoped TiO₂ thin films with control over the size of the nanocrystallites, morphology of the surface, and their photocatalytic activity. The prepared photocatalysts were extensively characterized by a number of analytical methods (SEM, AFM, Optical spectroscopy, XPS, Raman, and XRD) and their photocatalytic activity was tested with different experimental setups, environments, and reaction conditions.

In a similar manner, we designed, fabricated, characterized, and tested the activity of a variety of TiO₂/Carbon and TiO₂/Metal nanocomposite systems. These composite photocatalysts were used as models to elucidate the operational mechanisms under different regimes of irradiation and reaction media.

The following conclusions are drawn from the performed preparation work and experimental photocatalytic studies.

6.1.1. TiO₂ Films

- (1) The prepared TiO₂ films after annealing at 500°C yielded polycrystalline anatase phase and was confirmed by XRD and Raman.
- (2) The TiO₂ films were dense and consisted of smaller nanocrystalline particles.
- (3) Optimum thickness of TiO₂ was found to be around 50 nm for effective charge carrier transport to the surface.

6.1.2. TiO₂/Carbon Nanocomposites

- (1) Prepared carbon films after annealing at 800°C featured characteristic nanocrystalline graphitic peaks in the Raman spectrum.
- (2) Composite films exhibited a red shift in the optical absorption spectrum compared to bare TiO₂ films. It was assigned to electronic effects at the interface between carbon and TiO₂ films.

Conclusions and Outlook

- (3) Composite films showed a significant photocatalytic enhancement in the methanol photooxidation test system compared to bare TiO₂ films. The enhancement was due to efficient charge carrier separation at the interface.
- (4) The charge carrier separation was confirmed by photoluminescence (PL) measurements. We observed reduced PL intensity and shorter lifetime for the composites, indicating the leakage of photogenerated electrons from TiO₂ to the carbon films.
- (5) TiO₂/graphene samples prepared by different synthesizing techniques yielded different physical (surface morphology) and electrical (conductivity) properties, as revealed by AFM and four-probe measurements.
- (6) A significant enhanced photocatalytic activity was observed for TiO₂/graphene composites compared to bare TiO₂. The enhancement was assigned to improved charge carrier separation at the titania-graphene interface and was confirmed by PL spectroscopy measurements.
- (7) The differences in photoactivity among composites were related to the quality of graphene prepared by different methods.

6.1.3. TiO₂/Metal Nanocomposites

- (1) Three generically different configurations of TiO₂/Metal (Au, Ag) nanoparticles (NPs) were designed and fabricated to address the role of LSPR-related effects in undoped TiO₂ photocatalyst systems.
- (2) Composites showed significant photocatalytic enhancement (up to x100 for some configurations) compared to bare TiO₂ films.
- (3) The observations were statistically confirmed in two independent photoreactor systems.
- (4) The enhanced activity was attributed to (i) interfacial electron transfer from TiO₂ to metal NPs for metal NPs in direct contact with TiO₂ (ii) Plasmonic near- and far-field effects when there is an overlap of the plasmonic and TiO₂ absorption band.
- (5) The interfacial charge transfer mechanism was demonstrated using LSPR spectroscopy.
- (6) No visible light activity was observed since the plasmon energy of the prepared Au and Ag particles was below the bandgap of TiO₂.
- (7) TiO₂/Cu composites were prepared to address the stability of Cu nanoparticles in water environment.
- (8) The real time and *in situ* observed plasmon peak shifts were interpreted as evidence for the oxidation and (photo) corrosion of Cu NP.

6.2. Outlook

It has been tremendous experience to work in a field that is fairly new to me. Although we have contributed some evidences to the understandings of the photocatalytic mechanisms of the studied composite photocatalyst systems, there is still many questions to answer to improve and many aspects to explore and elucidate. We have pointed out some of these things in the Appendix. One task regarding preparation is how to get rid of PMMA residues in the HCL fabrication technique. I believe that this issue could be solved, for instance, using O₂ plasma etch or annealing the samples in a controlled environment after nanofabrication. However, it is not clear whether all kinds of nanostructured materials can be treated with these procedures.

Since methanol photooxidation has been used to evaluate the fabricated photocatalysts, it would be valuable to better understand the photochemistry mechanism of methanol reactions on the TiO₂ surfaces for these composite systems. For instance, systematically varying the partial pressures of oxygen and methanol would be a good starting point. The microreactor setup should be improved in order to accommodate different *in situ* characterization techniques such as optical UV-VIS spectroscopy and *infrared* spectroscopy, so that we can monitor different things in real time while the photoreaction is ongoing.

In this thesis, we adopted methanol photooxidation as a test system to evaluate the photocatalytic performance of the prepared photocatalysts. The samples prepared in the thesis should also be tested photoelectrochemically in the future, in order to learn more about the operating mechanisms. We have done some preliminary measurements but we faced stability issue of samples in aqueous environment.

Composite systems were designed to improve charge carrier separation and extend light absorption in the visible region. We observed improved charge carrier separation for the prepared composites compared to bare TiO₂. We observed extended light absorption in the visible region but no activity was observed from the visible region. This should be carefully looked into in the future.

Composites, under UV illumination, improve charge separation by transferring photogenerated electrons to carbon films or metal NPs. It is not clearly understood yet what these electrons might do after the charge transfer, because neither the carbon films nor the metal NPs are exposed to the reactant environment in our systems. Would these transferred electrons lead to charging effects or somehow be leaked to the surrounding environment? A careful attention should be paid on this to address the fate of transferred electrons.

Conclusions and Outlook

Interfacial charge transfer mechanism demonstrated by LSPR spectroscopy in methanol should be extended to other media and different compositions of samples. The system needs further optimization in terms of creating inert environment and interpreting observed blue shifts. Plasmonic related effects in TiO_2 should be further explored and demonstrated with designing different sizes of metallic particles and reaction environments.

TiO_2/Cu nanocomposite systems need to be optimized further in order to understand the chemical nature of Cu and its role on product selectivity. More measurements (such as photocatalytic test) and characterizations (such as XPS) are required to understand the underlying photocatalytic mechanisms in such systems.

Appendix

Additional Results not Presented in the Appended Papers

This section presents the results that are not discussed in the appended papers but are still within the scope of the thesis. Most of the results discussed in this section involve impact of NPs prepared by the hole-mask colloidal lithography (HCL) method on the TiO₂ photocatalytic performance.

Appendix 1: TiO₂/Carbon Nanostructures by HCL

It was demonstrated in paper I that model TiO₂/graphitic carbon films enhance the photocatalytic performance compared to bare TiO₂ films. The enhancement was attributed to improved charge separation at the interface between carbon and TiO₂ films. The prepared carbon films in paper I were 2-dimensional flat films. We attempted to further improve the interfacial contact between carbon and TiO₂ by fabricating nanostructured films using the HCL method. First, a thin film (~150 nm) of carbon was deposited on fused silica followed by deposition of gold nanoparticles (Au NPs) of 300 nm and 190 nm diameters by the HCL method. The Au NPs were used as etch masks for the carbon films. The etch was performed by oxygen plasma to a depth of 100 nm. Finally, the Au NPs were removed by the wet etching method (iodine-based gold etchants). The resulting structure has carbon discs of 100 nm height standing on the 50 nm thick carbon films. In addition to this type of sample, one more sample was prepared, depositing a thin layer of silver (~2 nm thick film) onto the carbon nanostructures in order to enhance the optical absorption through excitation of LSPR.

Figure A1 (a and b) shows representative SEM images of the carbon nanodiscs (300 nm diameter) with and without Ag. The discs were distributed homogeneously with short-range order. In between the discs, the surface of the carbon films appeared rougher with very smaller nanostructure that is due to oxygen plasma etching. The smaller bright feature seen on the Ag sample was the formation of smaller Ag islands. In fact, this type of carbon nanodiscs have the ability to exhibit geometric optical resonances[169]. The peak around 250 nm observed in the spectra (**Figure A2 (a)**) is assigned to plasma etch roughening of the surface[170]. In general, geometric resonance of nanostructures red shifts with increasing particle size provided that the refractive index of the material remains unchanged[170]. However, such kind of trends was not observed clearly for the fabricated nanostructures. There is, however, a small bump in the spectra around 450 nm that might be excitation of a geometric resonance of the carbon nanostructures. For the Ag samples, the peak appeared around 360 nm is assigned to excitation of LSPR in smaller Ag particles.

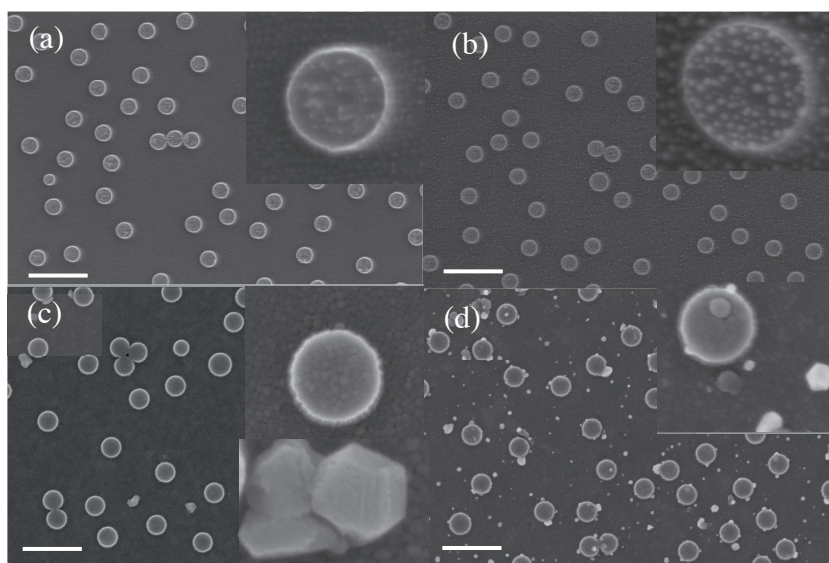


Figure A1: SEM images of HCL fabricated samples (a) Carbon nanodiscs (b) Carbon nanodiscs with Ag NPs (c) and (d) SEM images of (a) and (b) after the deposition of TiO₂. The top insets in all images show magnified versions of single NP. The bottom inset in (c) shows a hexagonal crystalline feature. The size and height of discs are 300 nm and 100 nm, respectively. The discs are supported on 50 nm thick carbon films. The scale bar on all images is 1 μm.

Figure A1 (c and d) shows SEM images of carbon nanostructures after the deposition of a 50 nm thick TiO₂ films. The prepared TiO₂ films were very dense and consisted of smaller grains/particles observed clearly in the top inset of **Figure A1 (c and d)**. The bottom inset of **Figure A1 (c)** shows some layers of hexagonal structure. Such structures appear randomly across the sample. They are considered to be formation of crystalline graphitic flakes resulting from smaller nanostructure in between the carbon discs after thermal annealing. However, they are not visible for the bare carbon nanostructure. The origin of such crystalline structures is not clearly understood yet. The observed bright features in the Ag containing samples are agglomeration and protrusion of Ag particles after thermal annealing of TiO₂ at 500 °C.

The crystallinity of composites plays a very important role in governing the photocatalytic performance. Raman spectroscopy is a good tool to assess both TiO₂ and carbon crystalline structure. **Figure A2 (b)** displays Raman spectra of composite nanostructures with and without Ag nanoparticles. The peaks observed at around 148, 199, 391, 502 and 631 cm⁻¹ are characteristics of the anatase phase of TiO₂[131]. The peaks at around 1341 and 1581 cm⁻¹ are typical peaks of nanocrystalline graphitic carbon films as described in the chapter 4. It is confirmed from Raman studies that the carbon layers have graphitic-like crystalline structure and TiO₂ is composed of the polycrystalline anatase phase. In addition to that, the peak intensity (148 cm⁻¹) of the Ag

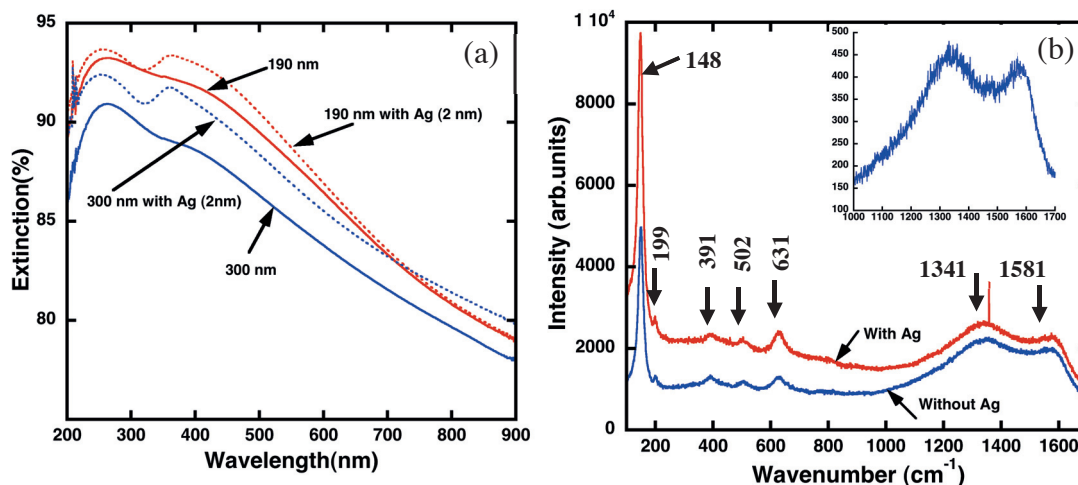


Figure A2: (a) Optical extinction spectra of carbon discs of 190 nm and 300 nm diameter with (solid line) and without Ag (dotted line) (b) Raman spectra of TiO₂/carbon discs with and without Ag. Inset shows the Raman spectrum of bare carbon discs.

sample is almost one order of magnitude higher than the sample without Ag. This enhanced peak intensity is attributed to surface enhanced Raman scattering due to LSPR effect of Ag NPs. It is also noticed that the Raman scattering signal of TiO₂ (148 cm⁻¹) on carbon nanostructures is slightly higher than the TiO₂ on flat thin films in paper I, implying that the carbon nanostructured surface favors improved crystallinity of TiO₂. The inset of **Figure A2 (b)** shows Raman spectra of bare carbon nanostructure, which also exhibits characteristic graphitic-like crystalline structure.

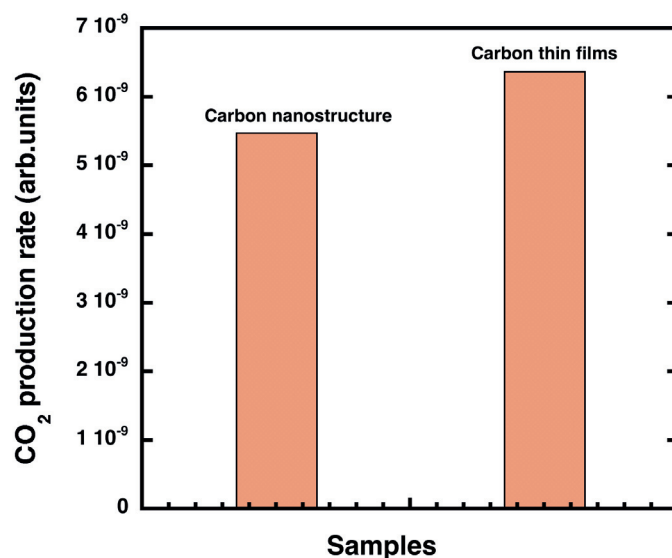
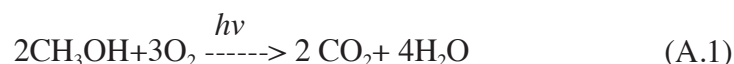


Figure A3: Comparison of the photocatalytic activity of TiO₂/carbon nanostructures with TiO₂/carbon thin films. The bar chart represents CO₂ production rate from the test reaction under UV illumination.

Appendix

The photocatalysts were tested in a home-built microreactor setup (described in paper I) using gas phase methanol photooxidation as a model reaction. The general methanol photooxidation reaction is shown in equation A.1. According to this reaction, the final products are CO₂ and H₂O. We followed the CO₂ mass spectrometer signal to estimate the photocatalytic performance of all the samples in the thesis (the detection of water is not difficult and it was not used because of complication with the background mass spectrometer signal of water). It should also be mentioned that we did not observe any intermediate products such as formaldehyde (CH₂O), formic acid (CH₂O₂), etc., during the photoreaction.



The samples were irradiated with photons in the spectral range between 250 nm to 380 nm using filtered radiation (Hoya-340 filter) from a Hg lamp source. Monitored CO₂ mass signal from this photoreaction is plotted versus time in **Figure A3**. The samples without Ag showed initially no photocatalytic activity for some hours (not shown). After that, they became photocatalytically active. On the other hand, samples with Ag showed considerable photocatalytic activity (not shown). Comparing the photocatalytic activity of thin flat carbon films and the carbon nanostructures with and without Ag, we were surprised to observe lower photoactivity for carbon nanostructures than flat carbon films. We speculate that the deposition of carbon nanostructures by the HCL method introduces impurities and in particular residues of PMMA polymer during the process. In the final step of HCL, the sample was immersed in acetone to lift-off the polymer PMMA. During this lift-off, some residues of polymers would most likely have been left on the nanostructure. May be this PMMA residues is blocking the charge carrier transfer between TiO₂ and carbon films. After a few hours of UV illumination, the PMMA layer seems to be disappearing partly or converted into some other forms and the sample started to show significant photocatalytic activity.

To summarize the appendix A1, we found that the carbon nanostructures prepared by the HCL method have the ability to improve the interfacial area (between carbon and TiO₂) and the optical absorption of TiO₂. The lack of photocatalytic activity for the nanostructured carbon/TiO₂ in comparison to the thin carbon films/TiO₂ was due to the left over of PMMA residues after the HCL method.

Appendix 2: TiO₂/Metal Nanocomposites by HCL

Paper IV discusses the effect of metal NPs in different configurations with respect to the reaction environment. In Paper IV, the size of the NPs was not varied and deposited by thermal evaporation. Prior to this work, an attempt was made to manipulate the size of metal NPs in order to tune the plasmon resonance over different spectral regions. We chose to prepare Au NPs by the HCL method on a 25 nm thick TiO₂ films. SEM images of fabricated Au nanoparticles of different sizes are shown in **Figure A4**. The prepared TiO₂ films were composed of smaller crystallites or grains, as seen clearly on the first 2 images in the first row of figures. These images indicate the *polycrystalline* nature of the prepared TiO₂. The particles were distributed homogeneously as 2-dimensional arrays with short-range order and the variation in particles size is clearly observable. The surface coverage of the particles was evaluated by the ImageJ software tool and is summarized in **Table A1**.

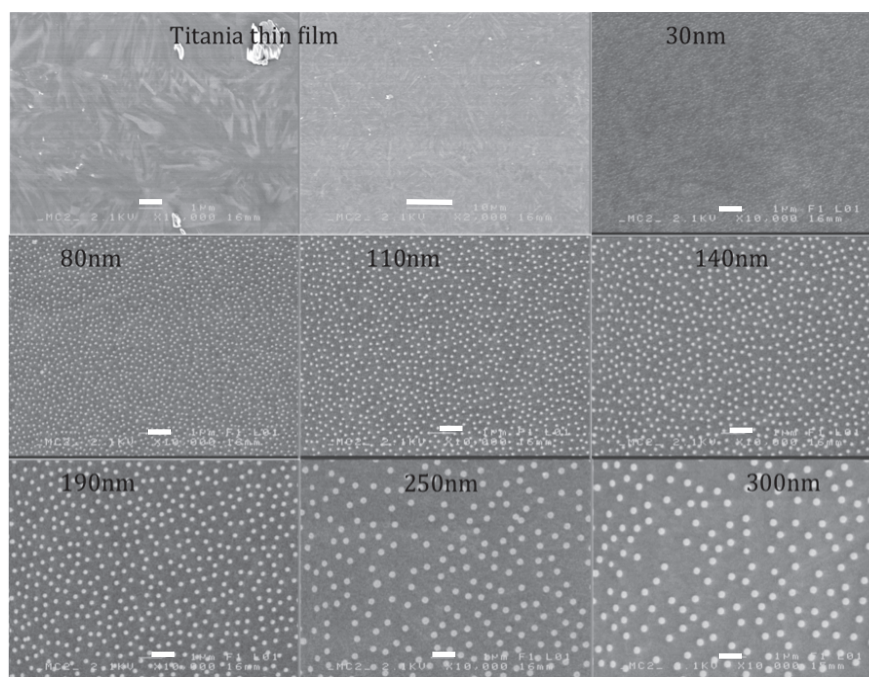


Figure A4: SEM images shows the size and distribution of Au NPs prepared by HCL. Here NPs are decorated on 25 nm thick TiO₂ films. The first 2 images in the row 1 represent thin films of TiO₂. The scale bar on all images is 1 μm except the second image in the first row (10 μm).

Optical characterization was performed by spectrophotometry in transmission mode as shown in **Figure A5**. The increased in absorption in the visible to near-infrared range for all composites is the excitation of LSPR modes in the Au particles. The peak shift is consistent with increase in particle size since the plasmon resonance is sensitive to size of the particle. As the particles size becomes bigger, the peak shifts toward the red side of

Appendix

the spectrum. The difference in peak intensity is due to difference in surface coverage of the particles. For bigger particles (250 and 300 nm), the peak broadening is dominant due to more damping in bigger particles. On the whole, the fabricated composites have well defined optical extinction across the VIS and NIR ranges. The small steps seen at 800 and/or 900 nm on the spectra are the result of detector change over and/or grating change over in the instrument.

Table A1: Distribution NPs size and coverage prepared by the HCL method

Diameter of used polystyrene (PS) colloidal beads (nm)	Mean diameter of NPs after fabrication (nm)	Surface coverage (%)
35	~31	~5.3
80	~85	~10.6
110	~106	~9.2
140	~136	~11
190	~178	~11.5
250	~260	~9.3
300	~298	~11.2

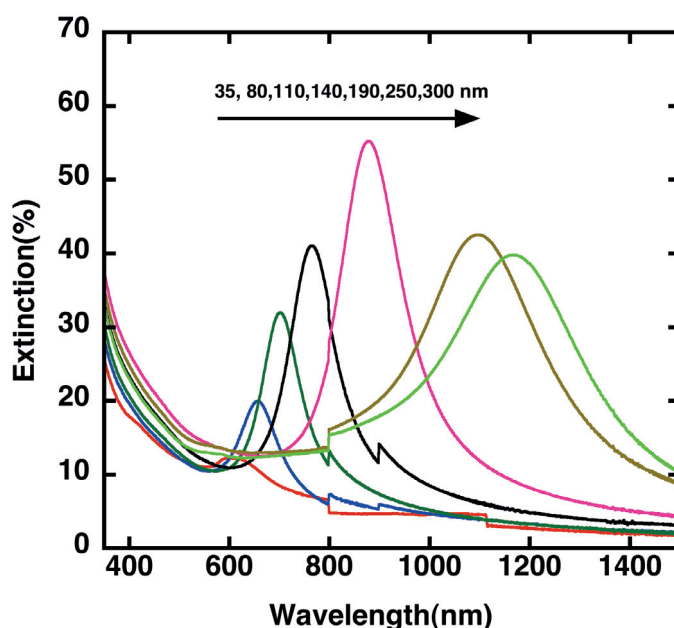


Figure A5: Optical extinction spectra of Au NPs with different diameters prepared on 25 nm thick TiO_2 films by the HCL method.

The samples were tested in a microreactor (made from a silicon chip) using photooxidation of carbon monoxide in flow mode in the UV region ($\lambda < 380$ nm). The tested samples showed photoactivity that is more or less closer to that of bare TiO_2 (not shown). There was no visible light photoactivity observed while irradiating samples at

their plasmon frequency. As explained in paper IV, the plasmon energy is not enough to induce e-h pairs generation/separation in TiO_2 through near-and far-field effects. The observed lower photoactivity in the UV region compared to NPs prepared in paper IV can be explained clearly with **Figure A6**. As it can be seen from the figure, the sample composed of Au (140nm) NPs on TiO_2 films (**Figure A6 (a)**) showed no photoactivity up to a few minutes and then started showing a significant activity. The sample composed of Au (80 nm) placed beneath TiO_2 (**Figure A6 (b)**) showed photoactivity comparable to bare TiO_2 . The result is really contradictory to what was expected for these types of composites. We speculate that some PMMA residue is present at the interface between TiO_2 /Au NPs resulting in hindering interfacial charge transfer from TiO_2 to Au NPs. After a few minutes, the residue is likely removed (oxidized) by TiO_2 and thus showed significant photoactivity.

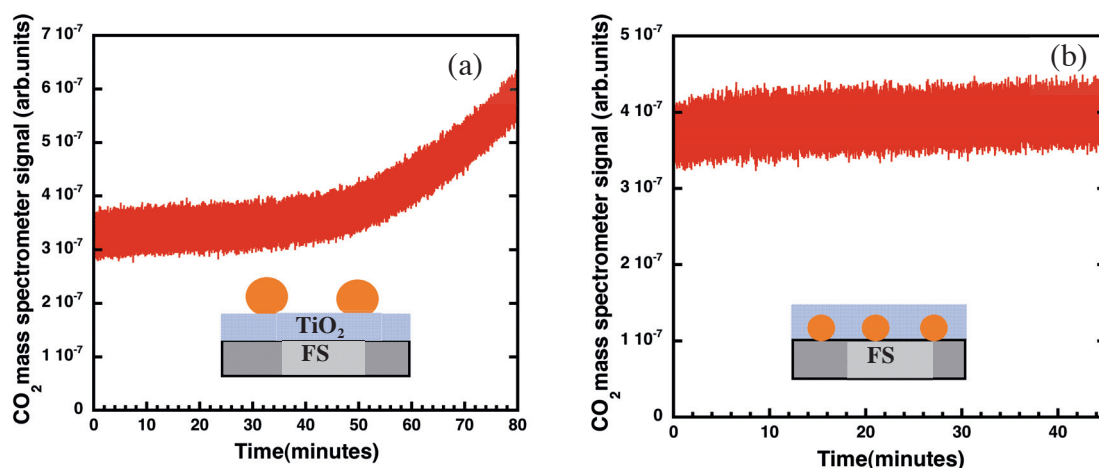


Figure A6: The mass spectrometer signal of CO_2 ($m/z=44$) for the photocatalytic performance of (a) Au(140 nm) on TiO_2 (b) Au(80 nm) beneath TiO_2 prepared by the HCL method. FS in the schematic denotes fused silica substrate.

To summarize the appendix A2, we found that Au NPs prepared by the HCL method irrespective of their configurations in the TiO_2 photocatalytic system showed a negligible photocatalytic enhancement in comparison to bare TiO_2 . The result was due to the presence of PMMA residues after the HCL fabrication method. No visible light photocatalytic activity was observed for TiO_2 /Au samples, since the plasmon resonance energy of the Au NPs is below the bandgap of TiO_2 . Plasmon mediated hot-electron transfer from the Au NPs to TiO_2 was not observed due to bigger size particles.

Appendix 3: TiO₂/Metal Nanocomposites Prepared by Thermal Evaporation

As mentioned in the appendix 2, the HCL method leaves some PMMA residues after the final fabrication on the metal NPs. These leftover residues create problems in the overall (photo)catalytic performance of the prepared model catalysts. In order to avoid this problem, the NPs were prepared by thermal evaporation of metal thin films followed by post-deposition annealing. This nanofabrication method is very easy, simple, and does not involve any polymers in the fabrication process. In this study, both gold (Au) and platinum (Pt) NPs were prepared and tested with focus on the dynamics of photocatalytic reaction under oxygen rich and lean conditions. Pt is a good co-catalyst in TiO₂ composite systems because of its potential ability to reduce water to hydrogen. The main interest, however, was about how different placements of the NPs (**Figure A9**) with respect to the reaction environment influences the photocatalytic performance.

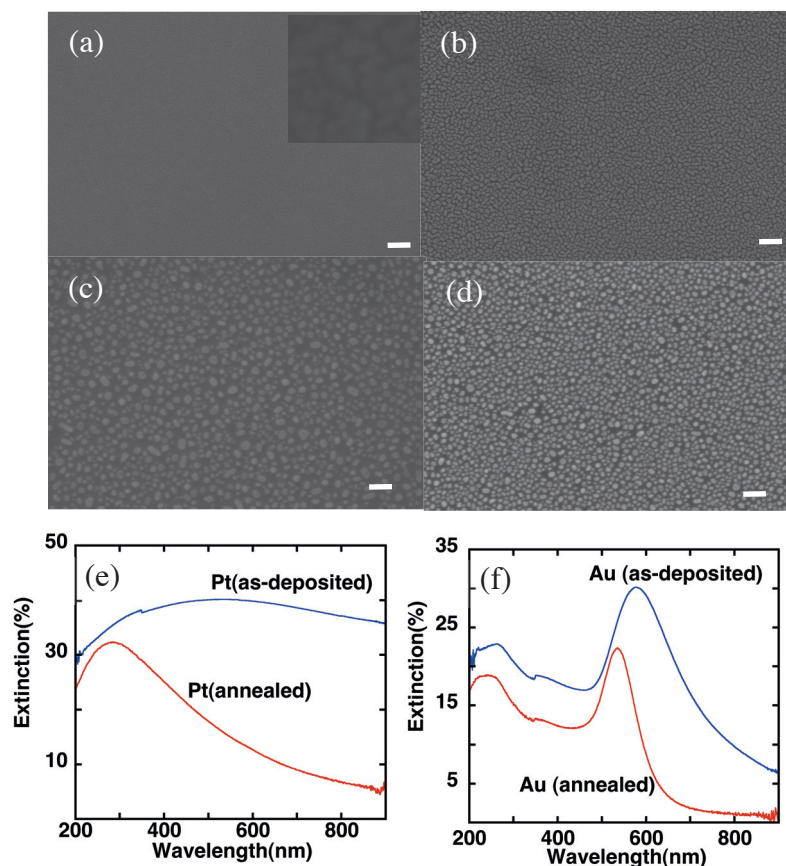


Figure A7: SEM images of as-deposited (a) Pt (b) Au thin films (c) Annealed Pt (d) Annealed Au. Inset in (a) shows a magnified image of as-deposited Pt. The scale bar on all images is 100 nm. (e) Optical extinction spectra of fabricated Pt NPs and (f) Au NPs.

Figure A7 (a-d) shows SEM images of as-prepared and annealed Pt and Au systems. The as-prepared metal thin films (nominal thickness 3 to 5 nm) appear irregular and discontinuous on fused silica but after thermal treatment they form a quasi-spherical shape. This fabrication procedure yields very dense and poly-dispersed particles with an average diameter of 25 nm to 30 nm. In principle, the surface coverage and the size of the particles can be changed by varying the deposited amount, the deposition rate and the annealing temperature.

After the thermal treatment, the Au NPs prepared by this method exhibit inhomogeneous plasmon resonances at around 536 nm (**Figure A7 (f)**). The inhomogeneity in the plasmon spectrum arises from difference in size and shape of the particles. The as-deposited Au particles show a broader and red shifted plasmonic peak at around 570 nm due to bigger size and may be also different shape particles. Excitation of LSPR in Pt NPs is different from classical Au and Ag plasmonic systems. The plasmon resonance in metals is mainly characterized by their complex dielectric function. The real part of this function represents polarization and the imaginary part represents damping such as absorption in the material. The complex dielectric function is strongly frequency dependent. Pt is characterized by a larger imaginary part of the dielectric function due to its electronic band structure. Interband transitions in Pt are predominant due to the fact that its d-band is much closer to the Fermi level compared to the case of Au where d-band is located ~ 2.3 eV below the Fermi level. This interband transition in Pt dampens the plasmon resonance in the investigated ranges (visible to near infrared) in this material. Nevertheless, an asymmetric nanoparticle plasmon resonance is observed for annealed Pt sample around 285 nm (**Figure A7 (e)**). The as-deposited Pt sample shows no peak due to more damping and lack of distinct nanostructures, as seen from the SEM images.

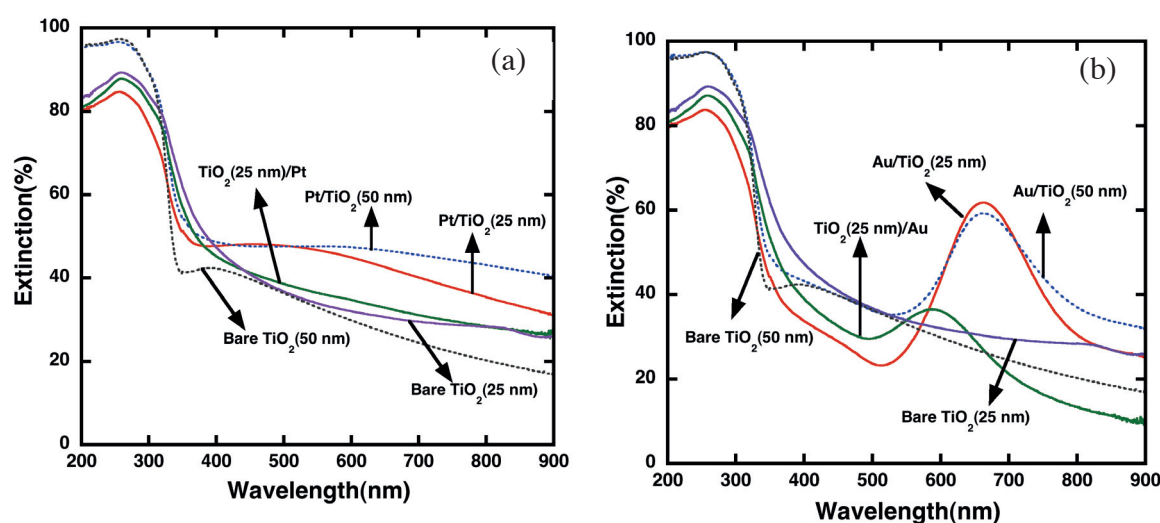


Figure A8: Optical extinction spectra of different configurations of (a) Pt-TiO₂ composites (b) Au-TiO₂ composites

Appendix

The optical extinction of the composite samples shows distinct plasmon resonance for the investigated size and shape of the particles. The red shift of the peak compared to bare Au NPs is attributed to changes in the dielectric environment of the Au particles. However, no plasmon resonance is observable for Pt/TiO₂ samples after deposition of TiO₂ films due to oxidation of Pt sample and/or overlapping of the plasmon resonance with the TiO₂ absorption band.

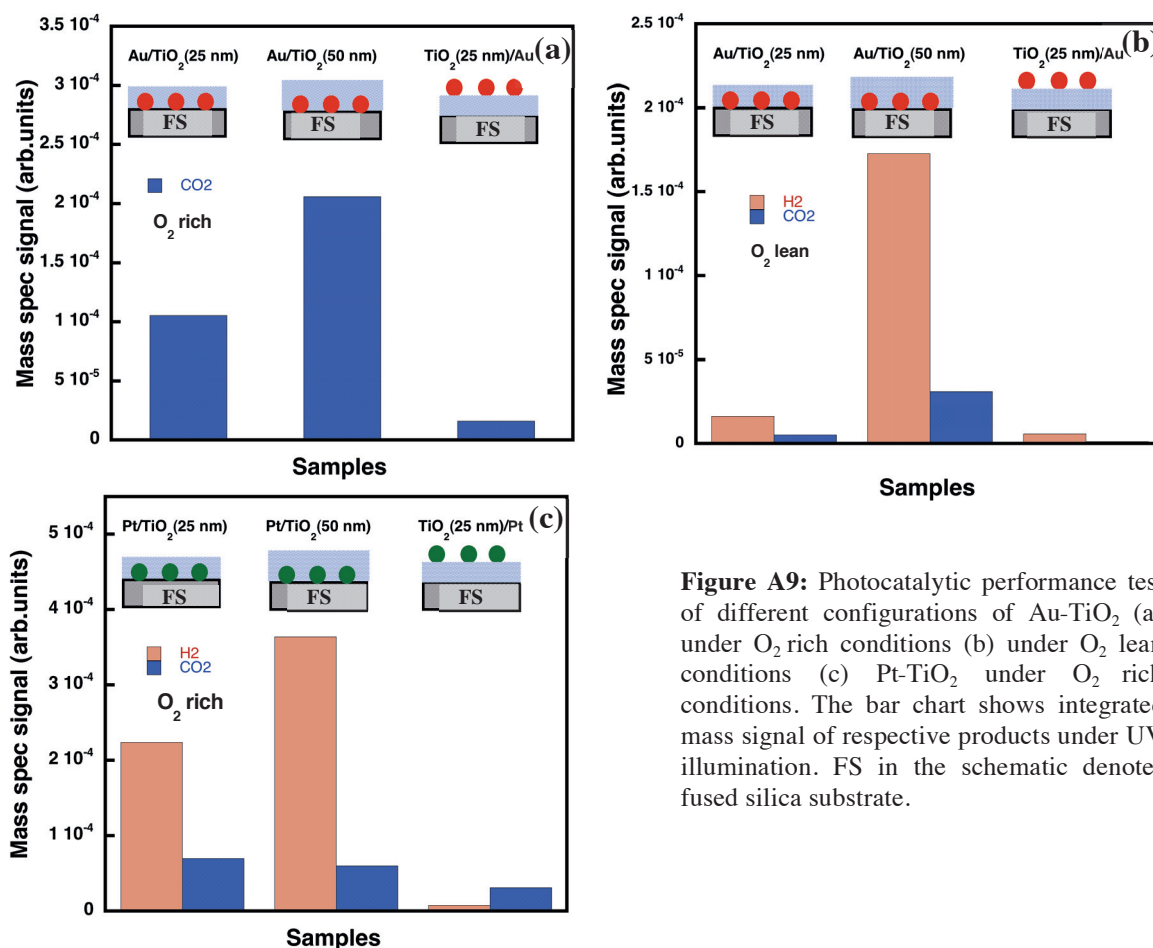


Figure A9: Photocatalytic performance test of different configurations of Au-TiO₂ (a) under O₂ rich conditions (b) under O₂ lean conditions (c) Pt-TiO₂ under O₂ rich conditions. The bar chart shows integrated mass signal of respective products under UV illumination. FS in the schematic denotes fused silica substrate.

Photooxidation of methanol was used as a model reaction to test the performance of these photocatalysts. The test was performed in oxygen-rich and oxygen-lean conditions and under UV illumination. At oxygen-lean conditions, the reactant container was evacuated/filled with nitrogen gas prior to methanol filling whereas at oxygen-rich conditions, the container was evacuated and filled with air prior to methanol filling. The results of these reactions experiment are shown in **Figure A9**. The bar chart shows the integrated CO₂ mass spectrometer signal under illumination. The Au-TiO₂ composites, under oxygen rich conditions, produce only CO₂ (**Figure A9 (a)**) as the product. The difference in CO₂ mass signals for the fabricated Au samples is related to the difference in composition and configuration of the systems. Au particles placed beneath TiO₂ showed higher activity than particles placed on top of TiO₂. The Au NPs on the TiO₂

films shadow the active layer of the photocatalyst, which explains the observed lower photoactivity. The increase in photoactivity for 50 nm compared to the 25 nm thick films is assigned to an increase in optical absorption.

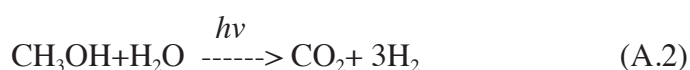
Under oxygen lean conditions, the Au-TiO₂ composites produce both hydrogen (H₂) and CO₂ as the final products (**Figure A9 (b)**). The production of H₂ is higher than the production of CO₂. The trend in activity is the same as observed for oxygen rich conditions for different configurations. The result suggests that methanol photochemistry is different under different oxygen concentrations. The details of methanol photochemistry on the TiO₂ surface are rather complex and beyond the scope of the thesis; interested readers are referred to articles in the literature[171-173]. The brief account of methanol photochemistry, which is given here, is to support the discussion of our observations. There are two possible mechanisms proposed in the literature for photooxidation of methanol[174].

- 1) Direct oxidation by photogenerated holes
- 2) Indirect oxidation via OH[•] radicals resulting from trapping of photogenerated holes by adsorbed water or surface OH group

It should be mentioned that there is a significant amount of water vapor always present in the reactor irrespective of the experimental conditions. Considering the amount of water vapor present, the second possible mechanism is most likely to occur in our case. The observed hydrogen in our case could be the result of any of the following reactions.

- (i) Methanol reforming reaction
- (ii) Partial reduction of water into hydrogen

The methanol reforming reaction is given by the equation A.2. This reaction yields H₂ and CO₂ as final products. The reaction is highly endothermic in nature so energy must be supplied in order to initiate it. This energy can be alternatively supplied by solar energy and the reaction can be boosted with the help of composite photocatalysts[175, 176].



The second possible reaction mechanism could be partial reduction of water into hydrogen by photogenerated electrons[177, 178]. The water reduction reaction on bare TiO₂ is not efficient due to the high recombination rate of e-h pairs. The reaction is more efficient when metal NPs are loaded on the TiO₂ matrix. In (almost) all of the

demonstrated studies in the literature, the metal NPs are placed on top of TiO_2 and exposed to the reactants. Under bandgap illumination of TiO_2 , the photogenerated electrons in the CB are transferred to, for example, Au NPs due to favorable energy level position and the transferred electrons subsequently reduce protons in water to hydrogen. At the same time, the photogenerated holes can be effectively scavenged by methanol. In our study, the Au NPs have been placed both on top of and beneath TiO_2 . The highest activity was observed for samples with NPs beneath TiO_2 . So, the operational photocatalytic mechanism for this type of composites should involve the transfer of photogenerated electrons to Au and subsequent reduction of water. It is possible only if the water molecules have the possibility to reach the Au NPs beneath TiO_2 . It is speculated that the prepared composites might have some nanoporosity in the structure and as a consequence, part of the NPs likely get exposed to the reactants and thereby results in producing hydrogen. Alternatively, the electrons might tunnel through TiO_2 to reach the reactants considering the reduced nature and thickness of TiO_2 films.

Figure A9 (c) shows photocatalytic measurement of Pt- TiO_2 composites under oxygen rich conditions. Here both the H_2 and CO_2 mass signals are observed even for oxygen rich conditions. The result suggests that the methanol photochemistry on Pt- TiO_2 is different from the Au- TiO_2 composite system. Pt has the capability to reduce water more efficiently than Au because the Schottky barrier is higher for Pt than Au as reported in the literature apart from being a good catalyst for water reduction[175]. It is likely that the second possible reaction mechanism proposed for the Au- TiO_2 composite system under oxygen lean conditions is a probable explanation for the observed H_2 and CO_2 production under oxygen rich conditions. The same products were observed for oxygen lean conditions for this composite system (not shown).

It should be mentioned that the results presented in this chapter are tentatively explained and discussed. These composite systems need to be further analyzed in order to get insights into the underlying mechanisms.

To summarize the appendix A3, we found that Au/ TiO_2 nanocomposite systems under oxygen lean conditions yield H_2 and CO_2 as the end products in the methanol photooxidation test, whereas under the oxygen rich conditions, the systems yield only CO_2 . The production of H_2 was assigned to either methanol reforming or water reduction on the composites. The photochemistry mechanism was the same for Pt/ TiO_2 nanocomposite systems irrespective of the oxygen's partial pressure.

Appendix 4: Effects of Hole Scavenger on Charge Transfer

One of the photocatalytic enhanced mechanisms discussed in paper IV was the interfacial charge transfer from TiO_2 to metal NPs under UV illumination when the NPs and TiO_2 are in direct contact with each other. This charge transfer mechanism was demonstrated *in situ* using LSPR spectroscopy. The measurement carried out in Paper IV was in pure methanol medium. We tested the samples of configuration S3(Au), where Au NPs are decorated beneath TiO_2 , in different media to understand the effect of the hole scavenger on the kinetics of charge transfer. The measurement setup and conditions are the same as in paper IV except that the sample of configuration S3(Au) is tested in air, water (milli-Q), and pure methanol.

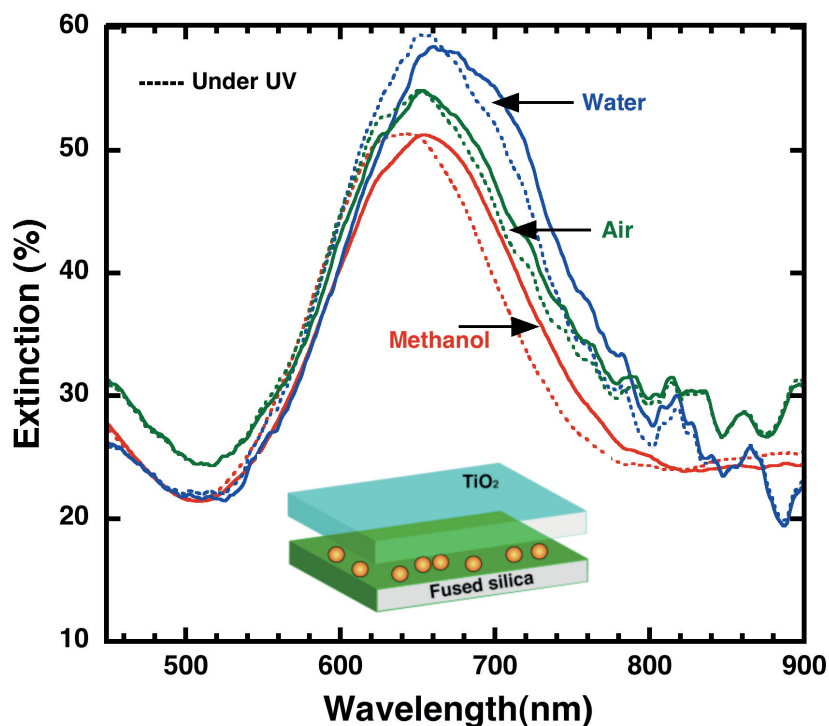


Figure A10: *In-situ* LSPR spectroscopy monitoring of S3(Au) in different media: air, water, methanol. The solid line represents LSPR peak under immersion and the dotted line represents LSPR peak position during UV illumination.

The result of the measurements from different reactant environments is compiled in **Figure A10**. Under UV illumination, the plasmon peak position is shifted towards the blue side of the spectrum irrespective of the medium (See **Table A2**). However, the shift is larger for methanol, followed by that for water and air. The magnitude of the shift reflects the influence of hole scavengers on charge carrier separation. The reason why larger blue shift is observed for methanol is that the photogenerated holes are more

Appendix

quickly trapped by methanol, since it is a better hole scavenger. As a consequence, the charge carrier recombination is greatly reduced in this medium. Water is not as good hole scavenger as methanol, resulting in slightly smaller blue shift than in methanol. The even smaller, but not zero, blue shift observed in air is due to the presence of humidity in air, which probably acts as a hole scavenger.

Table A2: Plasmonic peak shift for S3(Au) under UV illumination in different mediums

Medium	Peak shift (nm)
Methanol	~14
Water	~8
Air	~3

The LSPR spectroscopy offers great advantage of monitoring the charge transfer in real-time and *in situ* in different media. Another advantage of the plasmonic particle systems is that they can be used as a probe and co-catalysts simultaneously in these types of studies. In paper V, we have discussed this capability of using LSPR spectroscopy to monitor supported Cu NPs on TiO₂ in water in which Cu acted as a plasmonic sensor as well as a co-catalyst.

To summarize the appendix A4, we found that the role of air, water, and methanol medium on the charge carrier separation rate in the TiO₂ photocatalytic system. The charge carrier separation rate in different media was demonstrated by LSPR spectroscopy. The result showed that the charge carrier separation rate was higher in methanol medium, followed by water and air.

Acknowledgements

This thesis would not have been possible without the following people's supports and encouragements. I owe a debt of gratitude to all of them.

This work was funded by the Nordic energy council through Solar hydrogen and N-I-S-F-D projects. I like to thank the funding agencies for their financial supports.

I would like to express my sincere gratitude to my supervisor **Prof. Dinko Chakarov** for his kind guidance and continuous supports throughout my PhD. Thanks Dinko for giving me an opportunity to work under your supervision and clarifying both scientific and non-scientific things whenever I have. You have been a great support of pillar behind my academic growth. It has been really a wonderful time working with you.

I am very grateful to my examiner **Prof. Bengt Kasemo** for giving me an opportunity to work in his group. Thanks Bengt for your valuable suggestions and comments on the thesis. Also I am thankful to your motivations and useful tips in the last phase of my thesis.

All my research collaborators and co-authors are greatly appreciated and acknowledged for being helpful and open to fruitful discussions. Special appreciations are given to: Dr. Augustinas Galeckas, Dr. Vishnu, and Prof. Andrej Kuznetsov from University of Oslo; Jiefang Zhu (Uppsala University); Dr. Peter C.K. Vesborg, Morten G. Nielsen and Prof. Ib Chorkendroff (DtU, Denmark); Dr. Fernando Gonzalez Posada (Colleague, Chalmers) and Jie Sun & Prof. August Yurgens (MC2, Chalmers).

I like to thank Prof. Hannes Jonsson and his group from University of Iceland and Prof. Peter Lund and his group from Aalto University, Finland for their useful discussions.

Thanks Lars Hellberg for your helps on technical things in the lab. Thanks Prof. Igor Zoric for clarifying doubts in plasmonics and other topics in a simplified way and Dr. Michael Zach (former assistant supervisor) for your time on useful discussions and suggestions. I would like to thank the clean room technicians for their helps in samples preparation and characterization. Special credit is given to Henrik Frederiksen.

I would like to thank all the Chemical Physics group members for creating a nice and enjoyable working environment and your helps in several occasions. Special credits are given to Viktoria Gusak and Hans Fredriksson (former colleague) for your great helps in the UHV lab and my office mates Kristina Wettegren, Markus Schwind & Rafael Martins

Acknowledgements

(former colleagues), Pooya Tabib, and Benimino Iandolo for making a nice environment and your helps in different occasions.

I would like to thank my friends (Mani, Madhu, Nethaji, Madavan, and others) for their continuous motivations and supports. I am really grateful to all of you.

I would like to thank my father, mother, brother, sister, brother-in-law, relatives, and my fiancée for their endless love, continuous moral supports, and helping me achieve this feat in my academic career. I would like to thank acquaintances, well-wishers for their (indirect) helps in my academic career and personal life and finally Mother Nature for everything.

References

- [1] R. van de Krol, Y.Q. Liang, J. Schoonman, Solar hydrogen production with nanostructured metal oxides, *J Mater Chem*, 18 (2008) 2311-2320.
- [2] N.S. Lewis, D.G. Nocera, Powering the planet: Chemical challenges in solar energy utilization, *P Natl Acad Sci USA*, 103 (2006) 15729-15735.
- [3] M. Gratzel, Photoelectrochemical cells, *Nature*, 414 (2001) 338-344.
- [4] Observer, Worldwide electricity production from renewable energy sources, in: Observer (Ed.), Paris, 2012.
- [5] J.S. Roel Van de Krol, Photo-electrochemical production of hydrogen, in: Sustainable Energy Technologies: *Options and Prospects*, Springer, 2008, pp. 121-142.
- [6] H.B. Gray, Powering the planet with solar fuel, *Nat Chem*, 1 (2009) 7-7.
- [7] J. Nowotny, C.C. Sorrell, L.R. Sheppard, T. Bak, Solar-hydrogen: Environmentally safe fuel for the future, *Int J Hydrogen Energ*, 30 (2005) 521-544.
- [8] A. Fujishima, X.T. Zhang, D.A. Tryk, TiO₂ photocatalysis and related surface phenomena, *Surf Sci Rep*, 63 (2008) 515-582.
- [9] <http://old.iupac.org/projects/posters01/parmon01.pdf>.
- [10] <http://dev.nsta.org/evwebs/1952/photocatalysis.htm>.
- [11] A. Kudo, Photocatalyst materials for water splitting, *Catal Surv Asia*, 7 (2003) 31-38.
- [12] A. Kudo, Y. Miseki, Heterogeneous photocatalyst materials for water splitting, *Chem Soc Rev*, 38 (2009) 253-278.
- [13] M. Gratzel, Dye-sensitized solar cells, *J Photoch Photobio C*, 4 (2003) 145-153.
- [14] M. Ni, M.K.H. Leung, D.Y.C. Leung, K. Sumathy, A review and recent developments in photocatalytic water-splitting using TiO₂ for hydrogen production, *Renew Sust Energ Rev*, 11 (2007) 401-425.

References

- [15] M.R. Hoffmann, S.T. Martin, W.Y. Choi, D.W. Bahnemann, Environmental Applications of Semiconductor Photocatalysis, *Chem Rev*, 95 (1995) 69-96.
- [16] J. Nowotny, T. Bak, M.K. Nowotny, L.R. Sheppard, Titanium dioxide for solar-hydrogen I. Functional properties, *Int J Hydrogen Energ*, 32 (2007) 2609-2629.
- [17] T. Bak, J. Nowotny, M. Rekas, C.C. Sorrell, Defect chemistry and semiconducting properties of titanium dioxide: I. Intrinsic electronic equilibrium, *J Phys Chem Solids*, 64 (2003) 1043-1056.
- [18] T. Bak, J. Nowotny, M. Rekas, C.C. Sorrell, Defect chemistry and semiconducting properties of titanium dioxide: II. Defect diagrams, *J Phys Chem Solids*, 64 (2003) 1057-1067.
- [19] T. Bak, J. Nowotny, M. Rekas, C.C. Sorrell, Defect chemistry and semiconducting properties of titanium dioxide: III. Mobility of electronic charge carriers, *J Phys Chem Solids*, 64 (2003) 1069-1087.
- [20] A. Fujishima, K. Hashimoto, T. Watanabe, *TiO₂ Photocatalysis Fundamentals and Applications*, BKC Inc, 1999.
- [21] A. Fujishima, K. Honda, Electrochemical Photolysis of Water at a Semiconductor Electrode, *Nature*, 238 (1972) 37.
- [22] B. Oregan, M. Gratzel, A Low-Cost, High-Efficiency Solar-Cell Based on Dye-Sensitized Colloidal TiO₂ Films, *Nature*, 353 (1991) 737-740.
- [23] K. Adachi, K. Ohta, T. Mizuno, Photocatalytic Reduction of Carbon-Dioxide to Hydrocarbon Using Copper-Loaded Titanium-Dioxide, *Sol Energy*, 53 (1994) 187-190.
- [24] R.K. Sharma, M.C. Bhatnagar, G.L. Sharma, Mechanism of highly sensitive and fast response Cr doped TiO₂ oxygen gas sensor, *Sensor Actuat B-Chem*, 45 (1997) 209-215.
- [25] M. Haruta, Size- and support-dependency in the catalysis of gold, *Catal Today*, 36 (1997) 153-166.
- [26] A.S.K. Hashmi, G.J. Hutchings, Gold catalysis, *Angew Chem Int Edit*, 45 (2006) 7896-7936.
- [27] G.R. Elena Serranoa, Javier Garcia-Martinez, Nanotechnology for sustainable energy Renewable and sustainable energy reviews, 13 (2009) 2373-2384.

- [28] D.M. Adams, L. Brus, C.E.D. Chidsey, S. Creager, C. Creutz, C.R. Kagan, P.V. Kamat, M. Lieberman, S. Lindsay, R.A. Marcus, R.M. Metzger, M.E. Michel-Beyerle, J.R. Miller, M.D. Newton, D.R. Rolison, O. Sankey, K.S. Schanze, J. Yardley, X.Y. Zhu, Charge transfer on the nanoscale: Current status, *J Phys Chem B*, 107 (2003) 6668-6697.
- [29] U. Kriebig, *Optical properties of metal clusters*, Springer-Verlag, 1995.
- [30] S. Linic, P. Christopher, D.B. Ingram, Plasmonic-metal nanostructures for efficient conversion of solar to chemical energy, *Nat Mater*, 10 (2011) 911-921.
- [31] S.C. Warren, E. Thimsen, Plasmonic solar water splitting, *Energ Environ Sci*, 5 (2012) 5133-5146.
- [32] S.E. Braslavsky, *Glossary of terms used in Photochemistry 3(rd) Edition (IUPAC Recommendations 2006)*, *Pure Appl Chem*, 79 (2007) 293-465.
- [33] P.D. Tran, L.H. Wong, J. Barber, J.S.C. Loo, Recent advances in hybrid photocatalysts for solar fuel production, *Energ Environ Sci*, 5 (2012) 5902-5918.
- [34] P. Wang, B.B. Huang, Y. Dai, M.H. Whangbo, Plasmonic photocatalysts: harvesting visible light with noble metal nanoparticles, *Phys Chem Chem Phys*, 14 (2012) 9813-9825.
- [35] B.V. Zeghbroeck, P-N Junctions, in: *Principles of Semiconductor Devices*, 2011.
- [36] G.D. Gilliland, Photoluminescence spectroscopy of crystalline semiconductors, *Mat Sci Eng R*, 18 (1997) 99-399.
- [37] A.L. Linsebigler, G.Q. Lu, J.T. Yates, Photocatalysis on TiO₂ Surfaces - Principles, Mechanisms, and Selected Results, *Chem Rev*, 95 (1995) 735-758.
- [38] M.A. Henderson, A surface science perspective on TiO₂ photocatalysis, *Surf Sci Rep*, 66 (2011) 185-297.
- [39] Dynamics of trapping and recombination,
<http://students.chem.tue.nl/ifp20/pages/Chapter%202/ch2par4.html>.
- [40] U. Diebold, The surface science of titanium dioxide, *Surface Science Reports*, 48 (2003) 53-229.

References

- [41] R. Schaub, E. Wahlstrom, A. Ronnau, E. Laegsgaard, I. Stensgaard, F. Besenbacher, Oxygen-mediated diffusion of oxygen vacancies on the TiO₂(110) surface, *Science*, 299 (2003) 377-379.
- [42] L.B. Xiong, J.L. Li, B. Yang, Y. Yu, Ti³⁺ in the Surface of Titanium Dioxide: Generation, Properties and Photocatalytic Application, *J Nanomater*, (2012).
- [43] E. Hendry, F. Wang, J. Shan, T.F. Heinz, M. Bonn, Electron transport in TiO₂ probed by THz time-domain spectroscopy, *Phys Rev B*, 69 (2004).
- [44] D.W. Jing, M.C. Liu, Q.Y. Chen, L.J. Guo, Efficient photocatalytic hydrogen production under visible light over a novel W-based ternary chalcogenide photocatalyst prepared by a hydrothermal process, *Int J Hydrogen Energ*, 35 (2010) 8521-8527.
- [45] Z. Zhang, J.T. Yates, Band Bending in Semiconductors: Chemical and Physical Consequences at Surfaces and Interfaces, *Chem Rev*, 112 (2012) 5520-5551.
- [46] M.A. Barteau, Site Requirements of Reactions on Oxide Surfaces, *J Vac Sci Technol A*, 11 (1993) 2162-2168.
- [47] M. Gratzel, *Heterogeneous Photochemical Electron Transfer*, CRC Press, Florida, 1989.
- [48] http://en.wikipedia.org/wiki/Titanium_dioxide.
- [49] A. Kubacka, M. Fernandez-Garcia, G. Colon, Advanced Nanoarchitectures for Solar Photocatalytic Applications, *Chem Rev*, 112 (2012) 1555-1614.
- [50] S.D. Mo, W.Y. Ching, Electronic and Optical-Properties of 3 Phases of Titanium-Dioxide - Rutile, Anatase, and Brookite, *Phys Rev B*, 51 (1995) 13023-13032.
- [51] <http://www.galleries.com/minerals/oxides/anatase/anatase.htm>.
- [52] H. Tang, K. Prasad, R. Sanjines, P.E. Schmid, F. Levy, Electrical and Optical-Properties of TiO₂ Anatase Thin-Films, *J Appl Phys*, 75 (1994) 2042-2047.
- [53] A. Primo, A. Corma, H. Garcia, Titania supported gold nanoparticles as photocatalyst, *Phys Chem Chem Phys*, 13 (2011) 886-910.
- [54] R.G. Breckenridge, W.R. Hosler, Electrical Properties of Titanium Dioxide Semiconductors, *Phys Rev*, 91 (1953) 793-802.

- [55] L. Forro, O. Chauvet, D. Emin, L. Zuppiroli, H. Berger, F. Levy, High-Mobility N-Type Charge-Carriers in Large Single-Crystals of Anatase (TiO₂), *J Appl Phys*, 75 (1994) 633-635.
- [56] Z.C. Wang, U. Helmersson, P.O. Kall, Optical properties of anatase TiO₂ thin films prepared by aqueous sol-gel process at low temperature, *Thin Solid Films*, 405 (2002) 50-54.
- [57] V. Melnyk, V. Shymanovska, G. Puchkovska, T. Bezrodna, G. Klishevich, Low-temperature luminescence of different TiO₂ modifications, *J Mol Struct*, 744 (2005) 573-576.
- [58] H. Najafov, S. Tokita, S. Ohshio, A. Kato, H. Saitoh, Green and ultraviolet emissions from anatase TiO₂ films fabricated by chemical vapor deposition, *Japanese Journal of Applied Physics Part 1-Regular Papers Short Notes & Review Papers*, 44 (2005) 245-253.
- [59] H. Tang, H. Berger, P.E. Schmid, F. Levy, G. Burri, Photoluminescence in TiO₂ Anatase Single-Crystals, *Solid State Commun*, 87 (1993) 847-850.
- [60] R.T. Williams, K.S. Song, The Self-Trapped Exciton, *J Phys Chem Solids*, 51 (1990) 679-716.
- [61] P.V. Kamat, TiO₂ Nanostructures: Recent Physical Chemistry Advances, *J Phys Chem C*, 116 (2012) 11849-11851.
- [62] X. Chen, S.S. Mao, Titanium dioxide nanomaterials: Synthesis, properties, modifications, and applications, *Chem Rev*, 107 (2007) 2891-2959.
- [63] Y. Zhao, C.Z. Li, X.H. Liu, F. Gu, H.B. Jiang, W. Shao, L. Zhang, Y. He, Synthesis and optical properties of TiO₂ nanoparticles, *Mater Lett*, 61 (2007) 79-83.
- [64] F. Cao, G. Oskam, P.C. Searson, J.M. Stipkala, T.A. Heimer, F. Farzad, G.J. Meyer, Electrical and Optical-Properties of Porous Nanocrystalline TiO₂ Films, *J Phys Chem-U.S.*, 99 (1995) 11974-11980.
- [65] T. Ohno, K. Sarukawa, K. Tokieda, M. Matsumura, Morphology of a TiO₂ photocatalyst (Degussa, P-25) consisting of anatase and rutile crystalline phases, *J Catal*, 203 (2001) 82-86.
- [66] D.C. Hurum, A.G. Agrios, K.A. Gray, T. Rajh, M.C. Thurnauer, Explaining the enhanced photocatalytic activity of Degussa P25 mixed-phase TiO₂ using EPR, *J Phys Chem B*, 107 (2003) 4545-4549.

References

- [67] A. Kay, M. Gratzel, Artificial Photosynthesis .1. Photosensitization of TiO₂ Solar-Cells with Chlorophyll Derivatives and Related Natural Porphyrins, *J Phys Chem*, 97 (1993) 6272-6277.
- [68] J. Jitputti, Y. Suzuki, S. Yoshikawa, Synthesis of TiO₂ nanowires and their photocatalytic activity for hydrogen evolution, *Catal Commun*, 9 (2008) 1265-1271.
- [69] K. Zhu, N.R. Neale, A. Miedaner, A.J. Frank, Enhanced charge-collection efficiencies and light scattering in dye-sensitized solar cells using oriented TiO₂ nanotubes arrays, *Nano Lett*, 7 (2007) 69-74.
- [70] R.L.a.A. Westwood, Carbonaceous nanomaterials for the enhancement of TiO₂ photocatalysis, *Carbon*, 49 (2010) 741-772.
- [71] Z.G. Zou, J.H. Ye, K. Sayama, H. Arakawa, Direct splitting of water under visible light irradiation with an oxide semiconductor photocatalyst, *Nature*, 414 (2001) 625-627.
- [72] J.H. Park, S. Kim, A.J. Bard, Novel carbon-doped TiO₂ nanotube arrays with high aspect ratios for efficient solar water splitting, *Nano Lett*, 6 (2006) 24-28.
- [73] S.U.M. Khan, M. Al-Shahry, W.B. Ingler, Efficient photochemical water splitting by a chemically modified n-TiO₂ *Science*, 297 (2002) 2243-2245.
- [74] J.M.W. Y. J. Chen, C. S. Lin, G. Y. Jhan, and M. S. Wong, Role of carbon in titania as visible-light photocatalyst prepared by flat-flame chemical vapor condensation method, *J Vac Sci Technol A*, 27 (2009) 862-866.
- [75] C.S. Enache, J. Schoonman, R.V. de Krol, Addition of carbon to anatase TiO₂ by n-hexane treatment - surface or bulk doping?, *Appl Surf Sci*, 252 (2006) 6342-6347.
- [76] H. Irie, Y. Watanabe, K. Hashimoto, Nitrogen-concentration dependence on photocatalytic activity of TiO₂-xN_x powders, *J Phys Chem B*, 107 (2003) 5483-5486.
- [77] R. Asahi, T. Morikawa, T. Ohwaki, K. Aoki, Y. Taga, Visible-light photocatalysis in nitrogen-doped titanium oxides, *Science*, 293 (2001) 269-271.
- [78] J.L. Gole, J.D. Stout, C. Burda, Y.B. Lou, X.B. Chen, Highly efficient formation of visible light tunable TiO₂-xN_x photocatalysts and their transformation at the nanoscale, *J Phys Chem B*, 108 (2004) 1230-1240.
- [79] W. Zhao, W.H. Ma, C.C. Chen, J.C. Zhao, Z.G. Shuai, Efficient degradation of toxic organic pollutants with Ni₂O₃/TiO₂-xB_x under visible irradiation, *Journal of the american chemical society*, 126 (2004) 4782-4783.

- [80] T. Umebayashi, T. Yamaki, H. Itoh, K. Asai, Band gap narrowing of titanium dioxide by sulfur doping, *Appl Phys Lett*, 81 (2002) 454-456.
- [81] H.A. Atwater, A. Polman, Plasmonics for improved photovoltaic devices, *Nat Mater*, 9 (2010) 205-213.
- [82] Y.X. Chen, Z.B. Wei, Y.X. Chen, H.X. Lin, Z.P. Hong, H.Q. Liu, Y.L. Dong, C.Y. Yu, W.Z. Li, Metal-Semiconductor Catalyst - Photocatalytic and Electrochemical-Behavior of Pt-TiO₂ for the Water Gas Shift Reaction, *J Mol Catal*, 21 (1983) 275-289.
- [83] P.V. Kamat, Manipulation of Charge Transfer Across Semiconductor Interface. A Criterion That Cannot Be Ignored in Photocatalyst Design, *J Phys Chem Lett*, 3 (2012) 663-672.
- [84] H.T. Yu, X. Quan, S. Chen, H.M. Zhao, TiO₂-multiwalled carbon nanotube heterojunction Arrays and their charge separation capability, *J Phys Chem C*, 111 (2007) 12987-12991.
- [85] J. Sun, M.T. Cole, N. Lindvall, K.B.K. Teo, A. Yurgens, Noncatalytic chemical vapor deposition of graphene on high-temperature substrates for transparent electrodes, *Appl Phys Lett*, 100 (2012).
- [86] J. Sun, N. Lindvall, M.T. Cole, K.T.T. Angel, T. Wang, K.B.K. Teo, D.H.C. Chua, J.H. Liu, A. Yurgens, Low Partial Pressure Chemical Vapor Deposition of Graphene on Copper, *Ieee T Nanotechnol*, 11 (2012) 255-260.
- [87] J. Sun, N. Lindvall, M.T. Cole, K.B.K. Teo, A. Yurgens, Large-area uniform graphene-like thin films grown by chemical vapor deposition directly on silicon nitride, *Appl Phys Lett*, 98 (2011).
- [88] H. Fredriksson, Y. Alaverdyan, A. Dmitriev, C. Langhammer, D.S. Sutherland, M. Zaech, B. Kasemo, Hole-mask colloidal lithography, *Adv Mater*, 19 (2007) 4297.
- [89] R.H.a.L. Benatar, *A Practical Guide To Scanning Probe Microscopy* (2000).
- [90] <http://www.nanoscience.com/education/afm.html>.
- [91] <http://www.hunterlab.com>, Double Vs Single beam spectrophotometer (2008).
- [92] <http://www.answers.com/topic/chemical-reactor-2>.
- [93] [http://www.dusemund.com/mikroglas/Microreaction Technolog1.pdf](http://www.dusemund.com/mikroglas/Microreaction%20Technolog1.pdf).

References

- [94] T.R. Henriksen, J.L. Olsen, P. Vesborg, I. Chorkendorff, O. Hansen, Highly sensitive silicon microreactor for catalyst testing, *Rev Sci Instrum*, 80 (2009) -.
- [95] <http://science.widener.edu/svb/massspec/massspec.pdf>.
- [96] <http://www.chm.bris.ac.uk/ms/theory/quad-massspec.html>.
- [97] P.C.K. Vesborg, J.L. Olsen, T.R. Henriksen, I. Chorkendorff, O. Hansen, Gas-phase photocatalysis in microreactors, *Chem Eng J*, 160 (2010) 738-741.
- [98] J.L.F.a.W. Wang, Carbon Materials for in Photocatalysis, in: J.L.F. Philippe Serp (Ed.) *Carbon Materials for Catalysis*, 2008.
- [99] Y.H. Ng, S. Ikeda, M. Matsumura, R. Amal, A perspective on fabricating carbon-based nanomaterials by photocatalysis and their applications, *Energ Environ Sci*, 5 (2012) 9307-9318.
- [100] P.R. Wallace, The Band Theory of Graphite, *Phys Rev*, 71 (1947) 622-634.
- [101] <http://en.wikipedia.org/wiki/Semimetal>.
- [102] A.C. Ferrari, Raman spectroscopy of graphene and graphite: Disorder, electron-phonon coupling, doping and nonadiabatic effects, *Solid State Commun*, 143 (2007) 47-57.
- [103] A.C. Ferrari, J. Robertson, Interpretation of Raman spectra of disordered and amorphous carbon, *Phys Rev B*, 61 (2000) 14095-14107.
- [104] F. Bonaccorso, Z. Sun, T. Hasan, A.C. Ferrari, Graphene photonics and optoelectronics, *Nat Photonics*, 4 (2010) 611-622.
- [105] Q.J. Xiang, J.G. Yu, M. Jaroniec, Graphene-based semiconductor photocatalysts, *Chem Soc Rev*, 41 (2012) 782-796.
- [106] B.F. Machado, P. Serp, Graphene-based materials for catalysis, *Catal Sci Technol*, 2 (2012) 54-75.
- [107] M. Pumera, Graphene-based nanomaterials for energy storage, *Energ Environ Sci*, 4 (2011) 668-674.
- [108] S. Bae, H. Kim, Y. Lee, X.F. Xu, J.S. Park, Y. Zheng, J. Balakrishnan, T. Lei, H.R. Kim, Y.I. Song, Y.J. Kim, K.S. Kim, B. Ozyilmaz, J.H. Ahn, B.H. Hong, S. Iijima, Roll-

to-roll production of 30-inch graphene films for transparent electrodes, *Nat Nanotechnol*, 5 (2010) 574-578.

[109] A.K. Geim, K.S. Novoselov, The rise of graphene, *Nat Mater*, 6 (2007) 183-191.

[110] A.K. Geim, Graphene: Status and Prospects, *Science*, 324 (2009) 1530-1534.

[111] G. Eda, G. Fanchini, M. Chhowalla, Large-area ultrathin films of reduced graphene oxide as a transparent and flexible electronic material, *Nat Nanotechnol*, 3 (2008) 270-274.

[112] W.S. Hummers, R.E. Offeman, Preparation of Graphitic Oxide, *J Am Chem Soc*, 80 (1958) 1339-1339.

[113] S.F. Pei, H.M. Cheng, The reduction of graphene oxide, *Carbon*, 50 (2012) 3210-3228.

[114] G. Williams, B. Seger, P.V. Kamat, TiO₂-graphene nanocomposites. UV-assisted photocatalytic reduction of graphene oxide, *Acs Nano*, 2 (2008) 1487-1491.

[115] Y.W. Zhu, S. Murali, W.W. Cai, X.S. Li, J.W. Suk, J.R. Potts, R.S. Ruoff, Graphene and Graphene Oxide: Synthesis, Properties, and Applications (vol 22, pg 3906, 2010), *Adv Mater*, 22 (2010) 5226-5226.

[116] W.Q. Fan, Q.H. Lai, Q.H. Zhang, Y. Wang, Nanocomposites of TiO₂ and Reduced Graphene Oxide as Efficient Photocatalysts for Hydrogen Evolution, *J Phys Chem C*, 115 (2011) 10694-10701.

[117] H. Zhang, X.J. Lv, Y.M. Li, Y. Wang, J.H. Li, P25-Graphene Composite as a High Performance Photocatalyst, *Acs Nano*, 4 (2010) 380-386.

[118] K.F. Zhou, Y.H. Zhu, X.L. Yang, X. Jiang, C.Z. Li, Preparation of graphene-TiO₂ composites with enhanced photocatalytic activity, *New J Chem*, 35 (2011) 353-359.

[119] F. Rodriguez-Reinoso, The role of carbon materials in heterogeneous catalysis, *Carbon*, 36 (1998) 159-175.

[120] P. Serp, M. Corrias, P. Kalck, Carbon nanotubes and nanofibers in catalysis, *Appl Catal a-Gen*, 253 (2003) 337-358.

[121] L.F. Velasco, J.B. Parra, C.O. Ania, Role of activated carbon features on the photocatalytic degradation of phenol, *Appl Surf Sci*, 256 (2010) 5254-5258.

References

- [122] B. Tryba, A.W. Morawski, M. Inagaki, Application of TiO₂-mounted activated carbon to the removal of phenol from water, *Appl Catal B-Environ*, 41 (2003) 427-433.
- [123] R. Leary, A. Westwood, Carbonaceous nanomaterials for the enhancement of TiO₂ photocatalysis, *Carbon*, 49 (2011) 741-772.
- [124] N. Serpone, Is the band gap of pristine TiO₂ narrowed by anion- and cation-doping of titanium dioxide in second-generation photocatalysts?, *J Phys Chem B*, 110 (2006) 24287-24293.
- [125] B. Neumann, P. Bogdanoff, H. Tributsch, S. Sakthivel, H. Kisch, Electrochemical mass spectroscopic and surface photovoltage studies of catalytic water photooxidation by undoped and carbon-doped titania, *J Phys Chem B*, 109 (2005) 16579-16586.
- [126] C.S. Enache, J. Schoonman, R. van de Krol, The photoresponse of iron- and carbon-doped TiO₂ (anatase) photoelectrodes, *J Electroceram*, 13 (2004) 177-182.
- [127] Y.T. Liang, B.K. Vijayan, K.A. Gray, M.C. Hersam, Minimizing Graphene Defects Enhances Titania Nanocomposite-Based Photocatalytic Reduction of CO₂ for Improved Solar Fuel Production, *Nano Lett*, 11 (2011) 2865-2870.
- [128] K. Woan, G. Pyrgiotakis, W. Sigmund, Photocatalytic Carbon-Nanotube-TiO₂ Composites, *Adv Mater*, 21 (2009) 2233-2239.
- [129] W.C. Oh, A.R. Jung, W.B. Ko, Preparation of fullerene/TiO₂ composite and its photocatalytic effect, *J Ind Eng Chem*, 13 (2007) 1208-1214.
- [130] P.V. Kamat, I. Bedja, S. Hotchandani, Photoinduced Charge-Transfer between Carbon and Semiconductor Clusters - One-Electron Reduction of C-60 in Colloidal TiO₂ Semiconductor Suspensions, *J Phys Chem-U.S.*, 98 (1994) 9137-9142.
- [131] L.W. Zhang, H.B. Fu, Y.F. Zhu, Efficient TiO₂ photocatalysts from surface hybridization of TiO₂ particles with graphite-like carbon, *Adv Funct Mater*, 18 (2008) 2180-2189.
- [132] S. Krishnamurthy, I.V. Lightcap, P.V. Kamat, Electron transfer between methyl viologen radicals and graphene oxide: Reduction, electron storage and discharge, *J Photoch Photobio A*, 221 (2011) 214-219.
- [133] A. Kongkanand, P.V. Kamat, Electron storage in single wall carbon nanotubes. Fermi level equilibration in semiconductor-SWCNT suspensions, *Acs Nano*, 1 (2007) 13-21.

- [134] Y.H. Zhang, Z.R. Tang, X.Z. Fu, Y.J. Xu, TiO₂-Graphene Nanocomposites for Gas-Phase Photocatalytic Degradation of Volatile Aromatic Pollutant: Is TiO₂-Graphene Truly Different from Other TiO₂-Carbon Composite Materials?, *Acs Nano*, 4 (2010) 7303-7314.
- [135] P.W. Fowler, A. Ceulemans, Electron Deficiency of the Fullerenes, *J Phys Chem-Us*, 99 (1995) 508-510.
- [136] N.J. Bell, H.N. Yun, A.J. Du, H. Coster, S.C. Smith, R. Amal, Understanding the Enhancement in Photoelectrochemical Properties of Photocatalytically Prepared TiO₂-Reduced Graphene Oxide Composite, *J Phys Chem C*, 115 (2011) 6004-6009.
- [137] S. Link, M.A. El-Sayed, Shape and size dependence of radiative, non-radiative and photothermal properties of gold nanocrystals, *Int Rev Phys Chem*, 19 (2000) 409-453.
- [138] S.A. Maier, *Plasmonics: Fundamentals and Applications*, Springer, 2007.
- [139] M. Meier, A. Wokaun, Enhanced Fields on Large Metal Particles - Dynamic Depolarization, *Opt Lett*, 8 (1983) 581-583.
- [140] R.D. Averitt, D. Sarkar, N.J. Halas, Plasmon resonance shifts of Au-coated Au₂S nanoshells: Insight into multicomponent nanoparticle growth, *Phys Rev Lett*, 78 (1997) 4217-4220.
- [141] U. Kreibig, Electronic Properties of Small Silver Particles - Optical-Constants and Their Temperature-Dependence, *J Phys F Met Phys*, 4 (1974) 999-1014.
- [142] T. Klar, M. Perner, S. Grosse, G. von Plessen, W. Spirkl, J. Feldmann, Surface-plasmon resonances in single metallic nanoparticles, *Phys Rev Lett*, 80 (1998) 4249-4252.
- [143] P.G. Kik, A.L. Martin, S.A. Maier, H.A. Atwater, Metal nanoparticle arrays for near field optical lithography, *P Soc Photo-Opt Ins*, 4810 (2002) 7-13.
- [144] J.J. Chen, J.C.S. Wu, P.C. Wu, D.P. Tsai, Plasmonic Photocatalyst for H₂ Evolution in Photocatalytic Water Splitting, *J Phys Chem C*, 115 (2011) 210-216.
- [145] M.K. Kumar, S. Krishnamoorthy, L.K. Tan, S.Y. Chiam, S. Tripathy, H. Gao, Field Effects in Plasmonic Photocatalyst by Precise SiO₂ Thickness Control Using Atomic Layer Deposition, *Acs Catal*, 1 (2011) 300-308.

References

- [146] Z.W. Liu, W.B. Hou, P. Pavaskar, M. Aykol, S.B. Cronin, Plasmon Resonant Enhancement of Photocatalytic Water Splitting Under Visible Illumination, *Nano Lett*, 11 (2011) 1111-1116.
- [147] H. Wang, T.T. You, W.W. Shi, J.H. Li, L. Guo, Au/TiO₂/Au as a Plasmonic Coupling Photocatalyst, *J Phys Chem C*, 116 (2012) 6490-6494.
- [148] P. Christopher, D.B. Ingram, S. Linic, Enhancing Photochemical Activity of Semiconductor Nanoparticles with Optically Active Ag Nanostructures: Photochemistry Mediated by Ag Surface Plasmons, *J Phys Chem C*, 114 (2010) 9173-9177.
- [149] R.A. Molina, D. Weinmann, R.A. Jalabert, Oscillatory size dependence of the surface plasmon linewidth in metallic nanoparticles, *Phys Rev B*, 65 (2002).
- [150] A. Furube, L. Du, K. Hara, R. Katoh, M. Tachiya, Ultrafast plasmon-induced electron transfer from gold nanodots into TiO₂ nanoparticles, *J Am Chem Soc*, 129 (2007) 14852-+.
- [151] S.T. Kochuveedu, D.P. Kim, D.H. Kim, Surface-Plasmon-Induced Visible Light Photocatalytic Activity of TiO₂ Nanospheres Decorated by Au Nanoparticles with Controlled Configuration, *J Phys Chem C*, 116 (2012) 2500-2506.
- [152] S. Mubeen, J. Lee, N. Singh, S. Kramer, G.D. Stucky, M. Moskovits, An autonomous photosynthetic device in which all charge carriers derive from surface plasmons, *Nat Nanotechnol*, 8 (2013) 247-251.
- [153] Y. Tian, T. Tatsuma, Mechanisms and applications of plasmon-induced charge separation at TiO₂ films loaded with gold nanoparticles, *J Am Chem Soc*, 127 (2005) 7632-7637.
- [154] C.G. Silva, R. Juarez, T. Marino, R. Molinari, H. Garcia, Influence of Excitation Wavelength (UV or Visible Light) on the Photocatalytic Activity of Titania Containing Gold Nanoparticles for the Generation of Hydrogen or Oxygen from Water, *J Am Chem Soc*, 133 (2011) 595-602.
- [155] C. Hendrich, J. Bosbach, F. Stietz, F. Hubenthal, T. Vartanyan, F. Trager, Chemical interface damping of surface plasmon excitation in metal nanoparticles: a study by persistent spectral hole burning, *Appl Phys B-Lasers O*, 76 (2003) 869-875.
- [156] X. Chen, Y.T. Chen, M. Yan, M. Qiu, Nanosecond Photothermal Effects in Plasmonic Nanostructures, *Acs Nano*, 6 (2012) 2550-2557.

- [157] J.R. Adleman, D.A. Boyd, D.G. Goodwin, D. Psaltis, Heterogenous Catalysis Mediated by Plasmon Heating, *Nano Lett*, 9 (2009) 4417-4423.
- [158] G. Baffou, R. Quidant, C. Girard, Heat generation in plasmonic nanostructures: Influence of morphology, *Appl Phys Lett*, 94 (2009).
- [159] W.H. Hung, M. Aykol, D. Valley, W.B. Hou, S.B. Cronin, Plasmon Resonant Enhancement of Carbon Monoxide Catalysis, *Nano Lett*, 10 (2010) 1314-1318.
- [160] T. Inoue, A. Fujishima, S. Konishi, K. Honda, Photoelectrocatalytic Reduction of Carbon-Dioxide in Aqueous Suspensions of Semiconductor Powders, *Nature*, 277 (1979) 637-638.
- [161] Y. Hori, H. Wakebe, T. Tsukamoto, O. Koga, Electrocatalytic Process of Co Selectivity in Electrochemical Reduction of Co₂ at Metal-Electrodes in Aqueous-Media, *Electrochim Acta*, 39 (1994) 1833-1839.
- [162] R.L. Cook, R.C. Macduff, A.F. Sammells, Photoelectrochemical Carbon-Dioxide Reduction to Hydrocarbons at Ambient-Temperature and Pressure, *J Electrochem Soc*, 135 (1988) 3069-3070.
- [163] Y. Hori, K. Kikuchi, S. Suzuki, Production of Co and Ch₄ in Electrochemical Reduction of Co₂ at Metal-Electrodes in Aqueous Hydrogencarbonate Solution, *Chem Lett*, (1985) 1695-1698.
- [164] A.A. Peterson, F. Abild-Pedersen, F. Studt, J. Rossmeisl, J.K. Norskov, How copper catalyzes the electroreduction of carbon dioxide into hydrocarbon fuels, *Energ Environ Sci*, 3 (2010) 1311-1315.
- [165] Y. Li, W.N. Wang, Z.L. Zhan, M.H. Woo, C.Y. Wu, P. Biswas, Photocatalytic reduction of CO₂ with H₂O on mesoporous silica supported Cu/TiO₂ catalysts, *Appl Catal B-Environ*, 100 (2010) 386-392.
- [166] I.H. Tseng, J.C.S. Wu, H.Y. Chou, Effects of sol-gel procedures on the photocatalysis of Cu/TiO₂ in CO₂ photoreduction, *J Catal*, 221 (2004) 432-440.
- [167] J.C.S. Wu, H.M. Lin, C.L. Lai, Photo reduction of CO₂ to methanol using optical-fiber photoreactor, *Appl Catal a-Gen*, 296 (2005) 194-200.
- [168] H.W.N. Slamet, Ezza Purnama, Kapti Riyani and Jarnuzi Gunlazuardi, Effect of Copper Species in a Photocatalytic Synthesis of Methanol from Carbon Dioxide over Copper-doped Titania Catalysts, *World Applied Sciences Journal*, 6 (2009) 112-122.

References

- [169] H. Fredriksson, D. Chakarov, B. Kasemo, Patterning of highly oriented pyrolytic graphite and glassy carbon surfaces by nanolithography and oxygen plasma etching, *Carbon*, 47 (2009) 1335-1342.
- [170] H. Fredriksson, T. Pakizeh, M. Kall, B. Kasemo, D. Chakarov, Resonant optical absorption in graphite nanostructures, *J Opt a-Pure Appl Op*, 11 (2009).
- [171] O.I. Micic, Y.N. Zhang, K.R. Cromack, A.D. Trifunac, M.C. Thurnauer, Photoinduced Hole Transfer from TiO_2 to Methanol Molecules in Aqueous-Solution Studied by Electron-Paramagnetic-Resonance, *J Phys Chem-Us*, 97 (1993) 13284-13288.
- [172] C.C. Chuang, C.C. Chen, J.L. Lin, Photochemistry of methanol and methoxy groups adsorbed on powdered TiO_2 , *J Phys Chem B*, 103 (1999) 2439-2444.
- [173] D.A. Panayotov, S.P. Burrows, J.R. Morris, Photooxidation Mechanism of Methanol on Rutile TiO_2 Nanoparticles, *J Phys Chem C*, 116 (2012) 6623-6635.
- [174] C.Y. Wang, H. Groenzin, M.J. Shultz, Direct observation of competitive adsorption between methanol and water on TiO_2 : An in situ sum-frequency generation study, *J Am Chem Soc*, 126 (2004) 8094-8095.
- [175] G.L. Chiarello, M.H. Aguirre, E. Selli, Hydrogen production by photocatalytic steam reforming of methanol on noble metal-modified TiO_2 , *J Catal*, 273 (2010) 182-190.
- [176] J. Greaves, L. Al-Mazroai, A. Nuhu, P. Davies, M. Bowker, Photocatalytic methanol reforming on Au/TiO_2 for hydrogen production, *Gold Bull*, 39 (2006) 216-219.
- [177] W.C. Lin, W.D. Yang, I.L. Huang, T.S. Wu, Z.J. Chung, Hydrogen Production from Methanol/Water Photocatalytic Decomposition Using $\text{Pt/TiO}_{(2-x)\text{N}(x)}$ Catalyst, *Energ Fuel*, 23 (2009) 2192-2196.
- [178] O. Rosseler, M.V. Shankar, M.K.L. Du, L. Schmidlin, N. Keller, V. Keller, Solar light photocatalytic hydrogen production from water over Pt and Au/TiO_2 (anatase/rutile) photocatalysts: Influence of noble metal and porogen promotion, *J Catal*, 269 (2010) 179-190.